WALL CONFINEMENT EFFECTS FOR SPHERES IN THE REYNOLDS NUMBER RANGE OF 30-2000

by

TOSHINOSUKE AKUTSU

B.A. Sc., Kanto Gakuin University, 1970

M.A. Sc., Kanto Gakuin University, 1972

A THESIS SUBMITTED IN PARTIAL FULFILMENT OF

THE REQUIREMENTS FOR THE DEGREE OF

MASTER OF APPLIED SCIENCE

in

THE FACULTY OF GRADUATE STUDIES

Department of Mechanical Engineering

We accept this thesis as conforming to the required standard

THE UNIVERSITY OF BRITISH COLUMBIA

June, 1977

In presenting this thesis in partial fulfilment of the requirements for an advanced degree at the University of British Columbia, I agree that the Library shall make it freely available for reference and study. I further agree that permission for extensive copying of this thesis for scholarly purposes may be granted by the Head of my Department or by his representatives. It is understood that publication, in part or in whole, or the copying of this thesis for financial gain shall not be allowed without my written permission.

TOSHINOSUKE AKUTSU

Department of Mechanical Engineering

The University of British Columbia
Vancouver, British Columbia
Canada, V6T 1W5

Date Aug. 12, 1977

ABSTRACT

This thesis studies in detail: formation, development and instability of the vortex ring; associated surface pressure distribution; and drag for a family of spheres in the Reynolds number range of 30 - 2000 and the blockage ratio of 3 - 30%. In the beginning, a glycerol-water solution tunnel used in the experimental program is briefly described followed by an explanation of the model support system, pressure measuring instrumentation, drag balance and test procedures. An approach to the data reduction, so critical at low Reynolds number, is discussed and a new definition of the pressure coefficient which promises to be less dependent on test facilities and pressure gradients is evolved. Finally, the test data are analyzed as functions of the confinement condition and Reynolds number.

The results suggest that the ratio of the model to vertical stem support should be at least 10 to make stem effects negligible. Influence of Reynolds number on the surface pressure distribution is primarily confined to the range $R_n < 1000$. However, for the model with the highest blockage ratio of 30.6%, the pressure continues to show Reynolds number dependency for R_n as high as 2300 (limit of the tunnel capability for a glycerol-water

concentration used). In general, the effect of Reynolds number is to increase the minimum as well as the wake pressure. On the other hand, the effect of an increase in the blockage ratio is just the opposite. The wall confinement tends to increase the drag coefficient, however, the classical dependence of skin friction on the Reynolds number, $C_{d,f} \alpha R_n^{1/2}$, is maintained. The results vividly showed inadequacy of Maskell's correction procedure particularly at higher blockage (S/C > 5%).

An extensive flow visualization study using dye injection in conjunction with high speed photography complements the test program.

TABLE OF CONTENTS

Chapter Page

LIST OF FIGURES

Figure | Page

Figure | Page

Figure | Page

LIST OF APPENDIX FIGURES

ACKNOWLEDGEMENT

I would like to take this opportunity to express my gratitude and sincere thanks to Professor V.J. Modi for the enthusiastic guidance given throughout the research program and helpful suggestions during the preparation of the thesis. His help and encouragement have been invaluable.

The cheerful assistance of the technical staff is gratefully acknowledged. Their skillful assistance greatly accelerated the research program.

The investigation was supported by the National Research Council of Canada, Grant No. A-2181.

Finally, special appreciation is extended to my parents, Mr. and Mrs. Toshi Akutsu, for their encouragement, love and understanding during difficult times.

LIST OF SYMBOLS

B	cross-sectional area of the wake in Maskell's theory
c	velocity of sound
C	tunnel cross-sectional area
C_d	$F_t / (1/2)\rho U^2 S$
$\bar{C}_{d,p}$	pressure drag coefficient based on average velocity
$\underline{C}_{d,p}$	pressure drag coefficient based on centerline velocity
$\overline{C_{d,t}}$	total drag coefficient, $\overline{C_{d,p}} + \overline{C_{d,f}}$ based on average velocity
$\underline{C}_{d,t}$	total drag coefficient, $\underline{C}_{d,p} + \underline{C}_{d,t}$ based on centerline velocity
$\overline{C_{d,f}}$	skin friction component of total drag, based on average velocity
$\underline{C}_{d,f}$	skin friction component of total drag, based on centerline velocity
C_n	percentage concentration of glycerol-water solution by weight
C_p	$(P_\theta - P_r)/(P_0 - P_r)$
$\overline{C_p}$	$(P_\theta - P_\infty)/(1/2)\rho U^2$
$\underline{C_p}$	$(P_\theta - P_\infty)/(1/2)\rho U_c^2$
$\hat{C}_p$	$(P_\theta - P_r)/(1/2)\rho U^2$
C_{p_b}	base pressure coefficient, $(P_b - P_r)/(P_0 - P_r)$
C_{p_m}	minimum pressure coefficient, $(P_m - P_r)/(P_0 - P_r)$
$\bar{C}_{p_b}$	base pressure coefficient, $(P_b - P_\infty)/(1/2)\rho U^2$

D	sphere diameter
d_i	inside diameter of stem
d_o	outside diameter of stem
f	frequency of shedding vortex sheet
F	sectional pressure drag
F_t	total sectional drag
k	size of roughness element
M_n	Mach number, U/c
P	static pressure
P_θ	static pressure on the surface of the sphere at an angle θ from the front stagnation point
P_∞	static pressure of undisturbed stream
P_b	base pressure
P_r	static pressure at reference tap, in the present case $r = 60°$
q	dynamic pressure, $(1/2)\rho U^2$
R_c, R_o	cold and operating resistance of the hot film probe, respectively
R_n	Reynolds number, UD/ν
$R_{n,cr}$	critical Reynolds number
S	diametral cross-sectional area
S_n	fD/U
T	temperature of solution
U	average velocity in the test-section based on a flow rate as given by the orifice meter
U_c	centerline velocity
u'	rms value of velocity fluctuations in the downstream direction

U_z	local velocity as measured by a hot film probe
V	d.c. voltage output of a constant temperature anemometer
y_p	probe distance from the tunnel inlet
y_m	location of model from the tunnel inlet
z	vertical coordinate with origin at the bottom of the test section
δ	zero drift of the electronic pressure measuring system
θ	angular location of a pressure tap with reference to the front stagnation point
θ_s	angular location of the separating shear layer with respect to the rear stagnation point
ε	roughness parameter, k/D
μ	dynamic viscosity
ν	kinematic viscosity, μ/ρ
ρ	density
σ	component of turbulent intensity in the downstream direction, u'/U
τ_w	skin friction, shear stress at the wall
ϕ	differential pressure at orifice meter

1. INTRODUCTION

1.1 Preliminary Remarks

Geometrical symmetry has held special fascination for the human mind since millennia. Pyramids, the colossal monuments of pharaohs, depict symmetry at its best through straight lines. However, curvilinear symmetry in the form of 'sun-disc' has always been given special position in the ancient pantheon. Sphere is merely a symmetrical extension of circle in space.

There are numerous situations of practical importance where bodies of revolution in general and spherical objects in particular operate in fluid fields with relatively low Reynolds number. Towed sonars or stationary hydrophones used in submarine detection systems, oceanographic platforms employed in hydrographic surveys, proposed configurations of underwater habitats, oil-storage tanks,meteorological studies of rain drops and balloons, spray drying in the chemical industry, etc. belong to this class of problems. For laboratory simulation, model of a given system is usually tested in wind or water tunnels where confined condition is created either unintentionally or through choice for geometric similarity.

In the present case, however, attention on the spherical geometry was focussed due to the interest in understanding and improving hydrodynamic performance of the prosthetic aortic heart valve. The Starr-Edwards prosthesis, when implanted in an aorta, has been observed to work under a highly confined condition with the blockage ratio in the range of 15-50% depending on the size of the aorta and model of the prosthesis used. The aortic flow, even in absence of blockage, is extremely complicated, being non-Newtonian and pulsatile with complex swirling component of velocity superposed. The aortic wall confinement would further complicate the problem. Unfortunately, surprising as it may seem, blockage effects for even a uniform flow past a sphere at low Reynolds number remains virtually unexplored to date. This thesis represents a modest step towards better understanding of this difficult problem.

1.2 Survey of Literature

Interest in the behaviour of a sphere moving through a fluid goes back to the days of Newton who is credited with the first recorded measurements on sphere drag. Following this but prior to 1930, numerous experiments on the drag of falling spheres were conducted and a body of information generated for Reynolds numbers in the range $10^{-1} - 10^{6}$. These

data, in general, show a significant degree of scatter and hence are approximated by the familiar "standard" drag curve. It apparently applies only to smooth spheres in steady motion in a non-turbulent, isothermal, incompressible continuum fluid of effectively infinite extent. Ever since, theoretical and practical interest in the subject has resulted in a large volume of literature, and the contributions up to 1960 have been cited by Torobin and Gauvin[1] in their comprehensive review of the field.

The drag coefficient appears to depend primarily on the magnitude of the relative turbulence intensity and Reynolds number. Increasing turbulence intensities cause a systematic regression of the transition region of the drag coefficient curve towards lower Reynolds number together with a moderate increase of the drag coefficient in both subcritical and supercritical regions. In 1963, Heinrich et al.[2] carried out sphere drag measurements in a wind tunnel for $2 \times 10^3 < R_n < 2 \times 10^4$ and $0.078 < M_n < 0.39$. Their data, however, are significantly higher than the standard values. The discrepancy was attributed to the free stream turbulence. Sivier[3] has measured the drag of magnetically supported spheres in a wind tunnel with a free stream turbulence intensity up to 8%, and reported a definite increase in C_D for $R_n > 200$, the increase growing with increasing R_n. However, for $R_n < 200$, he observed little or

no change in C_D compared to results at lower turbulence level ($\simeq 1\%$). His results are also considerably higher than the standard drag values. Zarin[4] refined the magnetic balance system used by Sivier and varied the free stream turbulence intensity level. Even at a turbulence level less than 1%, he found, for $R_n > 10^3$, drag to be markedly greater than the standard values. However, for $R_n < 10^3$, the results were in good agreement with the standard values. From this study Zarin concluded that in the higher Reynolds number range ($R_n > 10^3$), a small degree of free stream turbulence results in higher drag values.

Ross and Willmarth[5] conducted drag measurements for spheres moving rectilinearly through the glycerine-water mixture for $5 < R_n < 10^5$. Their results agree fairly well with the standard data for $R_n < 2 \times 10^3$ but are somewhat greater for the Reynolds number exceeding this value. The study revealed that the drag on a sphere is not significantly affected by the vortex shedding (5% variation). On the other hand, Baily and Hiatt[6] carried out sphere drag measurements in the ballistic range for $0.1 < M_n < 6$ and $20 < R_n < 10^5$. There is a reasonable agreement between their low speed data and the classical standard drag curve. Goin and Lawrence[7] studied subsonic drag on spheres in the Reynolds number range of 200-10,000 using a test range with controlled

environmental condition. The result showed compressibility effect on drag to be evident for the Mach number as small as 0.2.

Of some interest are the results of Vlajinac and Covert[8] in the laminar range of $2 \times 10^4 - 2.6 \times 10^5$. They found that the classical wind tunnel corrections as discussed by Pankhurst and Holder do not completely account for model size and wall interference. Although the authors do not specify actual test blockage values, their data show considerable variation from results by other investigators.

In the higher Reynolds number range of $5 \times 10^4 \leq R_n \leq 6 \times 10^6$, Achenbach's[9] contribution is significant. Based on the measured total drag, local static pressure and skin friction distribution he estimated positions of boundary layer transition and separation. Furthermore, the results substantiated a dependence of the friction force on the Reynolds number.

In another study[10], Achenbach has investigated the effect of surface roughness and tunnel blockage for the flow past spheres in the above range of Reynolds number. It was observed that an increase in roughness parameter leads to a decrease in the critical Reynolds number, however, the transcritical drag coefficient showed a definite rise. The blockage effect, in the range of 25-80%, was to cause an increase in both the drag coefficient and the critical

Reynolds number. Preliminary experiments showed the turbulence to initiate a premature transition from laminar to turbulent flow. These results, in general, substantiate the conclusions of an earlier investigation by Maxworthy[11] in a slightly different range of the Reynolds number ($6 \times 10^4 - 2 \times 10^5$), and the blockage variation over 5-25%.

It would be of interest to review here rather limited and conflicting information available on the frequency of separating shear layer, although Möller[12] initiated such a study as early as in 1938. A little later, in 1957, Commetta[13] extended Möller's study of the Strouhal number variation with the Reynolds number to $R_n = 5 \times 10^5$, but could detect periodic separation of vortices only up to $R_n < 4 \times 10^4$. More recently, Majumdar and Douglas[14] as well as Calvert[15] have reported vortex shedding from spheres in the Reynolds number ranges of $5.6 \times 10^3 < R_n < 1.16 \times 10^4$ and $2 \times 10^4 < R_n < 6 \times 10^4$, respectively. Calvert's results showed the base pressure coefficient to be substantially dependent on R_n with the variation of -0.270 to -0.356 over $R_n = 1.5 \times 10^4 - 6 \times 10^4$. The effect of trip wire was to shift the origin of the wake, leaving the scale unchanged. One must point out occasional discrepancies in results as reported by the different authors. For example, Möller measured, at $R_n = 10^4$, a Strouhal number of 2 while Majumdar

and Douglas reported the value an order of magnitude lower ($S = fD/U = 0.2$), which is the value typical of circular cylinders in cross-flow. It was also suggested that in a turbulent flow there is no regular vortex shedding. On the other hand, Commetta detected coexistence of vortex shedding in two modes: the lower mode at $S = 0.2$ and the higher mode, associated with transition of the vortex sheet from laminar to turbulent, at $S = 0.8 - 1.4$. Recent studies by Achenbach[16,17], in the Reynolds number range of $400 - 5 \times 10^6$ confirms Möller's results at lower Reynolds number, however, the lower critical Reynolds number was found to be 6×10^3. In the range $6 \times 10^3 < R_n < 3 \times 10^5$ strong periodic fluctuations in the wake flow were observed. Beyond the upper critical Reynolds number of 3.7×10^5 no periodic vortex shedding was detected.

Experimental investigation involving flow visualization and photographing of the wake behind a sphere in the low Reynolds number range of $5 < R_n \simeq 300$ was carried out by Taneda[18] using a water tank. The results showed that the critical R_n at which the permanent "vortex-ring" begins to form in the rear of a sphere is about 24, size of the ring is nearly proportional to the logarithm of the R_n, and the wake behind the ring begins to oscillate for $R_n \simeq 130$. Magarvey and Bishop[19] studied the transition ranges for

three dimensional wakes produced by the motion of a drop of an immiscible liquid in the Reynolds number range $0 < R_n < 2500$. They distinguished the observed wakes as steady or periodic with several subclassifications in each of the categories, and concluded (as can be anticipated) that the wake pattern depends entirely on the Reynolds number regardless of the liquid-liquid system employed. Furthermore, it was observed that the general values of the transition Reynolds numbers cannot be obtained as they depend on the drop deformation. However, for all the cases considered the transition in the wake patterns were limited to Reynolds number spread of less than 20. A qualitative interpretation of heat and mass transfer mechanisms in the wake region of a sphere in low speed flows ($R_n < 410$) is presented by Lee and Barrow[20] who employ measurements of the velocity field in the wake through flow visualization by dye injection. The observed flow patterns generally confirmed Taneda's results. An important characteristic of the near-wake is the reversed flow, at a velocity much smaller than the free stream velocity, along the axis of the sphere towards the rear stagnation point. The wake transition and Strouhal number for the incompressible wake of various bodies was studied by Goldburg and Florsheim[21]. Based on the experimental results, it was suggested that the transition could be approximately correlated for a range of spheres and cones

by the Reynolds number based on total wake momentum thickness. Furthermore, it was found that for regular vortex shedding the data for spheres and cones could be correlated with Rayleigh-Strouhal formula based on the same criterion.

Before moving to the review of analytical approaches, it would be appropriate to mention here a recent and rather significant contribution by Modi and Aminzadeh[22]. It is particularly relevant as the present project represents an extension of their investigation. Using a glycerol-water solution tunnel and by appropriately controlling concentration of the working fluid, the authors were able to correlate the progress of formation, elongation, asymmetry and instability of the vortex ring with the surface pressure distribution in the Reynolds number range of 70-6000. Of particular interest is a spectacular rise in the minimum pressure in the range $R_n = 240 - 275$, which was found to be associated with the onset of instability of the ring vortex leading to its periodic shedding. In general, Reynolds number effects were confined to the region near and downstream of the minimum pressure point. An extensive flow visualization program complemented their test data.

Theoretical investigation of even a steady viscous incompressible flow past a sphere is very complex. It was first considered by Stokes (1851)[23], and has been discussed by many authors since then. A large portion of these studies

have been concerned with the solutions for vanishingly small R_n.

Stokes solved the problem by neglecting the inertia of the fluid. Later, Whitehead[24] tried to improve upon this solution by introducing higher approximations to the flow when the Reynolds number is not negligible. But as is now well known, his solution is not valid in problems of uniform streaming[25]. Oseen[26] solved Whitehead's paradox by assuming that the sphere caused a small perturbation in the uniform parallel flow and neglected second order perturbation velocities, thus taking the inertia terms into account to a limited extent. Oseen's solution for linearized equationshas been improved by Goldstein[27], Tomotika et al.[28], and Pearcey et al.[29] However, as can be anticipated, linearization renders these analyses inadequate for $R_n > 2$.

Of considerable interest are two independent solutions: one by Kawaguti[30] who satisfied an integrated form of the Navier-Stokes equation for first and second-order terms when expanded by Legendre Polynomials and the other by Proudman and Pearson[25] who linearized the Navier-Stokes equation by two approximations, one valid at a distance from the sphere, and the other valid near the surface of the sphere. Kawaguti[31] has also developed an alternative procedure to solve the Navier-Stokes equation using the finite difference method. Unfortunately, the technique, valid for flow around

spheres up to $R_n = 20$, proves to be extremely labourious. Fox et al.[32,33] and Allen et al.[34] have partially alleviated this difficulty by transferring the technique into a relaxation procedure. On the other hand, Jenson[35] applied the relaxation method directly to the governing equations for vorticity and stream function in modified spherical coordinates to obtain solutions for flow around spheres at R_n = 5, 10, 20, 40. Hamielec et al.[36-38] have also used a similar method, but with finer grid size to obtain numerical solutions of the Navier-Stokes equations for slow viscous flow around spheres. Fourier expansions for the flow variables were used to solve the problem over a wide range of the Reynolds number by Dennis and Walker[39]. Rimon and Cheng[40] derived steady state solutions for $1 < R_n < 1000$ by impulsively starting a sphere from rest with uniform velocity and used a time dependent integration to carry the solution to the steady state. More recently, Dennis and Walker[41] have presented a series truncation method, first proposed by Van Dyke[42], employing a family of Legendre functions to solve the Navier-Stokes equations for flow around spheres in the Reynolds number range of 1-40.

1.3 Sphere Flow Field

From the brief literature review given above, important characteristics of the flow field associated with a sphere become clear. At a very low Reynolds number, $R_n < 0.1$, the flow near the sphere is dominated by viscous forces resulting in the fore-aft symmetry. In the range $0.1 < R_n \leq 24$, inertial effects increase with increasing Reynolds number and the streamline pattern no longer conforms to the above mentioned symmetry. The first evidence of flow separation near the rear stagnation point appears at a Reynolds number slightly greater than 20($R_n \simeq 24$), although there is some disagreement as to the precise value of R_n corresponding to its onset. The separation region grows with Reynolds number, as suggested by the growth of the vortex ring, accompanied by a reduction in its stability. In the range $R_n = 130 - 210$, oscillation of the bubble ensues and becomes gradually stronger.

For $210 < R_n < 270$, an asymmetrical separation bubble is observed, followed by discrete vortex loops shedding periodically from opposite side of the separation bubble in the range extending up to 700. The value of R_n at which the vortex shedding begins, often referred to as lower critical Reynolds number, signifies the appearance of a wake in which the flow around the sphere is no longer closed. The zig-zag or helical path of the free falling spheres at $R_n > 210$

is directly attributed to this character of the wake. It is of interest to note here that the angle between the rear stagnation point and the separation circle steadily increases from a value of zero at $R_n = 24$ to 72° at $R_n = 450$. The Strouhal number for sphere has been found to be around 0.2 for $5.6 \times 10^3 < R_n < 11.6 \times 10^3$.

Beyond the value of the lower critical Reynolds number, nature of the flow remains essentially the same until the Reynolds number (often referred to as the upper critical Reynolds number) of 3.7×10^5 is reached. Now the boundary layer upstream of the separation point changes from laminar to turbulent. The result is a rearward shift of the separation point, causing a decrease in the size of the separated region and characteristic sharp drop in the drag. No well defined vortex shedding frequency has been recorded beyond the upper critical Reynolds number.

The flow description so far relates to the "standard condition" devoid of turbulence, surface roughness, compressibility, rarefaction, and heat transfer effects. The last three parameters are not significant in the present study. In general, increase in turbulence intensity results in a systematic regression of the transition region towards lower Reynolds numbers, together with a moderate increase of the drag coefficient for both the subcritical and supercritical Reynolds numbers. At higher Reynolds numbers, surface

roughness affects the flow in the similar manner: it causes early transition to a turbulent boundary layer resulting in a range of Reynolds number over which the drag coefficient diminishes (compared to the standard drag curve values). However, it may increase the drag at low Reynolds numbers. Figure 1-1 briefly summarizes the scope of important contributions since a comprehensive review of the field by Torobin and Gauvin[1].

1.4 The Plan of Study

As pointed out before, an investigation aimed at studying the fluid mechanics of prosthetic heart valves has been in progress in this department since 1969. Primarily, the attention is focussed on the Starr-Edwards configuration, which essentially consists of:

(i) a metal cage of highly polished uncoated casting of Stellite 21, a cobalt alloy noted for high strength and corrosion resistance;

(ii) a spherical ball of silicone rubber with diameter ranging from 1.2 - 2.2 cm;

(iii) a metal seat normally called orifice;

(iv) a sewing margin of knitted Teflon cloth.

The main objective has been to identify factors causing:

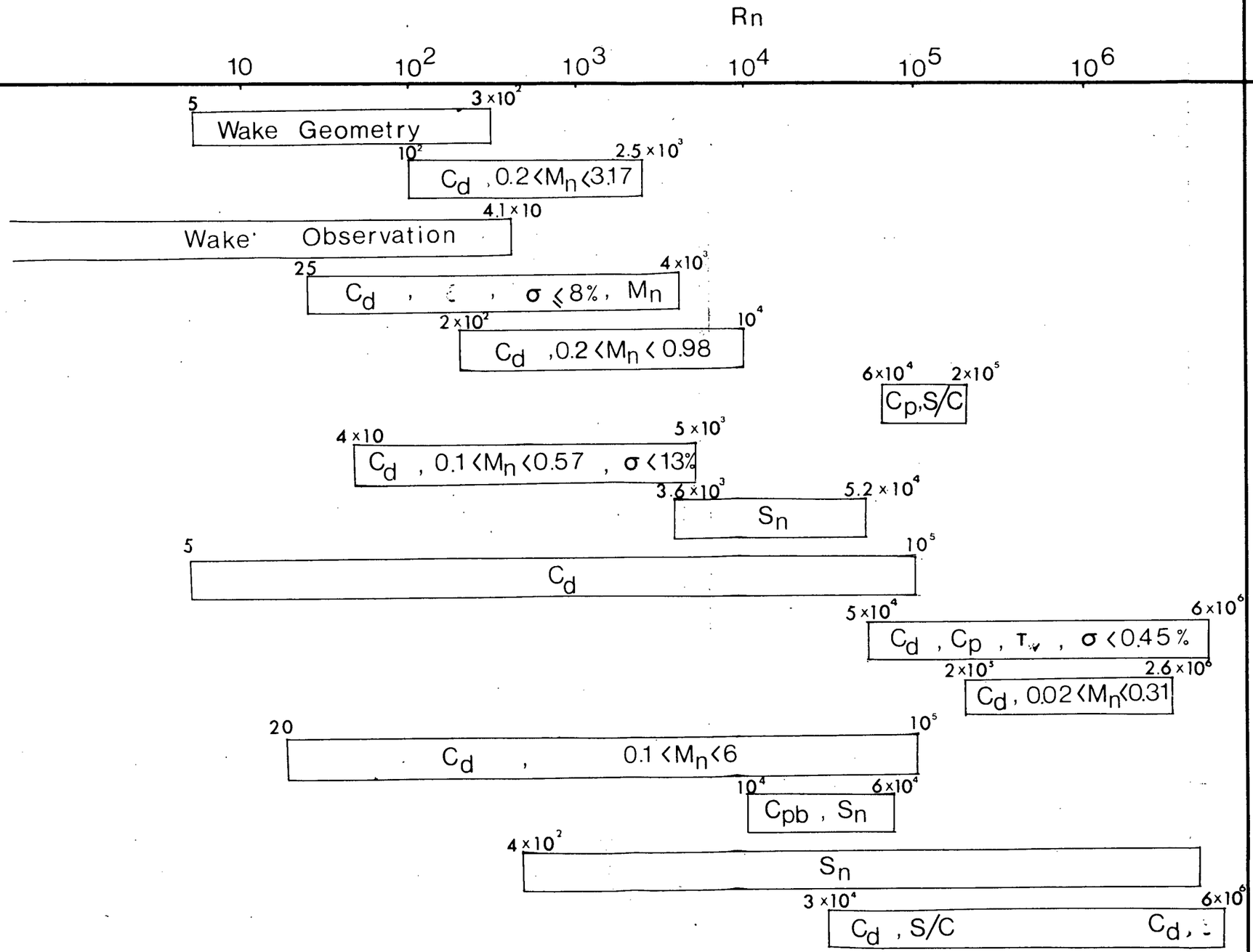

Figure 1-1 A summary of literature indicating the scope of recent important contributions in the field of flow past a sphere.

Taneda[18] [1956]

Heinrich et al.[2] [1965]

Lee & Barrow[20] [1965]

Sivier[3] [1967]

Goin & Lawrence[7] [1968]

Maxworthy[11] [1969]

Zarin[4] [1969]

Mujumdar & Douglas[14] [1970]

Roos & Willmarth[5] [1971]

Achenbach[9] [1972]

Vlajinac & Covert[8] [1972]

Bailey & Hiatt[6] [1972]

Calvert[15] [1972]

Achenbach[17] [1974]

Achenbach[10] [1974]

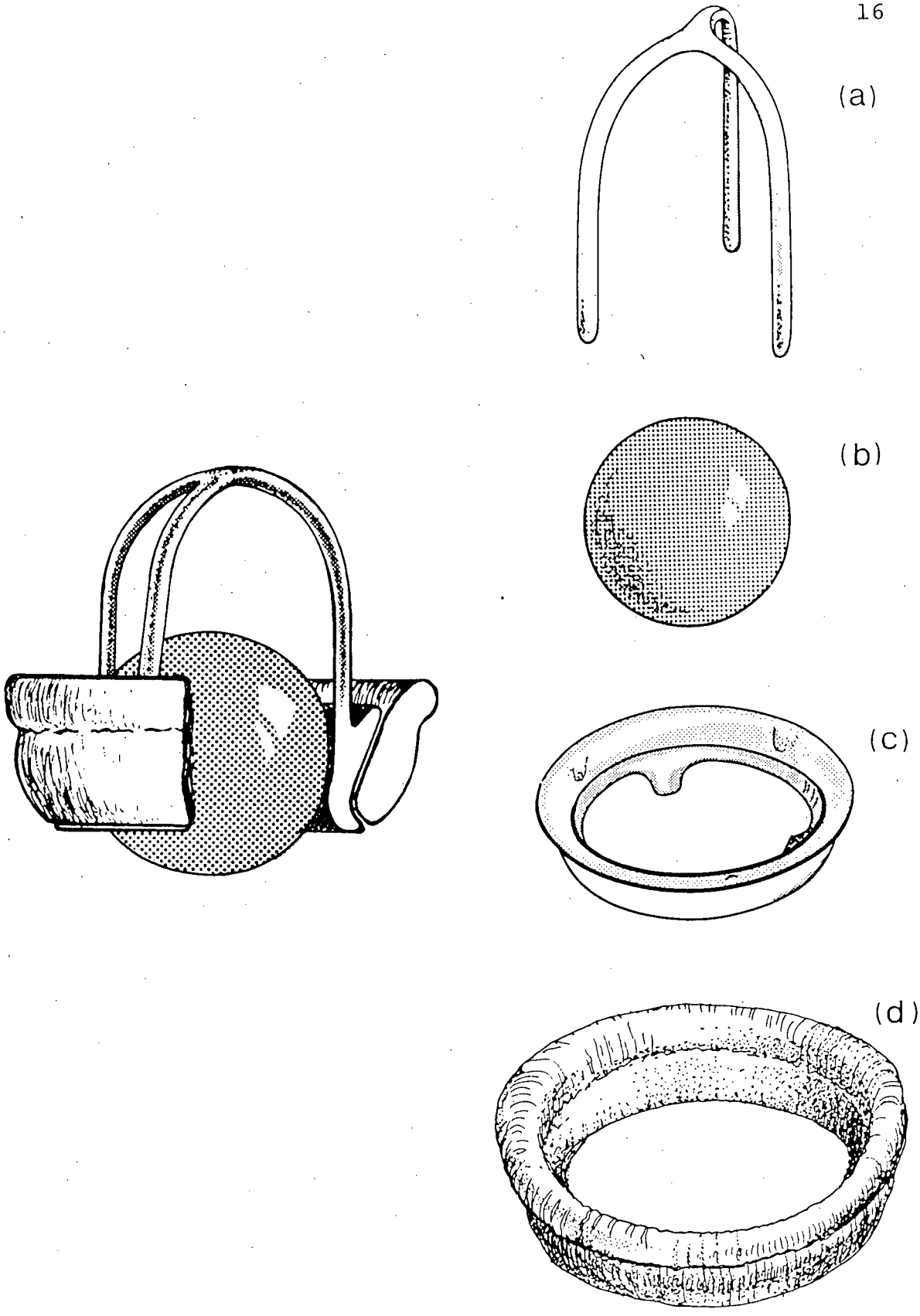

Figure 1-2 Starr-Edwards prosthesis and its exploded view: (a) cage; (b) ball or poppet; (c) seat; (d) suture ring

(a) destruction of red blood cells;

(b) dissociation of the blood constituents and their deposition on the cage resulting in the valve failure.

Suitable modifications in the valve geometry that would alleviate or at least minimize these problems and lead to an improvement in the valve performance were also of interest.

The fluid dynamics of bluff bodies in pulsatile flows at low Reynolds number represents a challenging task. Hence one is forced to approach the problem in stages of increasing difficulty. Although studies by Aminzadeh and Modi[22,43-47] have provided considerable useful information, there are a number of aspects to the problem which remain unexplored. One of them pertains to the effect of blockage as imposed by the poppet of the Starr-Edwards valve occupying aortic position (Figure 1-3).

Depending upon the size of the aorta and prosthesis, the blockage offered by the poppet may be substantial[47] leading to a large change in the flow character. With this as background, it was decided to explore wall effects on such a heart valve prosthesis in the pulsatile flow representing a cardiac cycle. However, a detailed literature review revealed that the corresponding information for a sphere by itself even in a uniform flow in the Reynolds number range of interest remains unrecorded.

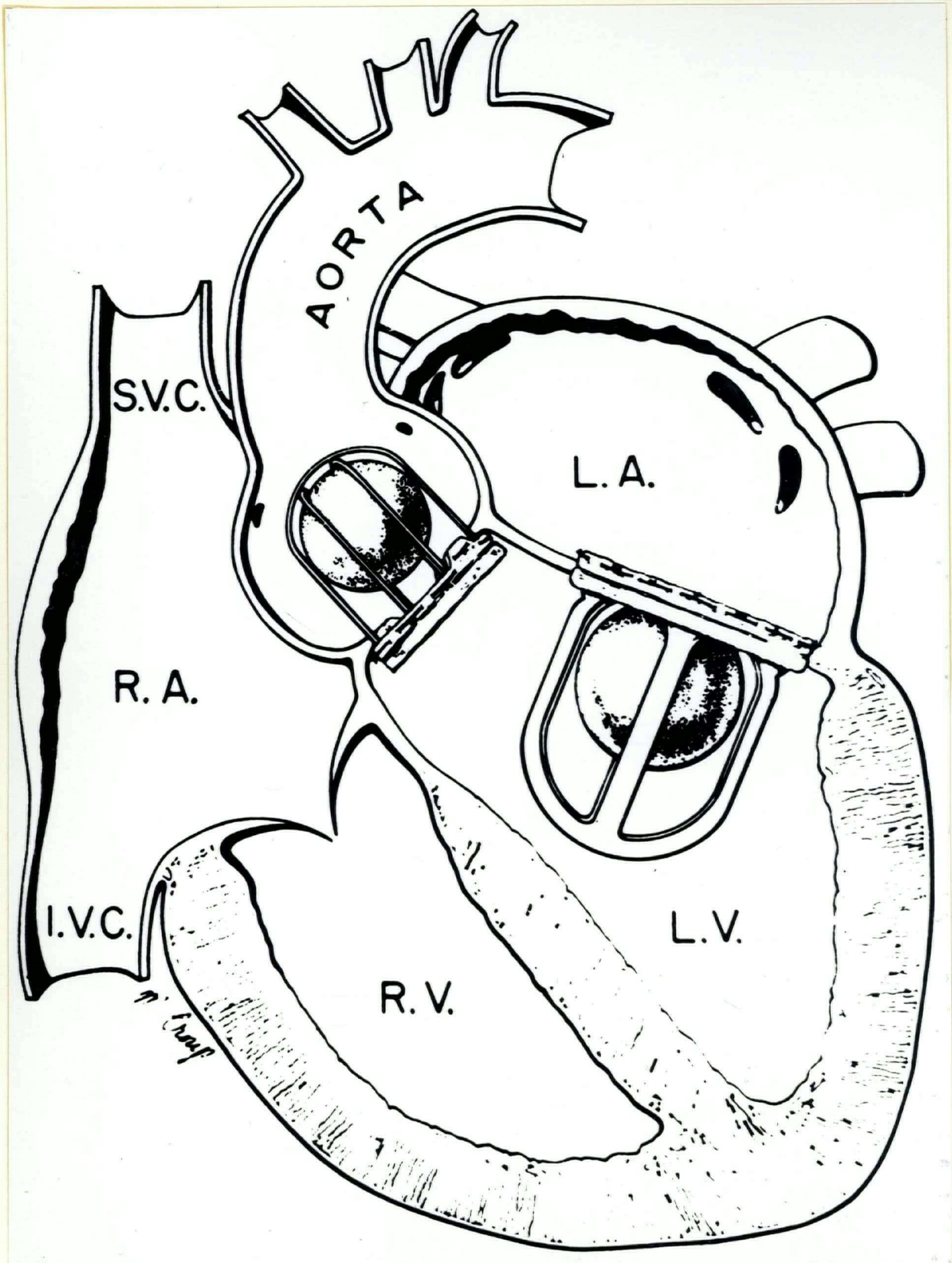

Figure 1-3 A schematic diagram showing the Starr-Edwards prosthesis occupying aortic position and presenting a large blockage

This thesis, therefore, studies:

(i) formation, development and instability of vortex ring;

(ii) associated pressure distribution;

(iii) drag; and

(iv) near wake geometry

for a family of spheres representing blockage ratio of 3 - 30% in the Reynolds number range of 30 - 2000.

In the beginning, the effect of stem used in supporting the spheres is systematically investigated, which provides a criterion for their selection. This is followed by a detailed study of the surface pressure distribution and drag. An approach to data reduction, so critical at low Reynolds number, is discussed and its merit assessed compared to the conventional procedure. Finally, the test results are analyzed as functions of the confinement condition and Reynolds number. An extensive flow visualization study in conjunction with still and high speed movie photography complements the test program. Figure 1-4 summarizes the plan of study.

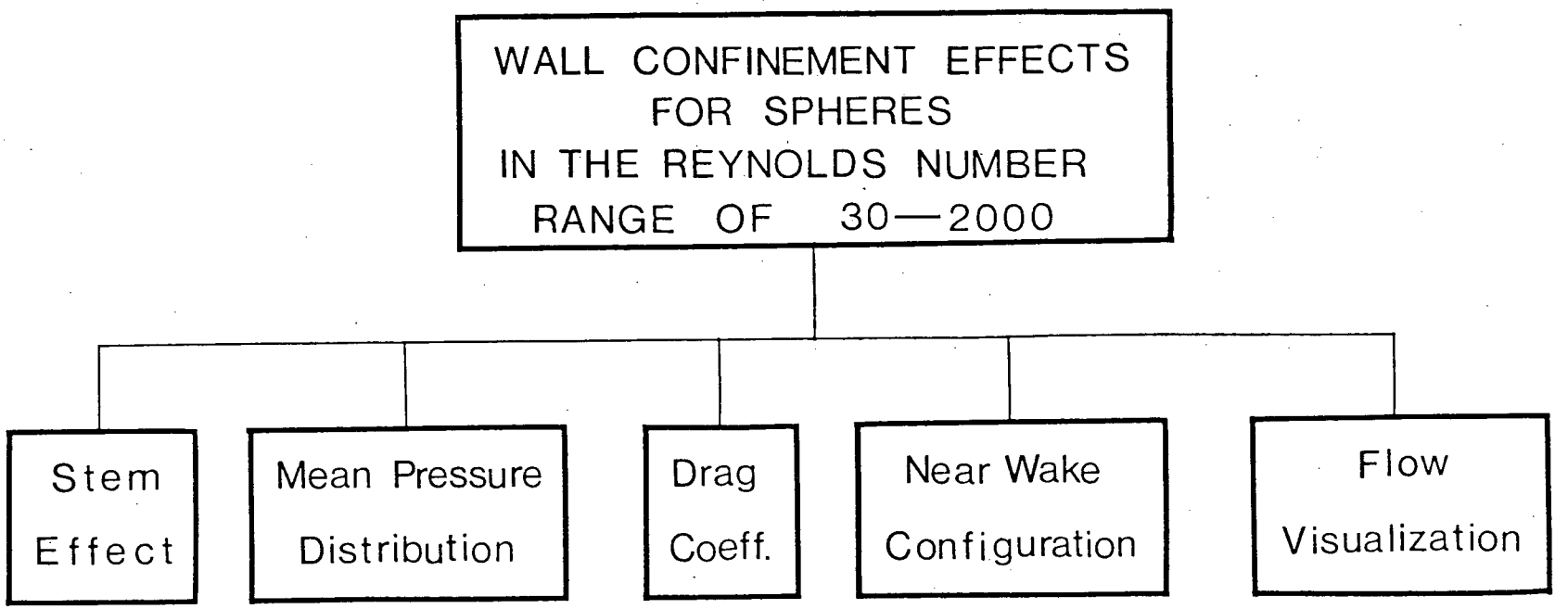

Figure 1-4 The plan of study

2. EXPERIMENTAL APPARATUS AND TEST PROCEDURES

This chapter introduces the test facilities used in the experimental program. Some of the instrumentation employed constitutes the standard equipment in any well equipped fluid mechanics laboratory and hence needs no elaboration. On the other hand, design and constructional details involved in the development of specific equipments are often numerous and hence, though important and relevant, cannot be covered in their entirety. The attention is, therefore, focussed on more salient features.

The test procedures employed are conceptually well known but their implementation often attain complexity of a higher order, mainly because of the character of the working fluid (glycerol-water solution). Often peculiarities of specific experiments make certain measurements quite difficult. Throughout, the emphasis is on practical considerations involved in executing the experimental programme. At times the factors involved are,seemingly, so trivial that one would seldom give them a second look. However, a common experience of most experimenters is that resolution of apparently simple problems occasionally takes days, if not weeks or months. This is particularly true in the case where liquid is the working fluid.

The glycerol-water solution tunnel representing a fundamental facility for the entire test program and its

calibration using the hot-film anemometry are described first. This is followed by an introduction of the models and their support system. Next, the highly sensitive pressure transducing system capable of determining surface pressure distribution is discussed leading to the arrangement used in drag measurements. Finally, details of the flow visualization procedure, which proved extremely useful in obtaining physical appreciation as to the character of the flow, are presented. Wherever appropriate, calibration procedures employed are explained and corresponding charts included.

2.1 Glycerol Tunnel

The tests were conducted in a glycerol-water solution tunnel designed to produce Reynolds number in the range 30 - 6000 (based on sphere diameter and representative average velocity in the test-section). The choice of concentration of the working fluid provided a degree of flexibility, but only to a certain extent, as governed by the characteristics of the power unit. Primarily the tunnel consists of three subassemblies: the test section; the fluid return system; and the power unit consisting of a pump and a drive motor.

The test-section is built of four plexiglas walls 2.44 m (8 ft) long, 1.9 cm (0.75 in) thick and wide enough to produce an inside cross-section of 20.32 cm x 20.32 cm (8 in x 8 in).

Deflection annular vanes together with several sections of honeycombs, brass screens and nylon wool gave exceptionally flat velocity profiles. There are three accesses to the inside of the test-section, through each end and via a port-hole at the top. The porthole, 12.7 cm (5 in) in diameter, is judiciously located 0.84 m (33 in) from the entrance to admit arm to reach, position and adjust models. In addition, several smaller portholes which could take 1.6 cm (5/8 in N-C) plugs were drilled and tapped in the top wall of the test-section. These openings were used to mount models, take out pressure conducting lines and to support a hot-film probe in the test-section. Two glass plates, 63.5 x 14 x 1.27 cm (25 x 5 1/2 x 1/2 in), recess-mounted in the sides of the test-section provided optically flat, homogeneous and thermally stable walls for inspection and photography.

Located between the end of the plexiglas test-section and the power drive system is the return section essentially comprising of heat exchanger, Polyvinyl Cloride (PVC) pipes and elbows with connecting flanges and radiator hose. A copper pipe, 3 m x 7.62 cm (10 ft x 3 in), in conjunction with a 2.4 m x 15.24 cm (8 ft x 6 in) PVC plastic pipe formed an annular single pass heat exchanger. With the coolant supplied by a water main, it was possible to maintain temperature of the working fluid within ± 0.2°C. PVC elbows and sections of the radiator hose provided relatively easy,

anti-corrosion and vibration free connection between the test-section and heat exchanger.

The power unit consists of a centrifugal pump: Aurora type GAPB, 12.7 ℓ/s (200 gal/min), 7.6 m head, 1750 rpm. It is driven by a three horsepower variable speed d.c. motor. The pump impeller and housing are of cast brass to guard against possible corrosion. The motor is energized by a three phase grid, the voltage being adjusted through an autotransformer and rectified by selenium diodes. No further smoothing of the d.c. output was required.

It was important to minimize dirt contamination of the tunnel fluid. This was achieved by incorporating a 10 μ filter in a bypass circuit across the pump. The system filters the entire volume at least once in twenty-four hours of operation. The tunnel is schematically shown in Figure 2-1.

Flow rate in the tunnel was monitored using a sharp edge orifice plate mounted 0.61 m (2 ft) upstream of the pump inlet. The plate location was so selected as to make its reading relatively independent of the upstream and downstream disturbances in the form of elbows, change in section at the pump inlet, pump suction, etc. Before final assembly the orifice plate and associated plumbing were calibrated, under simulated test conditions, by pumping water from a large sump into a weighing tank. The calibration plot thus obtained is presented in Figure 2-2.

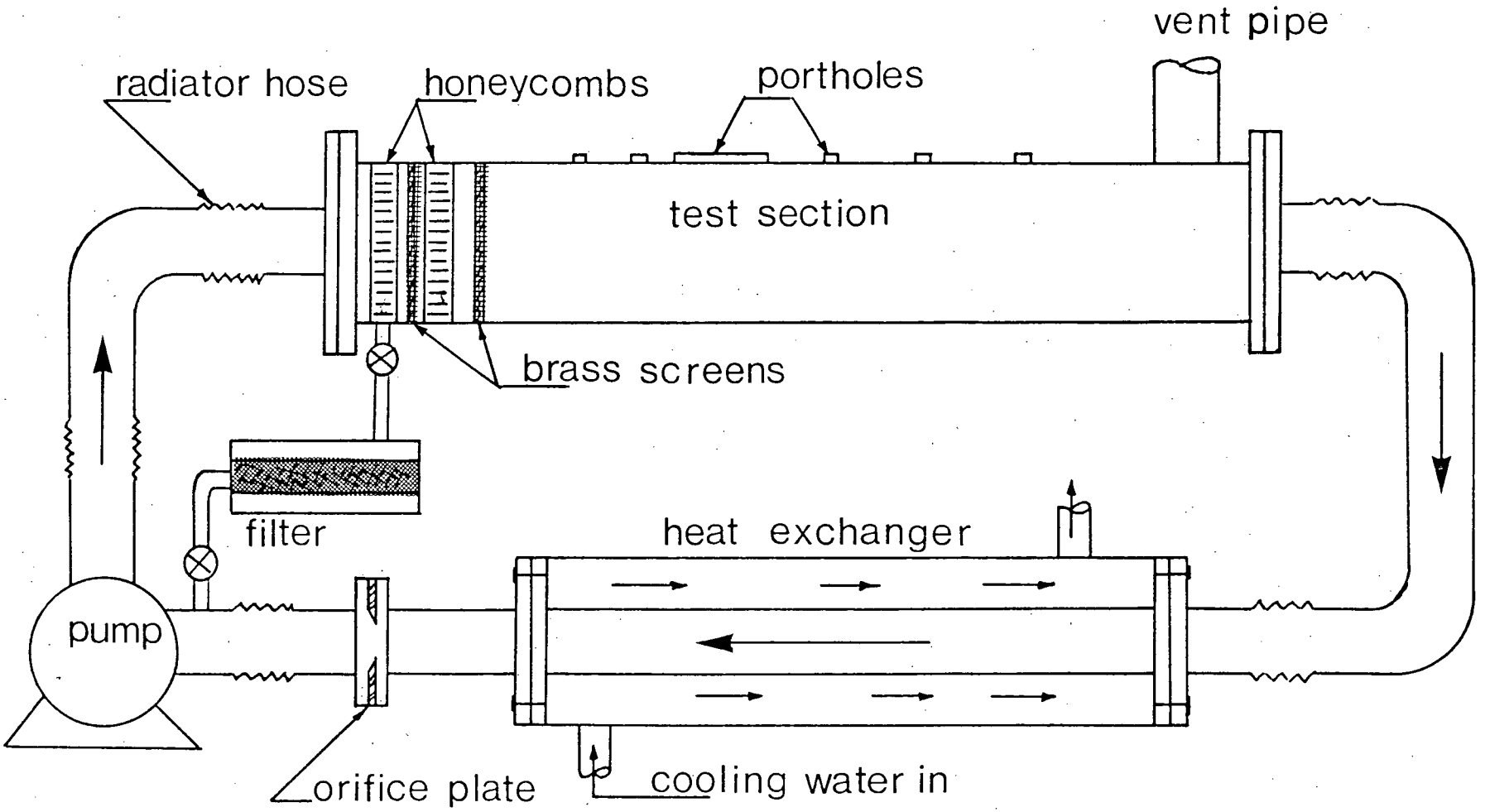

Figure 2-1 A schematic diagram showing the glycerol-water solution tunnel

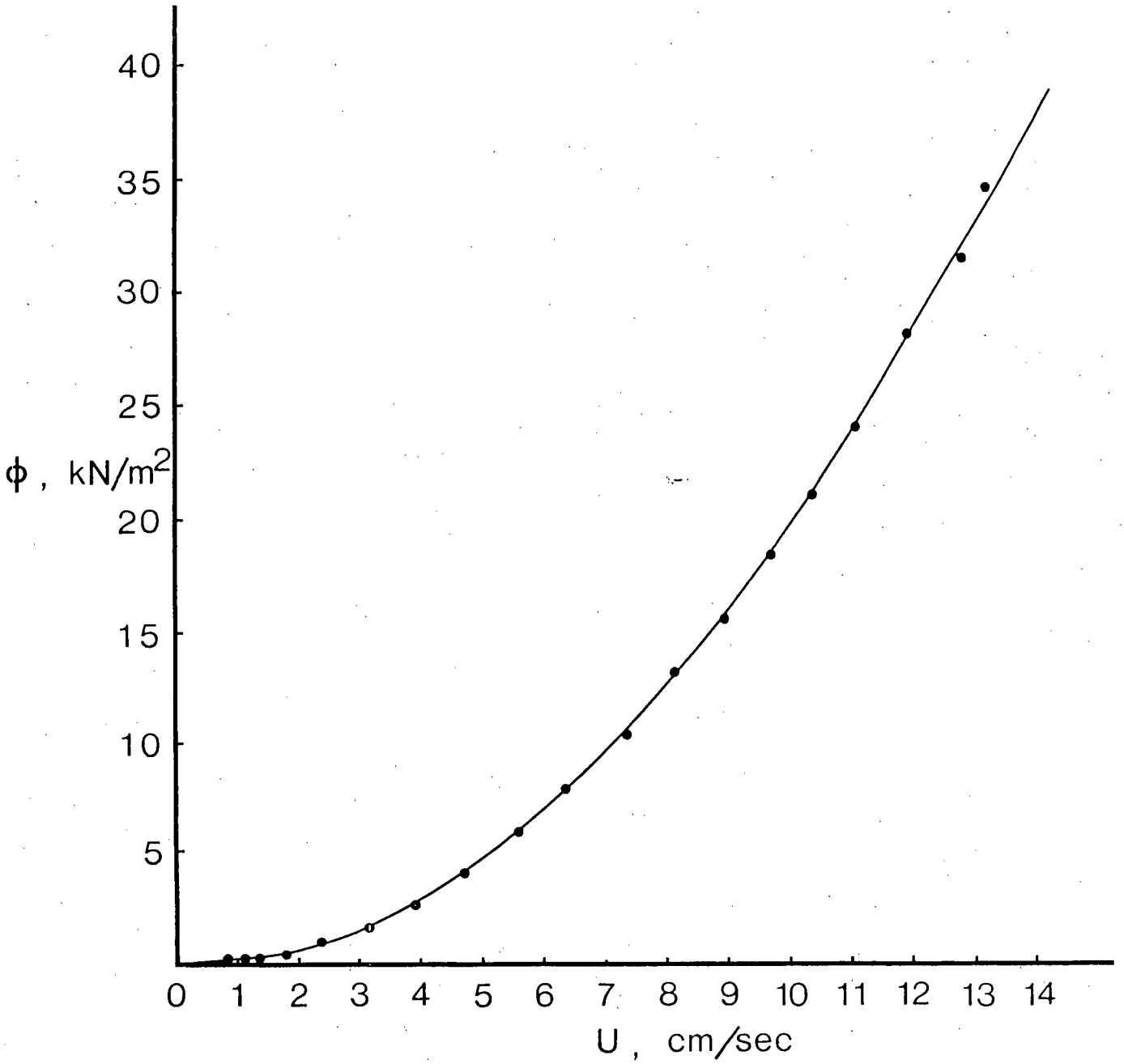

Figure 2-2 Calibration plot for the sharp edge orifice meter

2.2 Hot Film Anemometry and Velocity Profiles

As mentioned before, an average velocity in the test-section was determined from the volume flow rate given by the orifice meter. However, during the course of the experimental work it was also required to measure velocity profiles and, in particular, the centerline velocities in the range of 2.5 - 15 cm/s. Measurements of fluid velocities at low values of Reynolds number has long been known to be exceptionally difficult.

Apart from laser-doppler anemometer, which was still in the early stage of acceptance when calibration of the tunnel was undertaken (1973), a hot film probe appeared to meet the requirements of high resolution in time and space of flow velocities quite adequately. Hence a quartz coated wedge shaped platinum film probe (Thermo-Systems Inc., model 1239W) was used in conjunction with the standard constant temperature anemometric equipment (DISA model 55A01). Despite the existence of a comprehensive literature on measurements in gases, relatively few papers deal with the use of hot film anemometry for investigation of slow liquid flow. It is mainly because of several difficulties involved in adapting the anemometer to use in water or other liquids:

(i) Electrolysis is by far the worst source of trouble causing corrosion of the probe, generation of gases and instability in the

electronic control circuitry. This particular problem does not arise in non-conducting liquids, such as distilled water or kerosene. Another way of avoiding serious corrosion could be the use of high frequency alternating current to heat the probe, and/or coating the probe to provide electrical insulation from the liquid.

(ii) Often the formation of bubbles on the sensor causes incorrect and unstable operation of the probe[48]. Bubble formation can be reduced by cleaning the probe in a solvent, e.g., methyl alcohol, with the anemometer in "stand-by" condition, and/or by adding some surface reactants to reduce fluid's surface tension, thus preventing the formation of bubbles and their attachment to the sensor. In the case of water a "wetting agent" (Kodak Photo-Flo 200) can be used.

(iii) Contamination of the probe by dust particles or other deposits reduces and modifies its sensitivity[49]. To eliminate dirt contamination the surface of the liquid should be shielded. Continuous filtration of a part of the circulating fluid should also help in minimizing the problem. Both these methods and frequent cleaning of the probe were found necessary in the present set of experiments.

There are many ways to calibrate hot-film probes[50,51]. The choice of method depends on the availability of a suitable standard of comparison, the ease of measurement, and the desired degree of accuracy. In most cases, the velocity measured by mechanical means at a specific point in the fluid field is compared with the electrical signal of the anemometer. The degree of accuracy then depends mainly on the accuracy with which the reference velocity is known.

In the present case the probe was held stationary in a rotating dish, 30.5 cm diameter and 25.4 cm high, mounted horizontally on a turntable with infinitely variable speed drive (Figure 2-3). This arrangement was found satisfactory over the velocity range of interest. Sufficient time had to be allowed for a quasi-steady state of motion to be set-up[52]. The motion obtained was very closely solid body rotation when the probe was not too far from the cylindrical or bottom walls of the dish. The circular dish had to be sufficiently large to allow for the dissipation of vorticity generated by the probe between successive passes; obviously the time constant of this effect is of the order ν/r^2 (r = distance from the probe to the axis of rotation)[53]. Absolute cleanliness was found to be essential in these tests. The complete rig was kept in a glass enclosure which greatly reduced the frequency of probe cleaning required to produce repeatable results.

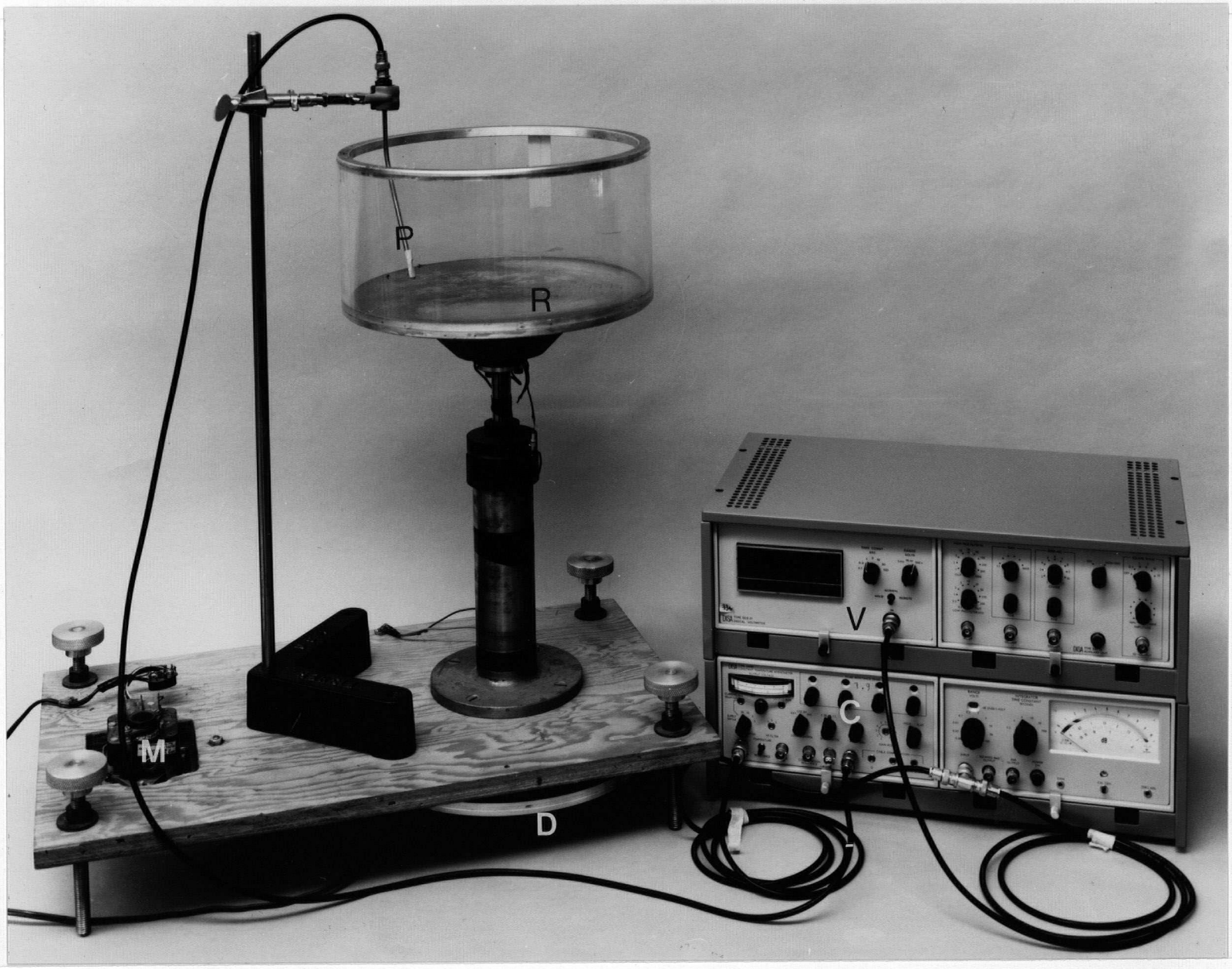

Figure 2-3 A photograph showing the rotating dish arrangement used in calibration of the hot-film probe: C, constant temperature anemometer; D, drive wheel; M, drive motor, P, probe; R, rotating dish, V, d.c. digital voltmeter

Calibration tests were carried out in the glycerol-water solution of concentration 55.7% by weight (Figure 2-4). As anticipated, the experimental points clustered around a straight line down to quite low values of the true velocity. The indicated straight line is a least mean square fit through the measured data. The maximum deviation from the fit is 2.3% for the overheat ratio of 0.097. The scatter in the experimental results is of the order that can be expected from the ancillary equipment alone.

Since the hot-film temperature T_m is kept constant by virtue of the overheat ratio, a change of R_c (probe's cold resistance) during the measurements would imply a change of T_m. It is, therefore, useful to investigate drift in the overheat ratio induced by variations in R_c. This would give some appreciation as to the changes in the ambient temperature that can be tolerated during a given test.

To this end, dependence of probe cold resistance on fluid temperature was measured using a constant temperature bath. Figure 2-5 shows these results for various concentrations of glycerol solution. All the curves have almost the same slope suggesting the constant coefficient of resistivity. In the worst case, the maximum deviation was observed to be about 1.2%.

The first step in the test programme was to calibrate the tunnel, i.e., to obtain information about the

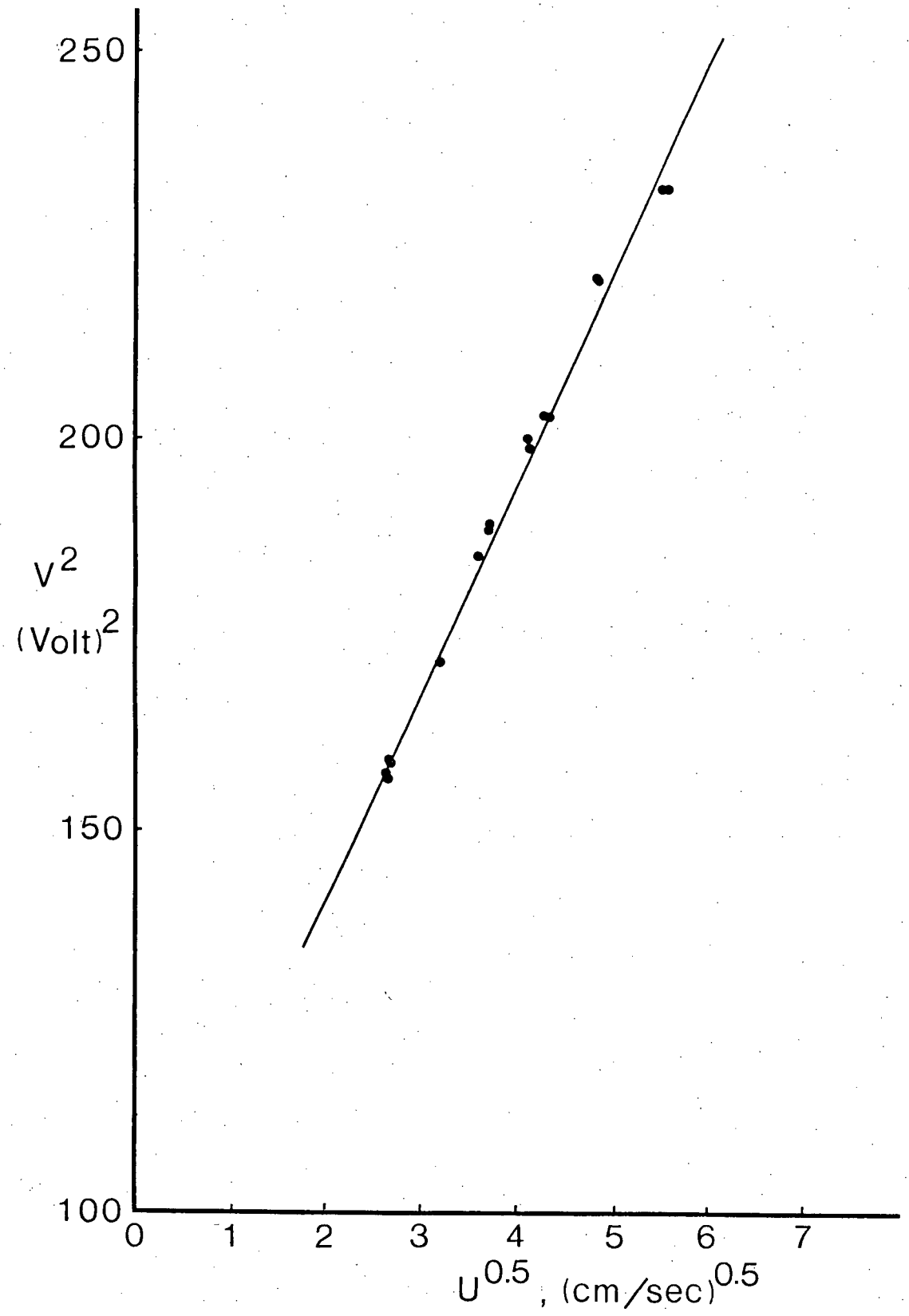

Figure 2-4 Calibration data for hot-film probe in the glycerol-water solution of C_n = 55.7%

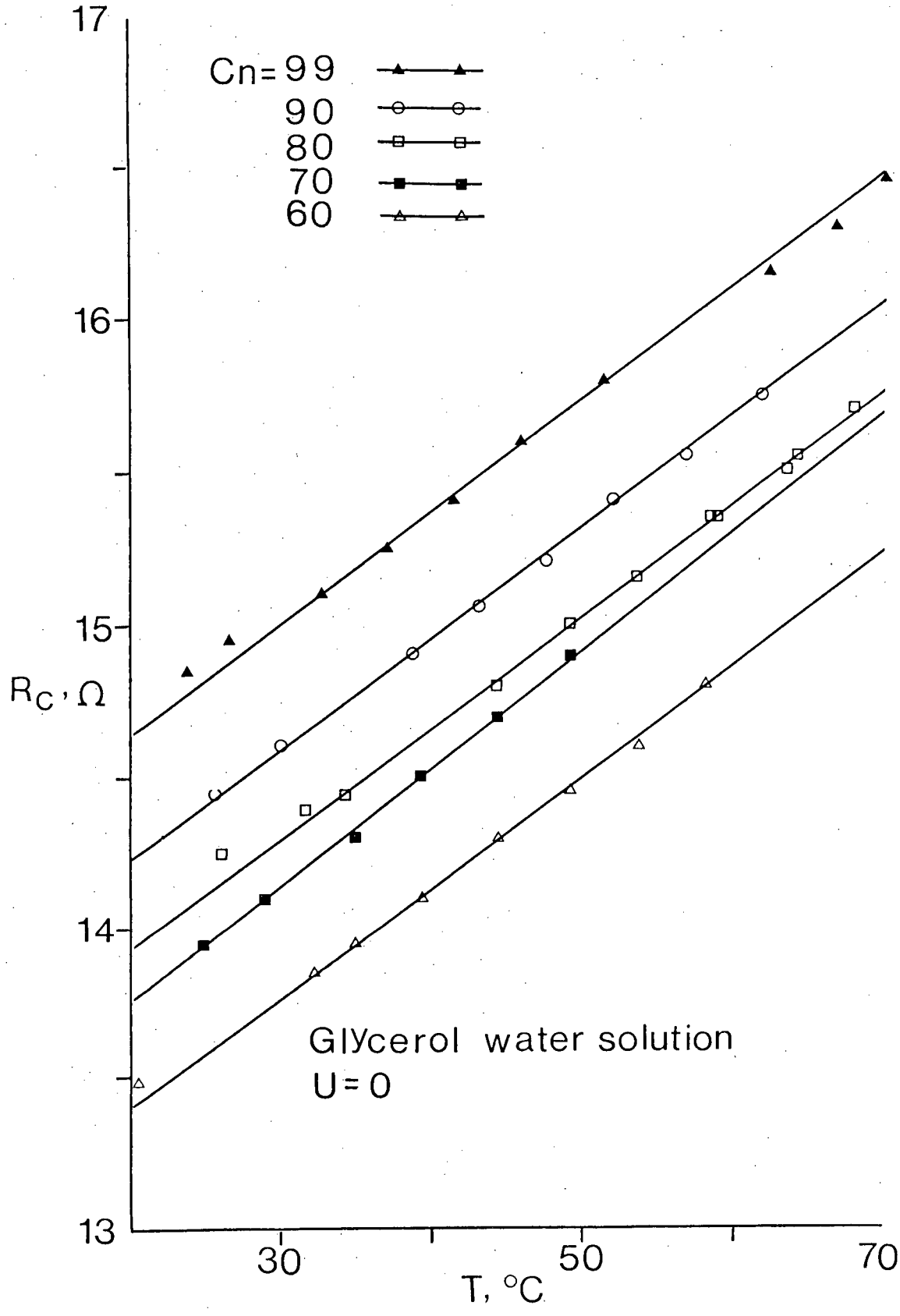

Figure 2-5 Calibration plots showing the effect of temperature on probe's cold resistance when immersed in glycerol-water solution of different concentration

boundary layer growth as reflected in the velocity profiles along the test section. To this end, the tunnel was filled with the working liquid of a fixed concentration. All air pockets and bubbles were removed from the tunnel by circulating the test fluid, with the wetting agent, for at least eight hours at around 30°C. Velocity profile at a given station was then obtained using the calibrated hot film probe in conjunction with a traversing gear, which can position the probe with an accuracy of around ±0.25 mm. It should be pointed out that the probe movement is confined to the vertical direction in the central plane of the tunnel. Step size for the probe movement was regulated according to the velocity gradient so as to provide an accurate profile near the wall. Figure 2-6 shows instrumentation layout used during the velocity profile measurements.

Velocity profiles were measured at a station 83 cm down stream of the entrance to the test section ($y_p = 83$ cm) in the Reynolds number range of 960 - 3900 based on the hydraulic diameter of the test section and the average velocity as deduced from the flowmeter data. Two distinct cases were considered: tunnel without a model and with models of different blockage ratios located at $y_m = 100$ cm. Typical plots are presented in Figures 2-7 and 2-8. It is apparent that the velocity profile is essentially flat at least over the central 15 cm of the tunnel height. The

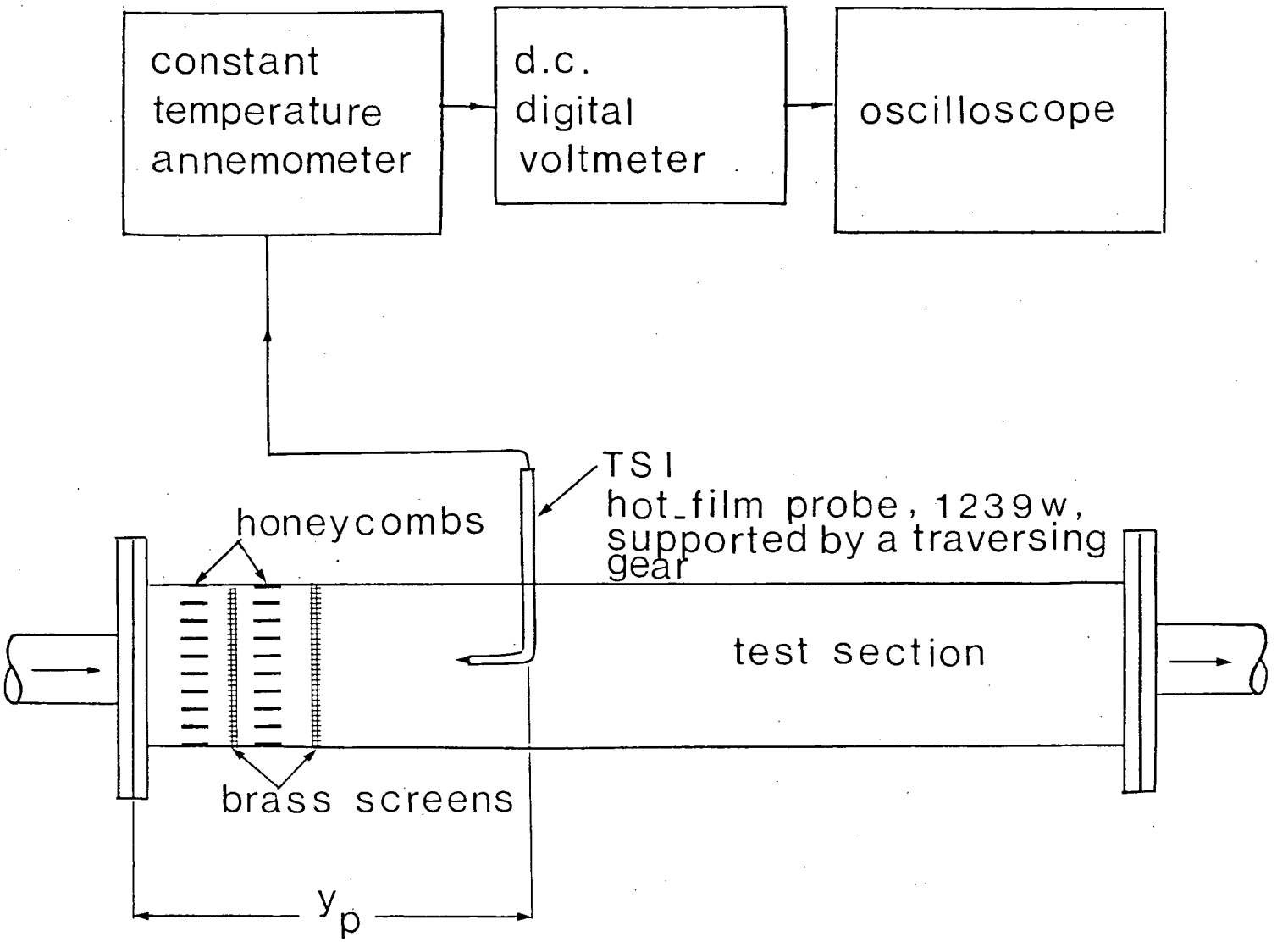

Figure 2-6 Instrumentation layout used during velocity profile measurements

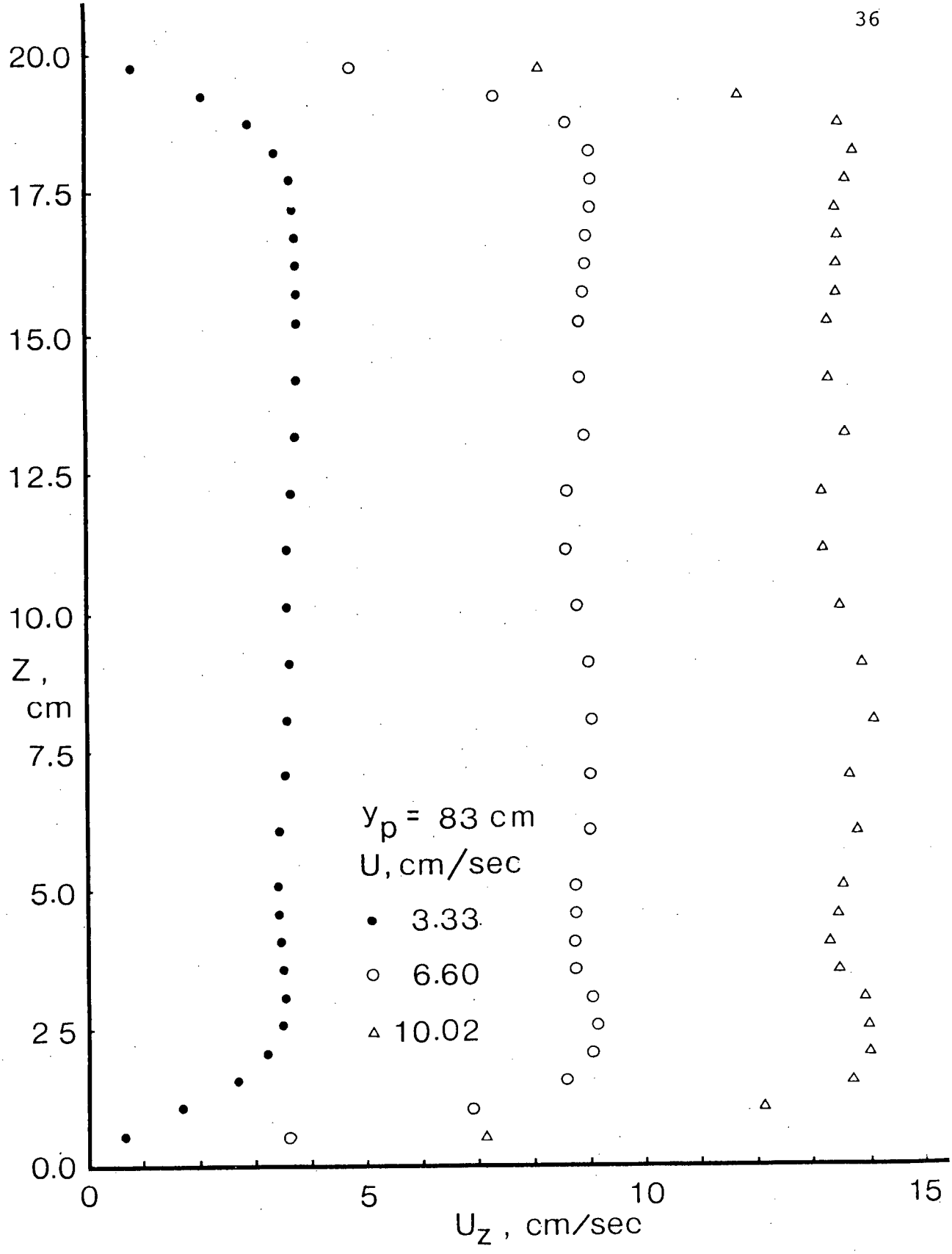

Figure 2-7 A set of typical velocity profiles at the station y_p = 83 cm in absence of the spherical models

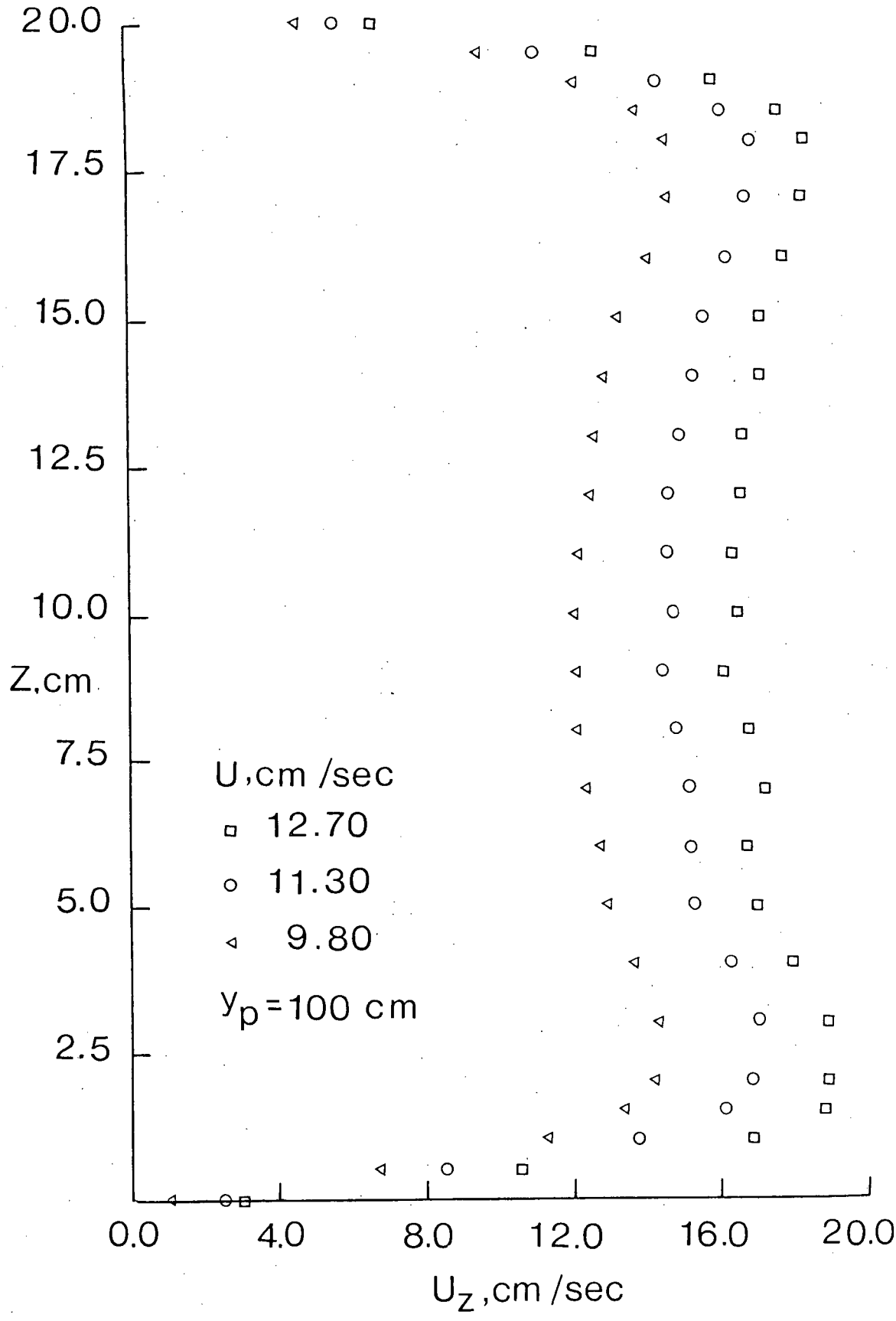

Figure 2-8 Effect of wall confinement on the upstream velocity profile: (a) S/C = 7.6%

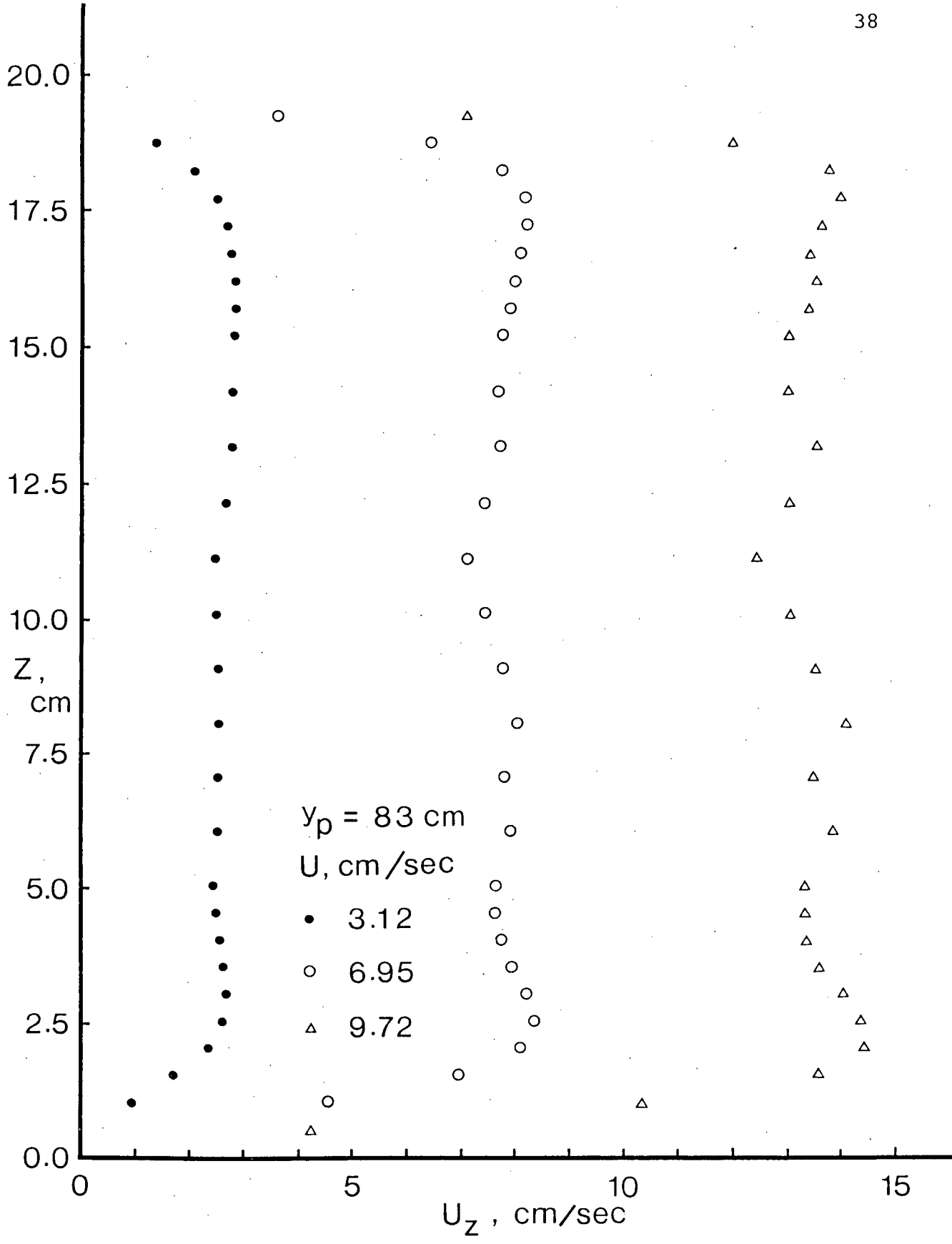

Figure 2-8 Effect of wall confinement on the upstream velocity profile: (b) S/C = 30.6%

presence of the model does affect to some extent its uniform character, however, the maximum deviation from the average value was found to be less than 8%. As we will see later, any variations in the velocity profile can be accounted for by a modified definition of the pressure coefficient. For the purpose of comparison of the experimental results with available information in the literature, it was also necessary to have details of centerline velocity over the operating range of the mean flow. This is shown in Figure 2-9. It is interesting to note that at a very low value of the average velocity (based on flowmeter data, $U < 3$ cm/s), the centerline velocity (U_c) is essentially the same as U. However, with an increase in the flow rate, the ratio U/U_c gradually drops and tends to attain a uniform value of around 0.74.

2.3 Models and Support System

A family of seven spheres ranging in diameter from 3.8 - 12.7 cm were carefully machined from plexiglas with a tolerance of 0.0025 mm. Any deviation from sphericity was checked using two procedures:

(i) micrometer;

(ii) projecting a photograph of the model on a screen.

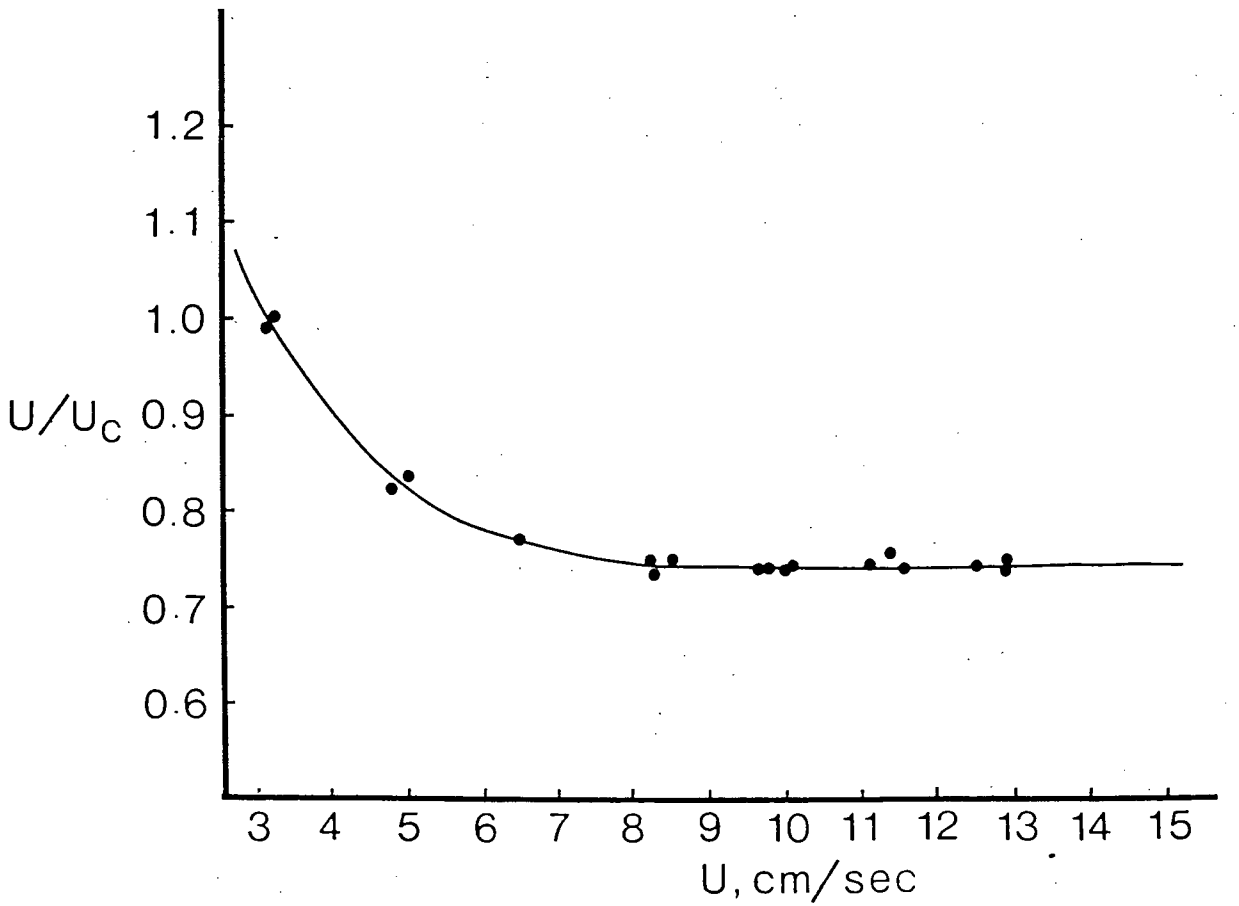

Figure 2-9 Variation of the centerline velocity as measured by the hot-film probe with the average velocity as given by the flowmeter data

Maximum deviation from the mean diameter was found to be less than 0.18%. The accuracy was considered quite adequate for the test program. Figure 2-10 shows the models, their dimensions and the resulting blockage ratios.

As against construction of the models, which turned out to be relatively simple, the design of their support system presented several interesting problems from fluid dynamics considerations. Ideally one would like to hold a model in position without introducing any supporting structure in the fluid field. Although such 'non-contact' magnetic support systems are available commercially, they tend to be prohibitively costly. One is, therefore, forced to turn to conventional stem type of support. This poses two questions:

(i) What is the desirable orientation of the stem relative to the fluid field?

(ii) What is the effect of a stem on the fluid field? To put it differently, what is the criterion for selection of the stem size so that its effect on the fluid field becomes negligible?

A horizontal stem lying in the wake of the model appears attractive, however, it suffers from two disadvantages. Here, to cover the spherical surface, pressure taps would be required on the horizontal meridional section,

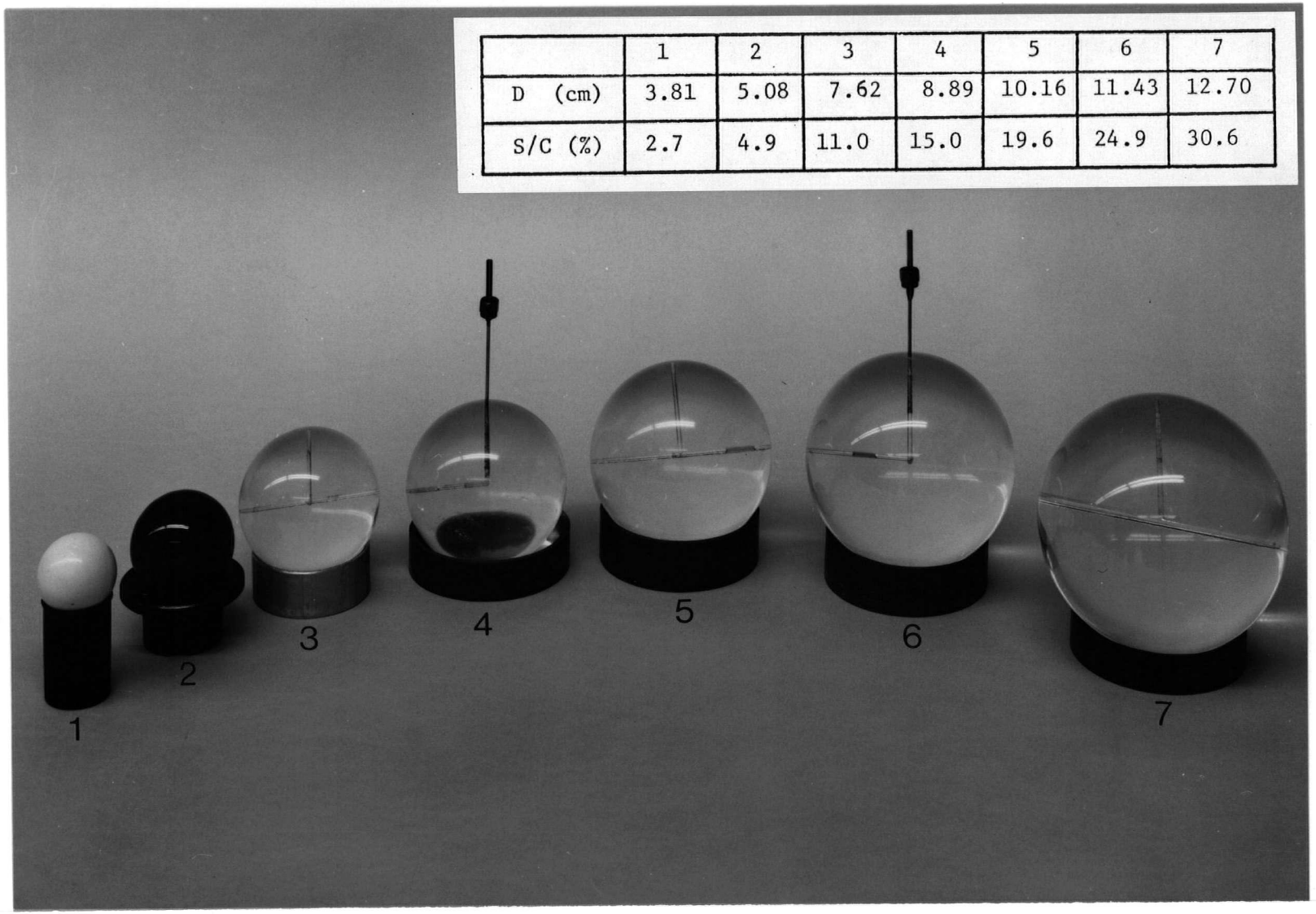

	1	2	3	4	5	6	7
D (cm)	3.81	5.08	7.62	8.89	10.16	11.43	12.70
S/C (%)	2.7	4.9	11.0	15.0	19.6	24.9	30.6

Figure 2-10 A photograph showing spherical models used in the experimental program covering the blockage ratio range of 2.7 - 30.6%

the number of pressure taps being governed by the desired accuracy of the pressure plot. The stem may be used to convey the pressure tubings, hence its size would be a direct function of the number of pressure taps used. Preliminary experiments with tubes of different diameters suggested that the inside diameter should be at least 1.3 mm to have reasonable time constant (< 5 minutes). Considering a minimum number of pressure taps to be fifteen (this is grossly inadequate to precisely describe local variations; as will be seen later, actual experimental program recorded pressure at thirty locations to provide a well-defined profile), leads to inside diameter of the stem to be at least 2 cm, i.e., the outside diameter of around 2.4 cm! Obviously this is unacceptable when the smallest sphere has a diameter of 3.8 cm. Furthermore, the stem would interfere with the near-wake, one of the items of interest in the present study.

On the other hand, a vertical stem support presents an attractive alternative. A single pressure tap, through a systematic rotation about the vertical axis, can cover the entire horizontal plane and hence, through symmetry, the entire surface of the sphere if located on the horizontal meridional section. Furthermore, the stem, if connected to the tap, can serve as a conduit for transferring the pressure signal to an externally located transducer. However, we still need to answer the question concerning an

appropriate size of the stem that would not disturb the pressure field.

To arrive at a criterion for stem size, an extensive test program with four stems of equal inside diameter (d_i = 1.32 mm) but varying outside diameter (d_o = 1.58, 4.76, 6.35, and 12.70 mm) was undertaken using two spherical models of diameters 5.08 and 6.35 cm. The results are presented in Figures 2-11 to 2-13. The effect of outside stem diameter on pressure profiles at a given Reynolds number as plotted in Figure 2-11 clearly shows that a stem diameter $\leq$ 4.76 mm does not affect the data substantially. Furthermore, the stem effect seems to be essentially independent of the Reynolds number in the range investigated (Figure 2-12).

The results on minimum pressure and the base pressure when plotted against the outside stem diameter to sphere diameter ratio (d_o/D) clearly establish its critical value as shown in Figure 2-13. Note that for $d_o/D \leq 0.1$ the stem effect is virtually negligible. In the present test-program, depending on the size of the sphere, d_o/D varied in the range 0.0125 - 0.083.

2.4 Pressure Measurements

The mean pressure component, being extremely small (of the order of 0.6898 N/m^2) demanded a highly sensitive instrumentation for its measurement. This was accomplished

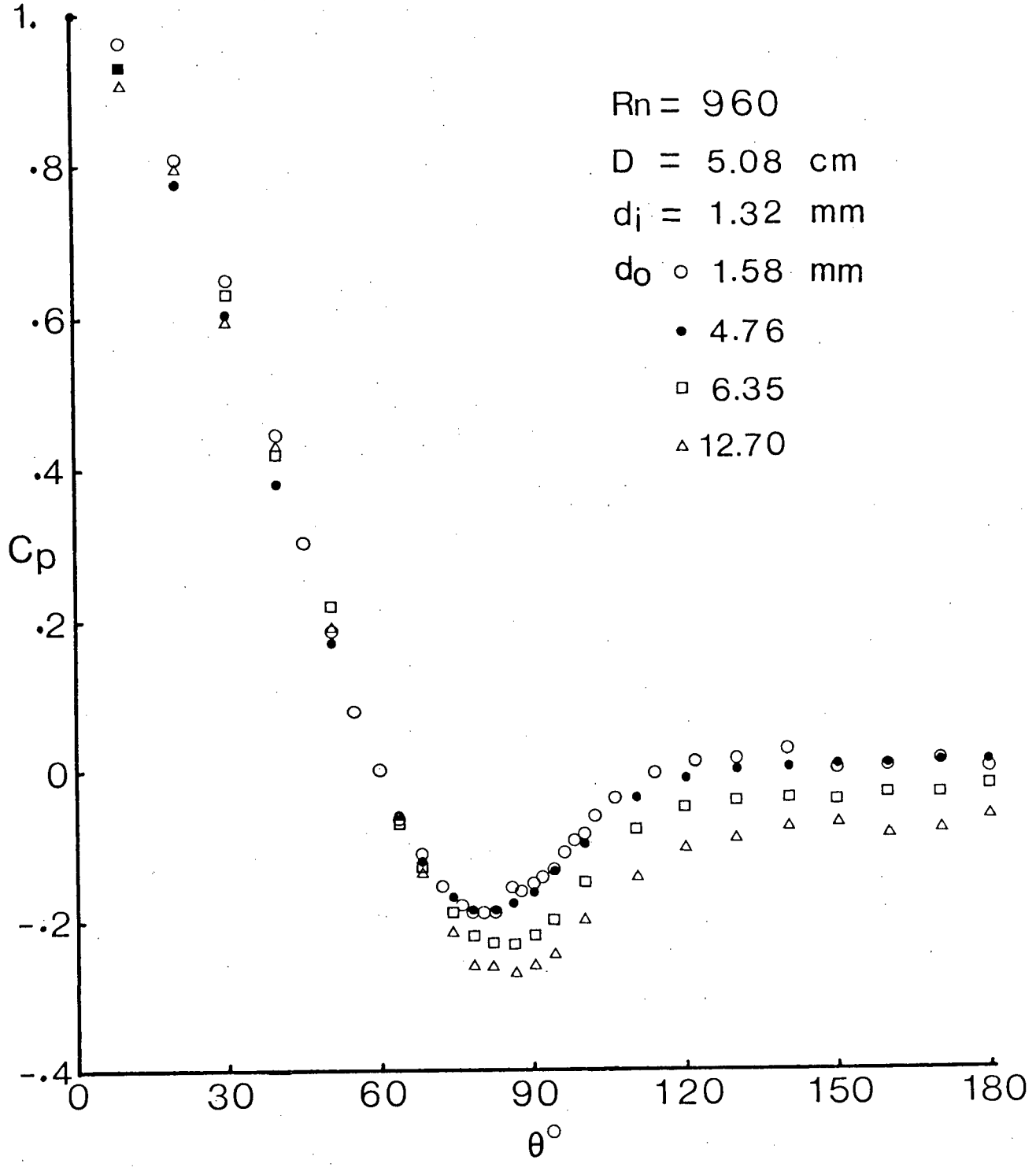

Figure 2-11 Effect of the stem diameter on measured surface pressure distribution over a sphere:
(a) Sphere diameter = 5.08 cm

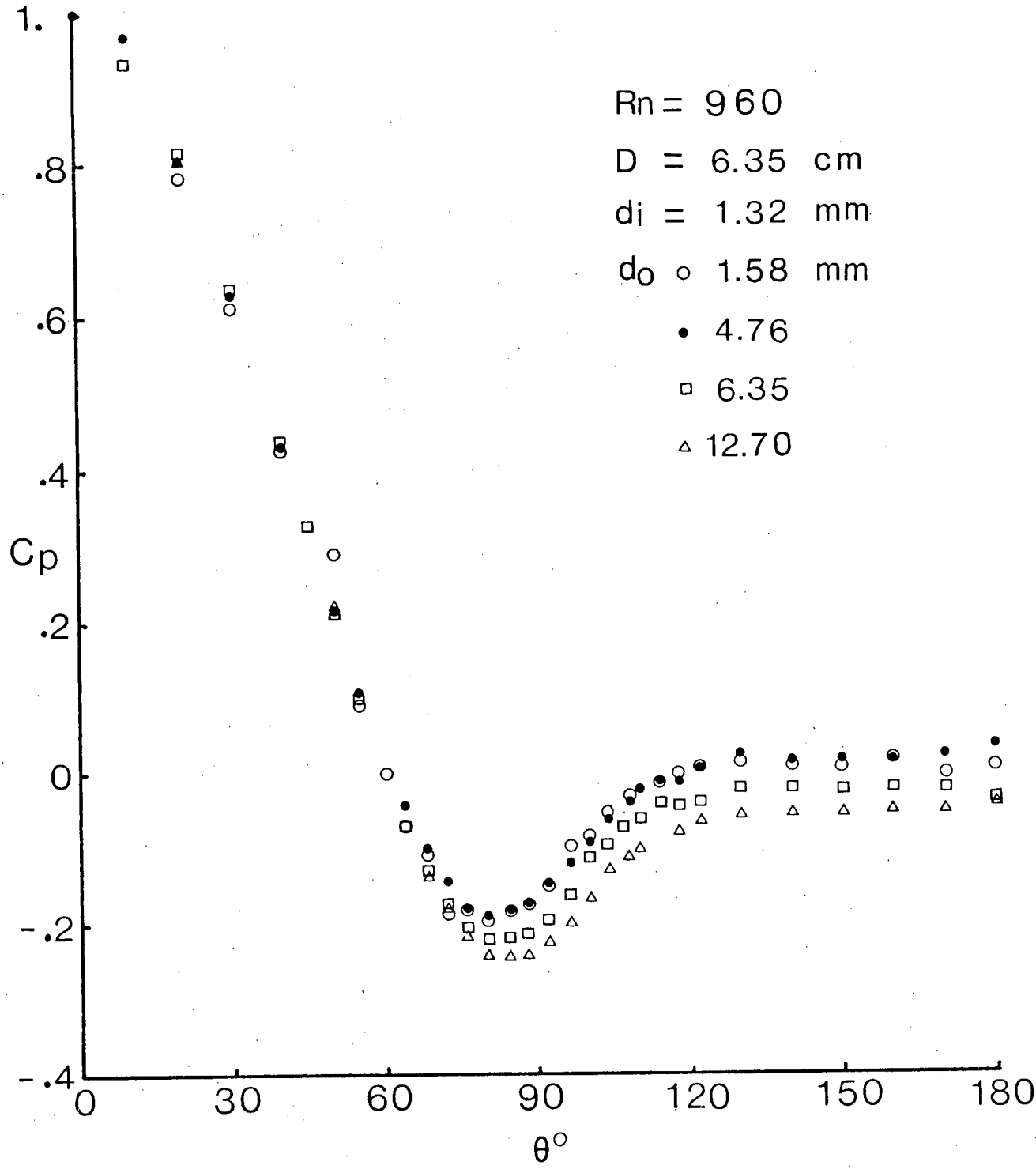

Figure 2-11 Effect of the stem diameter on measured surface pressure distribution over a sphere:
(b) Sphere diameter = 6.35 cm

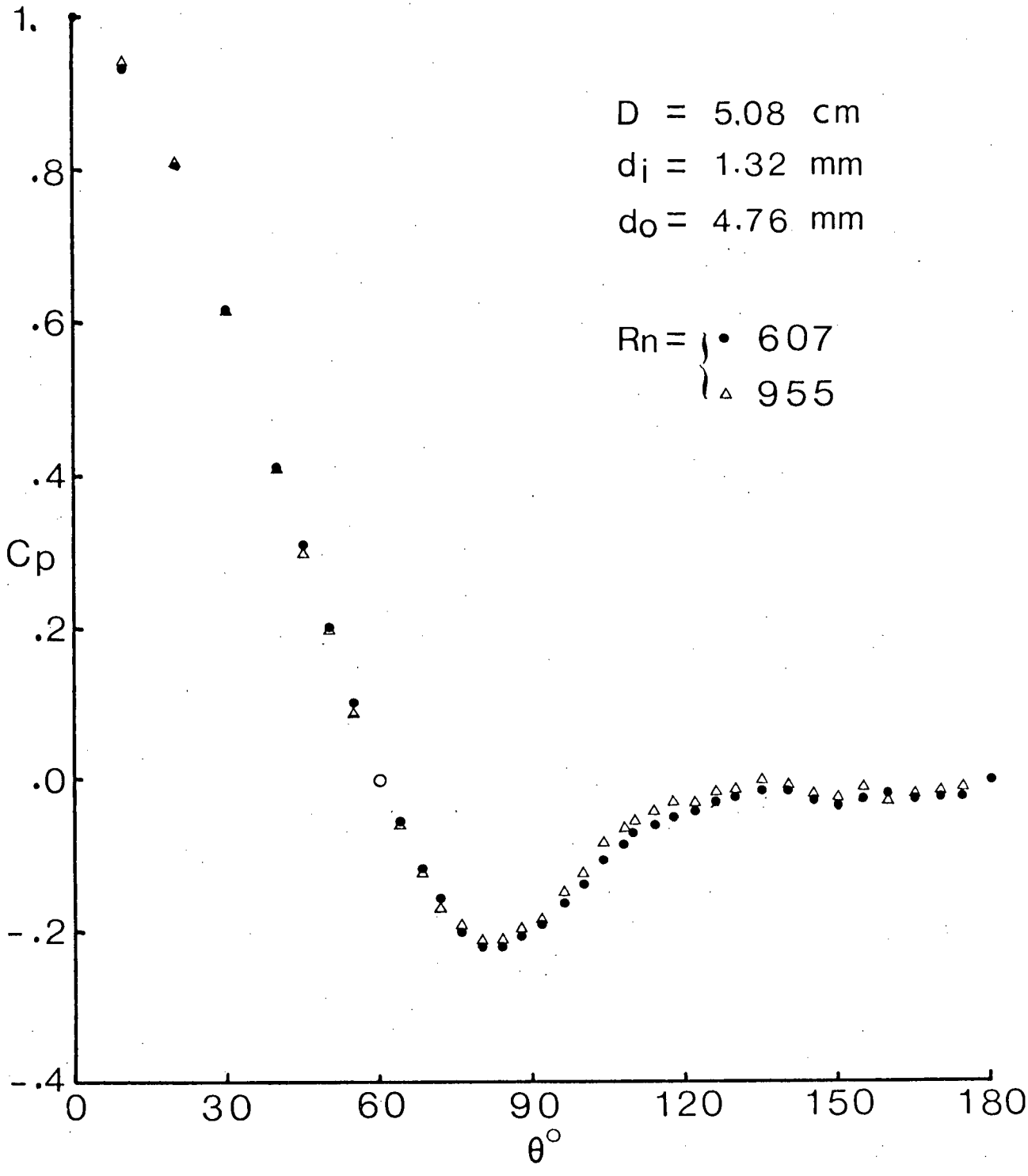

Figure 2-12 Plots showing stem-effects to be relatively independent of the Reynolds number in the range 300-1000: (a) D = 5.08 cm, d_i = 1.32 mm, d_o = 4.76 mm

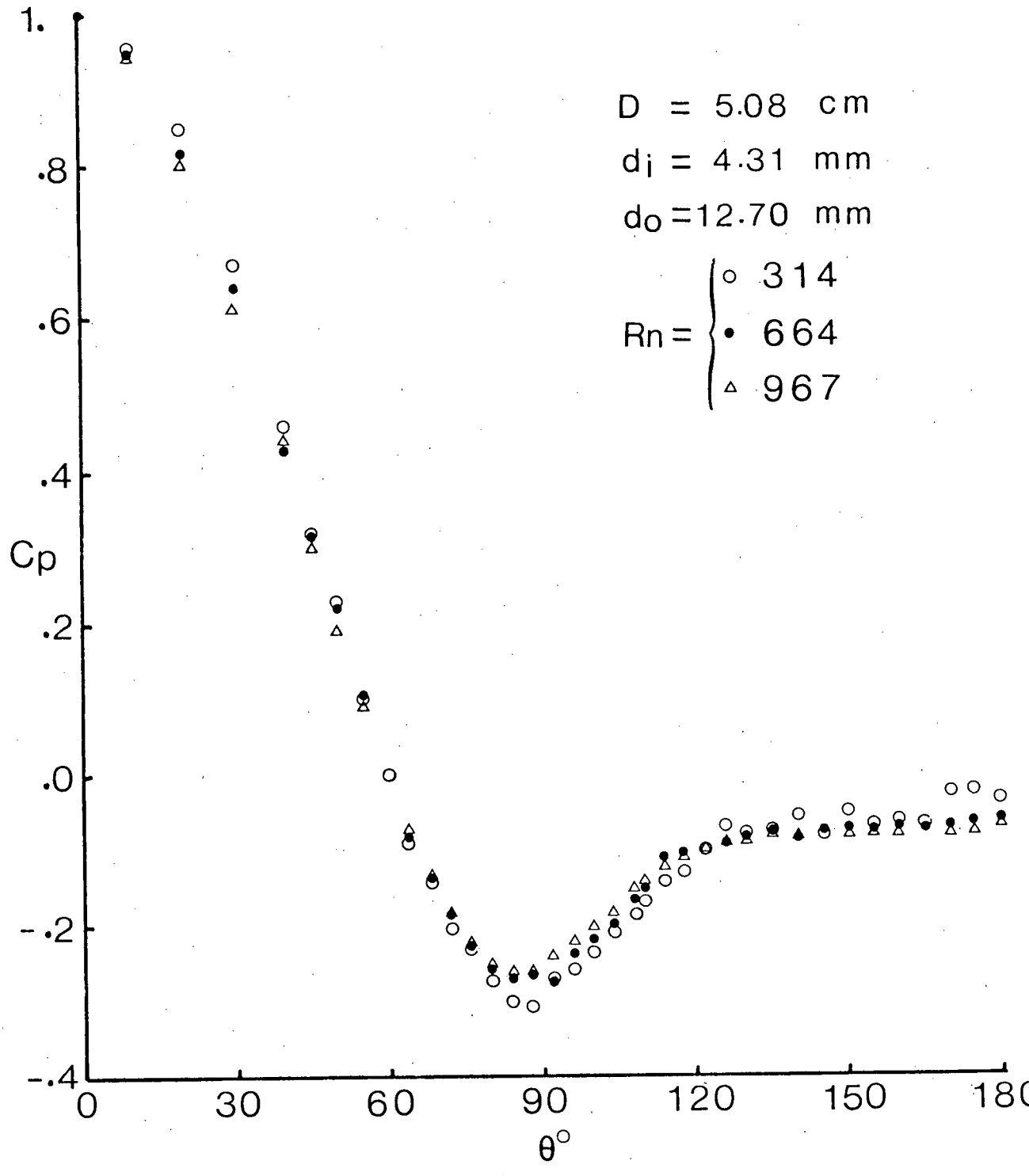

Figure 2-12 Plots showing stem-effects to be relatively independent of the Reynolds number in the range 300-1000: (b) D = 5.08 cm; d_i = 4.31 mm, d_o = 12.70 mm

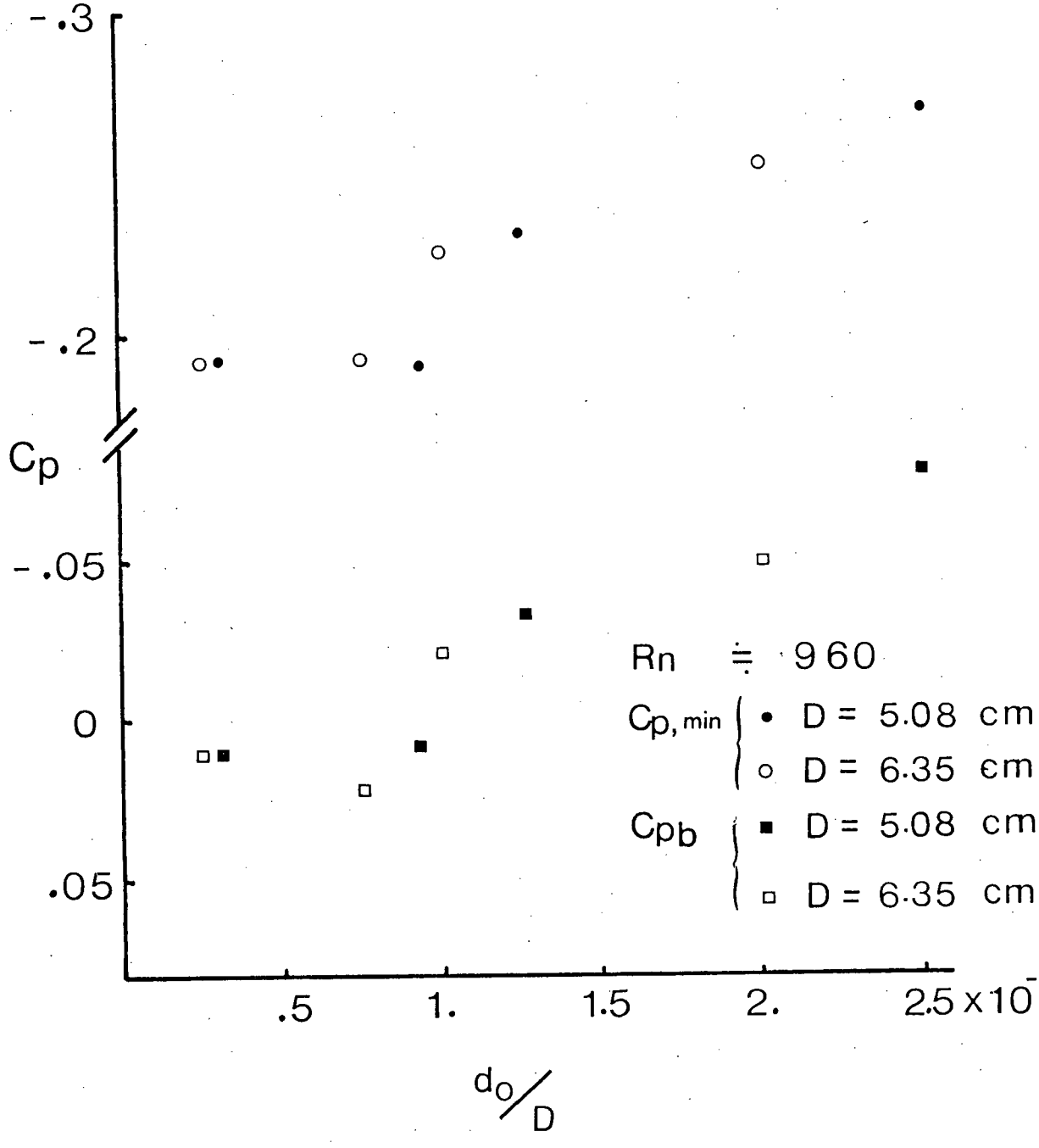

Figure 2-13 Variation of the minimum and base pressures showing the critical value of d_o/D

using a "Barocel Modular Pressure Transducing System" developed by DatametricsInc. of Watertown, Massachusetts. The type 550-5 Barocel sensor is designed to operate with fluids over the pressure range of 0 - 10 psia (68.98 kN/m^2). The unit is a high precision, stable capacitive voltage divider, the variable element of which is a thin prestressed steel diaphragm positioned between fixed capacitor plates. The diaphragm deflects proportionally to the magnitude of the applied pressure. To isolate the external pressure medium from the sensor diaphragm-capacitance system, the unit uses highly sensitive metallic bellows. The volume between the bellows, isolator and sensor diaphragm is filled with degassed silicone oil which serves both as pressure transmitting fluid and as a dielectric. The pressure signal from the external liquid medium is transmitted by the bellows to the silicone oil which in turn deflects the diaphragm to produce the required change in capacitance. An a.c. carrier voltage at 10 Hz is applied to the stationary capacitor plates, and a bridge circuit determines an output voltage dependent on the ratio of the capacitance of the diaphragm to each of the stationary plates. The carrier voltage is therefore modulated according to the input pressure. The unit sensitivity is 10^{-5} psi (0.07 N/m^2) provided the pressure sensor is fully isolated from external sources of vibration and noise. It was imperative to ensure removal of all traces of air

pockets from the pressure ducting for satisfactory operation. Barocel is accurately calibrated for steady pressures. Figure 2-14 presents a schematic diagram of the pressure transducer.

It was important to minimize the effect of ambient temperature excursions on the Barocel's performance. This was achieved by mounting the transducer on a heat sink, a large aluminum block with working fluid circulating inside. The arrangement virtually eliminated the influence of temperature transients.

After a complete removal of air bubbles from the fluid, a model was positioned in the test section with its center 46 cm downstream of the last screen. Next, the pressure ducting was filled with the test fluid and was connected to a Barocel pressure transducer via a set of polyethylene and Mylar tubings after removal of air pockets from the line. The pressure sensing unit was balanced to read zero output in the no-flow condition. With the pump operating at a preselected speed to give a desired Reynolds number and the test fluid held at a constant temperature, the mean pressure distribution around the horizontal meridional cross-section was measured. For each run the velocity profile upstream of the sphere was also recorded. The hot-film probe, mounted on a traversing gear, was positioned 25 cm upstream of the sphere. The procedure was repeated over a range of mean flow rates.

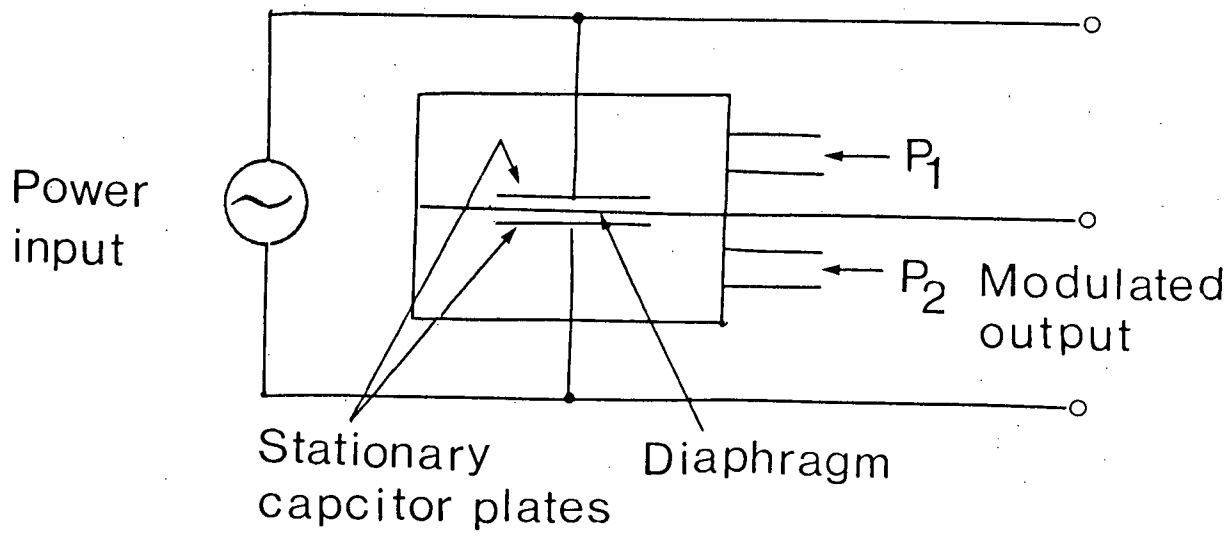

Figure 2-14 A schematic diagram of the Barocel pressure transducer

A point concerning an appropriate choice of the size of the pressure tubings must be emphasized here. A systematic study with tubes of different size and associated time to reach steady state pressure showed the tubes with internal diameter less than 1.6 mm to have an excessively large time constant (> 20 min) . Of course, as suggested by several theoretical and experimental studies on the dynamic response of fluid lines[54-56], the time constant would depend on a number of parameters including the diameter and length of the tubings, viscosity of the fluid, inline volume including the transducer's cavity, character of pressure signals, etc. For the mean pressure measurements under consideration, it was convenient to use fluid lines of 4.6 - 6.4 mm resulting in the time constant (τ) of around 3 - 5 minutes.

To insure accuracy as well as repeatability of the measured data, it was of utmost importance to minimize and compensate for any drift of the pressure transducer and associated electronic circuitry. Minute character of the pressure signals (10^{-4}psi) together with the relatively long time involved in reaching the steady state made this all the more necessary. Chart recordings of the drift over periods of 24 - 48 hours showed them to be quite significant, at times as large as 50% of the actual signal, but of no well defined pattern. The drift compensation procedure involved three successive measurements at equal intervals of

time corresponding to the time constant of the system. This is explained in detail below.

Let the objective be to measure a differential pressure $P_a - P_r$, where P_a represents pressure on the surface of the sphere at point 'a' and P_r corresponds to the pressure at a reference point. Let the arbitrary zero drift of the electronic system be as indicated in Figure 2-15. The diagram also shows the corresponding drift of the differential pressures ΔP_a and ΔP_r, where $\Delta P_a = P_a - P_w$ and $\Delta P_r = P_r - P_w$. Here P_w represents pressure at a suitable location, taken to be on the tunnel wall in the present case. Thus, the desired $P_a - P_r = \Delta P_a - \Delta P_r$.

Now, from Figure 2-15,

$$(\Delta P_r)_1 = \Delta P_r + \delta_1 ,$$

$$(\Delta P_r)_3 = \Delta P_r + \delta_1 + \delta_2 + \delta_3 ,$$

$$(\Delta P_a)_2 = \Delta P_a + \delta_1 + \delta_2 ;$$

$$\therefore \quad \frac{(\Delta P_r)_1 + (\Delta P_r)_3}{2} = \frac{(\Delta P_r + \delta_1) + (\Delta P_r + \delta_1 + \delta_2 + \delta_3)}{2}$$

$$= \Delta P_r + \delta_1 + \frac{\delta_2 + \delta_3}{2} .$$

Hence,

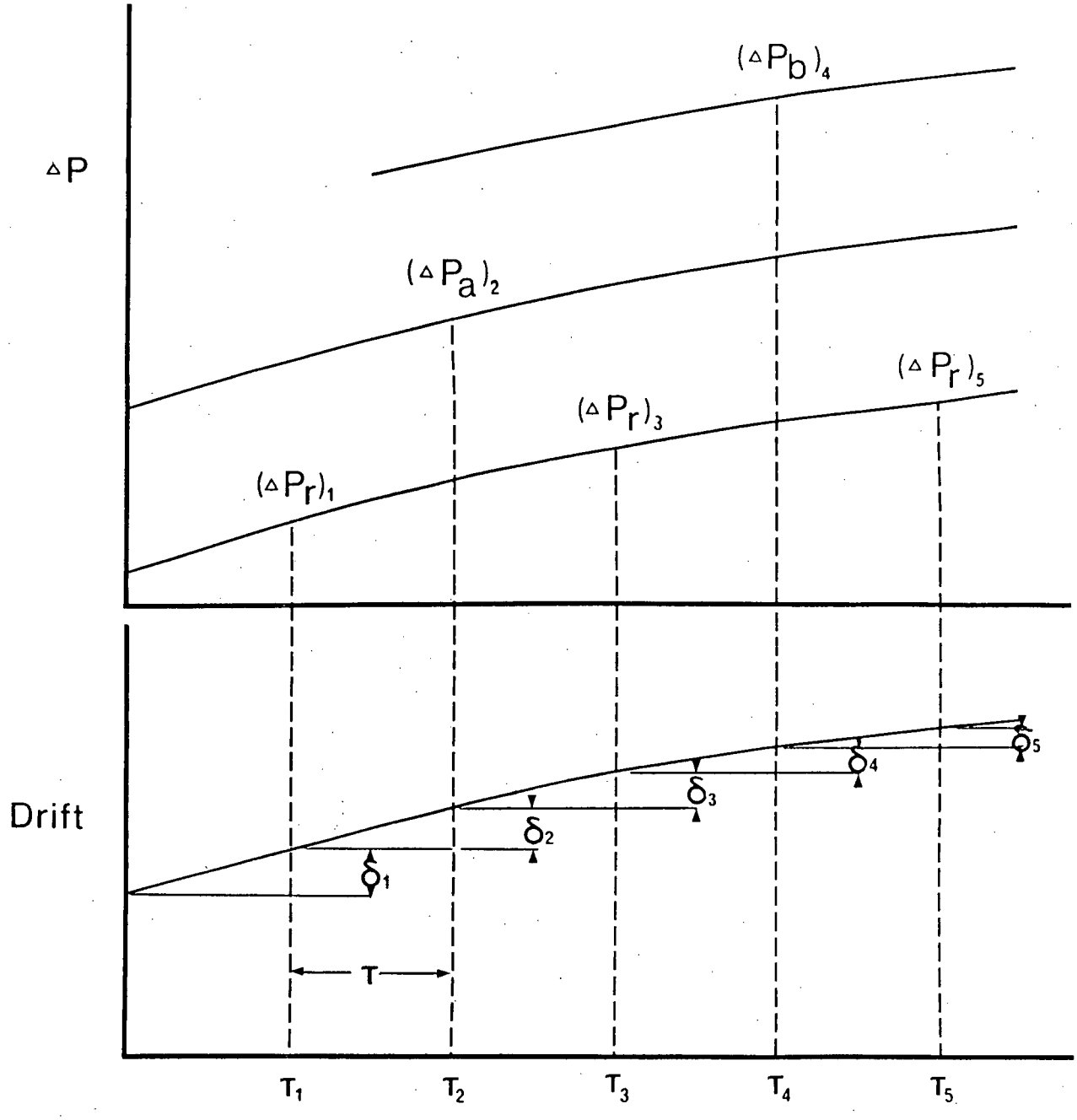

Figure 2-15 A procedure for compensation of the electronic drift of the pressure measuring system

$$(\Delta P_a)_2 - \frac{(\Delta P_r)_1 + (\Delta P_r)_3}{2} = (\Delta P_a)_1 - \Delta P_r - \delta_1 - \frac{\delta_2 + \delta_3}{2}$$

$$= P_a - P_r + \frac{\delta_2 - \delta_3}{2} \quad .$$

Assuming that the electronic zero setting drifts linearly during the interval marked by the pressure measurements $(\Delta P_r)_1$, $(\Delta P_r)_2$ then

$$\delta_2 - \delta_3 = 0 \quad ,$$

i.e.,

$$(\Delta P_a)_2 - \frac{(\Delta P_r)_1 + (\Delta P_r)_3}{2} = P_a - P_r \quad . \ldots\ldots (1)$$

Thus determination of the differential pressure involved the measurement of $(\Delta P_r)_1$, $(\Delta P_a)_2$ and $(\Delta P_r)_3$ in that order. The procedure gave data that can be reproduced within an accuracy of ±2%. Note, the evaluation of the differential pressure $P_b - P_r$ at some different location on the sphere would follow the same procedure. Thus

$$P_b - P_r = (\Delta P_b)_4 - \frac{(\Delta P_r)_3 + (\Delta P_r)_5}{2} \quad .$$

A question may arise: why not measure the differential pressure $P_a - P_r$ directly. As shown in Appendix I, although this can be done, it involves necessarily more measurements. Furthermore, the resulting formula is more involved and lacks recursion character leading to a substantial increase in time and effort.

Furthermore, any fluctuation in the line voltage would be reflected on the pump speed and hence on the pressure signals from the model. The speed fluctuations were monitored through variations in the orifice meter data. The output voltage from the pressure transducer was damped using a DISA type 550 digital d.c. voltmeter equipped with a r-c damping circuit to provide an adjustable time constant of up to 100 seconds. A schematic diagram of the instrumentation layout is shown in Figure 2-16.

The tests were conducted on a family of spheres, ranging in diameter from 3.8 - 12.7 cm, in the Reynolds number range of 280 - 2200. In all the cases, the model was supported by a vertical stem, a stainless steel tubing, which also served as a pressure conducting line. Its outside diameter was dictated by the relative size of the sphere and the stem influence on the pressure field. On the other hand, the inside diameter was governed by the time constant to reach the steady state pressure as discussed before. The stem adopted for the experiments had an inside diameter of 1.32 mm

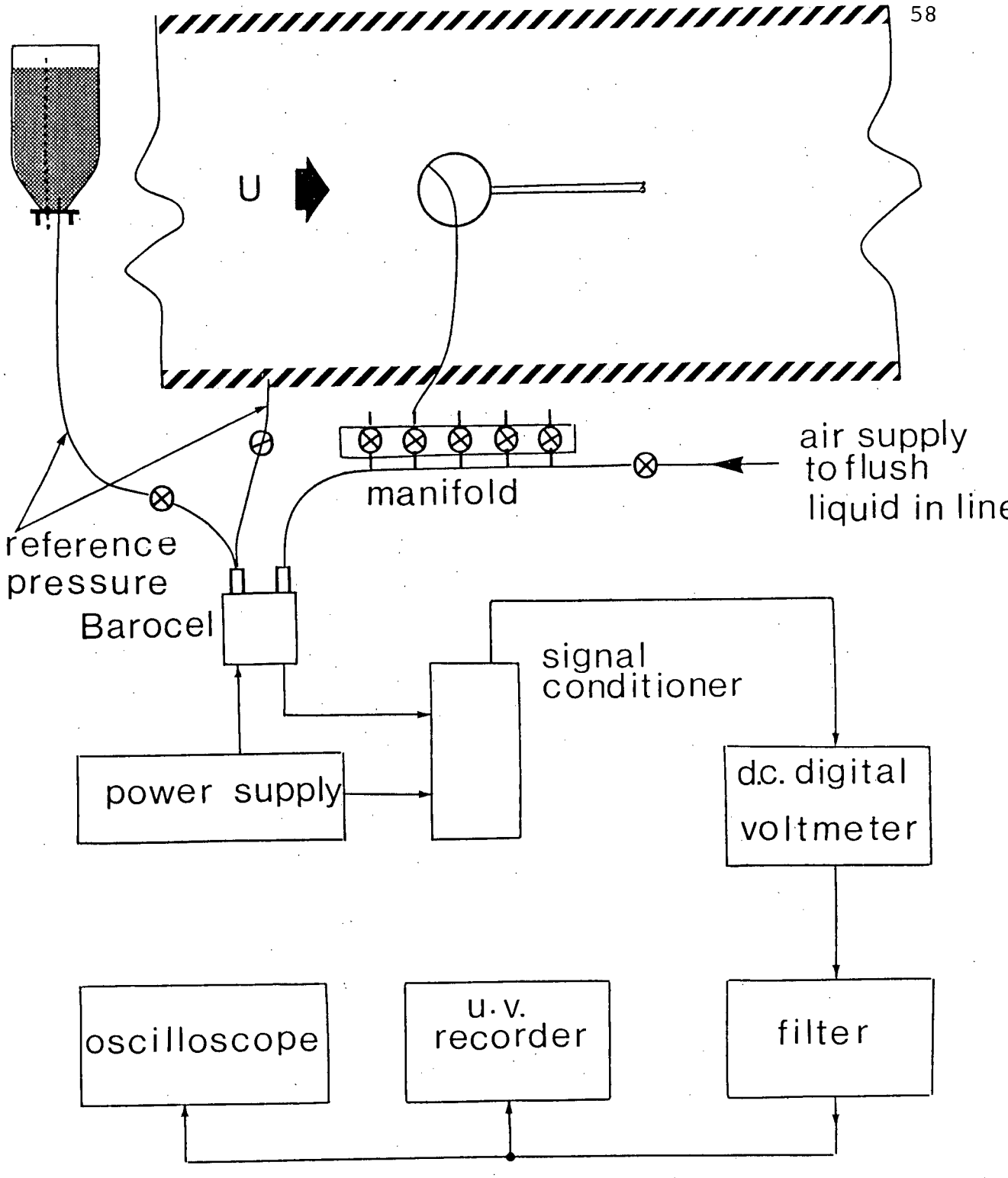

Figure 2-16 A line drawing of the instrumentation set-up used for pressure measurements

and an outside diameter of 1.83 mm resulting in D/d_o in the range of 22.8 - 66.6.

The pressure measurements were confined to the horizontal meridional section of the model. A 1/16 in. pressure tap connected the stem through a groove (1/16 in.dia.) drilled in the body of the sphere (Figure 2-17). The entire horizontal plane was covered by a controlled rotation of the stem in a step size that varied between 4° to 10° depending upon the gradient of the pressure profile. The measurements in general were confined to only one side of the sphere, except for occasional checks to confirm flow symmetry.

2.5 Drag Measurements

The balance used for drag measurements essentially consists of three components:

(i) removable stem supporting the spherical model;
(ii) central suspension block supported by a pair of needle bearings;
(iii) interchangeable cantilever type sensing unit with strain gages affixed near its root.

The stem supporting the model is attached to the central block by a thread and nut arrangement, which proved to be quite convenient in changing the models without affecting the rest of the balance. Interchangeable character of

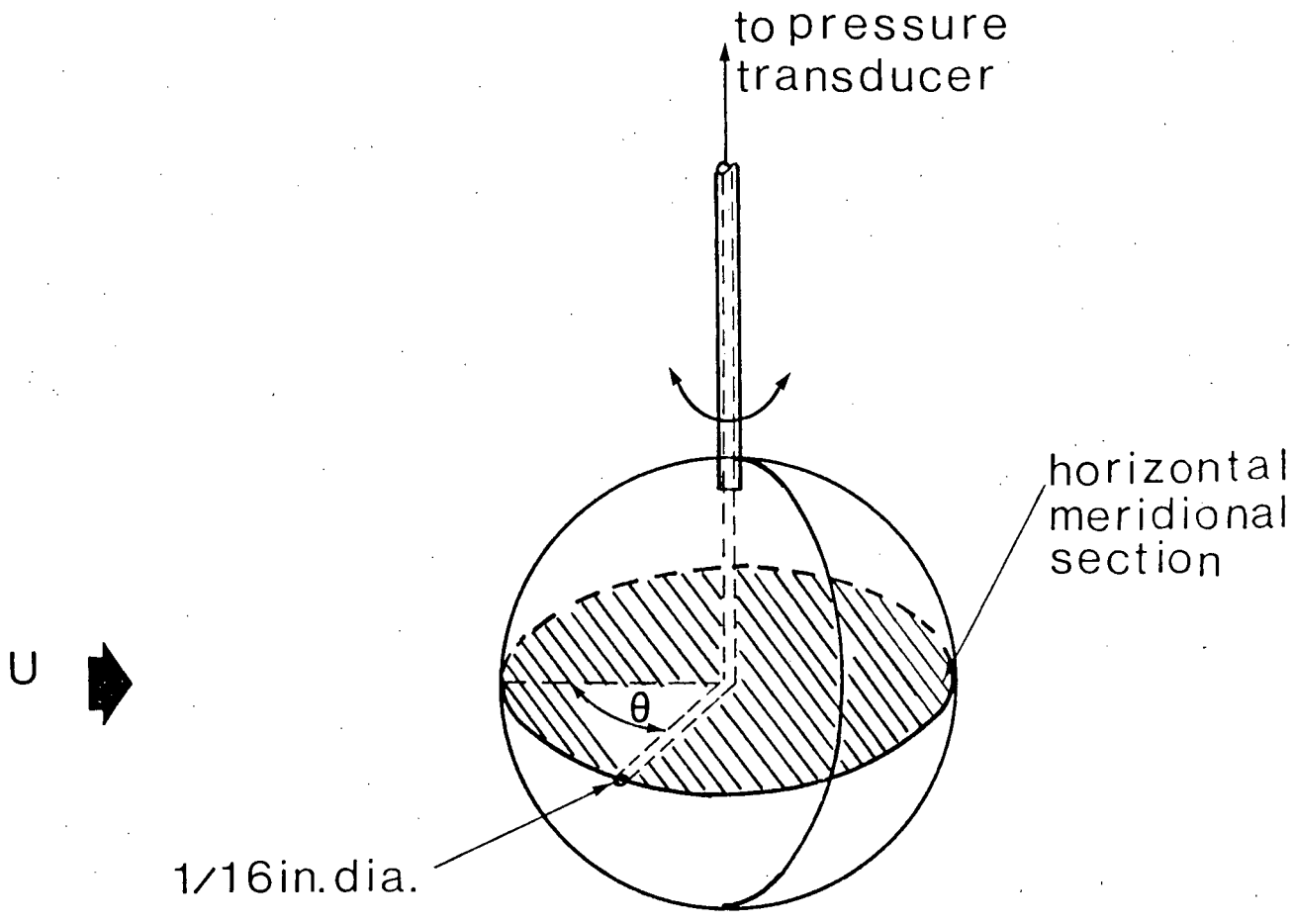

Figure 2-17 A schematic diagram showing the spherical model and its support system during pressure measurements

the sensing element was purposely introduced to achieve a desired degree of accuracy in a given range of drag. Several beams of varying flexural rigidity and length were constructed for measurement of drag in the range of 0.1 - 15 grams with the sensitivity of 10^{-3} gram. Further improvement in sensitivity can also be attained by adjusting the gain of a bridge amplifier meter. Two strain gages, one on each side of the beam, were used for temperature compensation. The tip of the beam rested against a fixed wedge shaped support. Alignment of the stem with the local vertical being critical for elimination of any contribution of the model weight to the drag, the wedge support was mounted on a micrometer with positional accuracy of 0.025 mm (0.001 in).

Sensitive character of the beam demanded that calibration of the balance be carried out under actual test arrangement with a spherical model located in the tunnel. This is particularly important to effectively compensate for any contribution from the weight of the sphere due to deviation of the supporting stem from vertical. This can arise in spite of the initial alignment assured by the wedge because of the flexibility of the stem, no matter how small it may be. The arrangement is schematically shown in Figure 2-18 while Figure 2-19 shows the actual assembled unit.

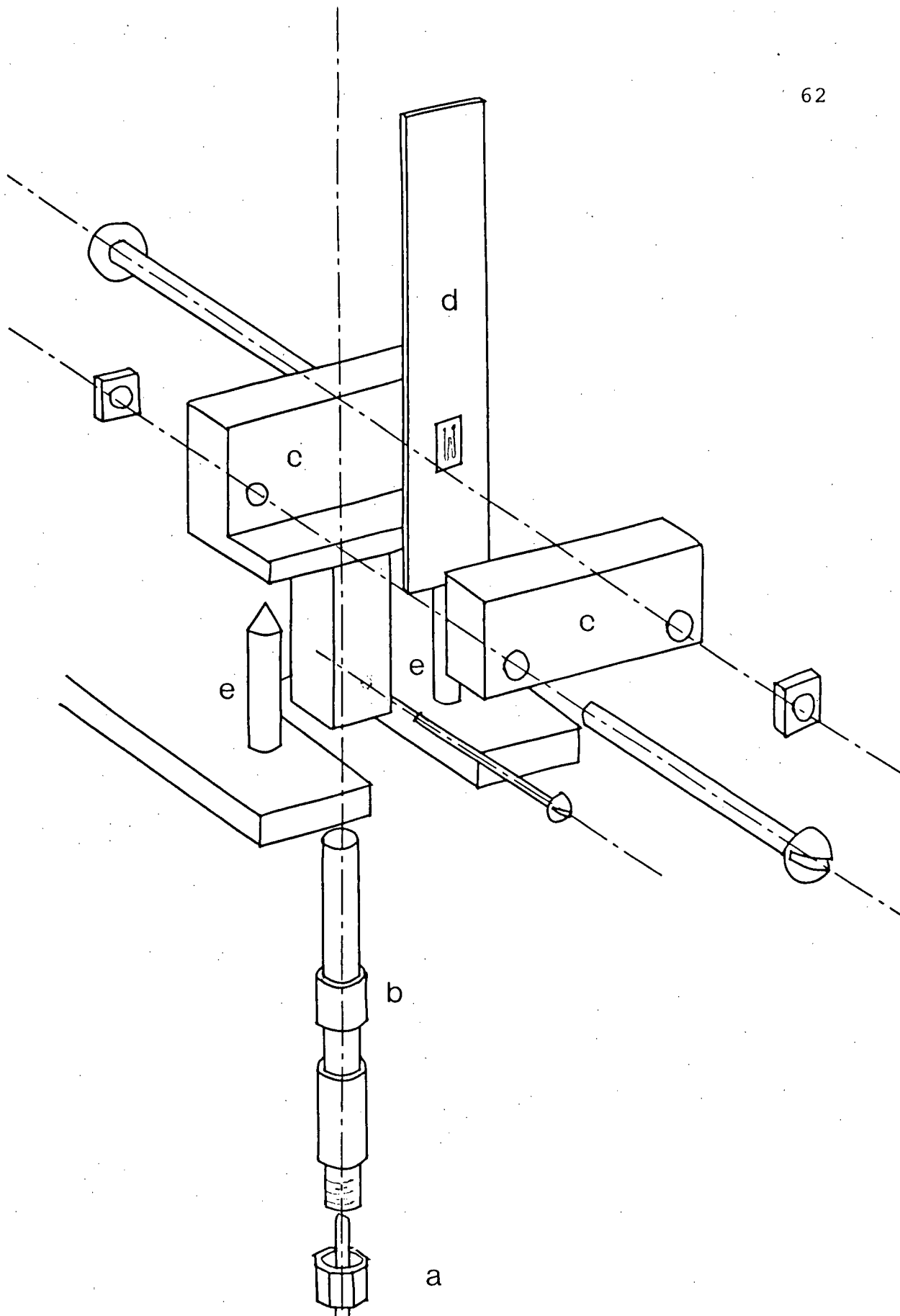

Figure 2-18 An exploded view of the drag measuring balance: (a) supporting stem; (b) intermediate connection; (c) central suspension block; (d) cantilever with strain gages; (e) needle bearings supporting the central block

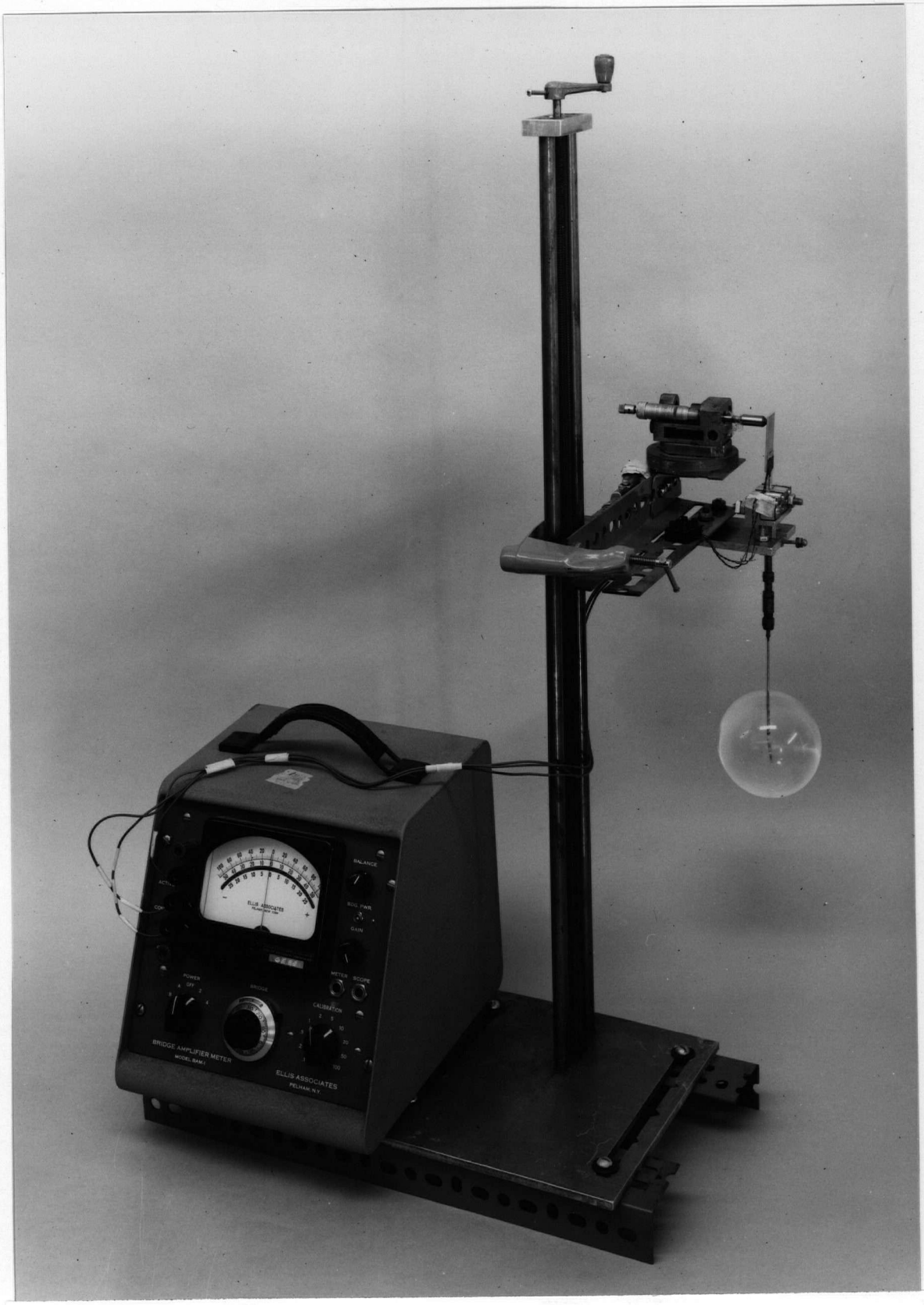

Figure 2-19 (a) Drag balance assembly with bridge amplifier meter

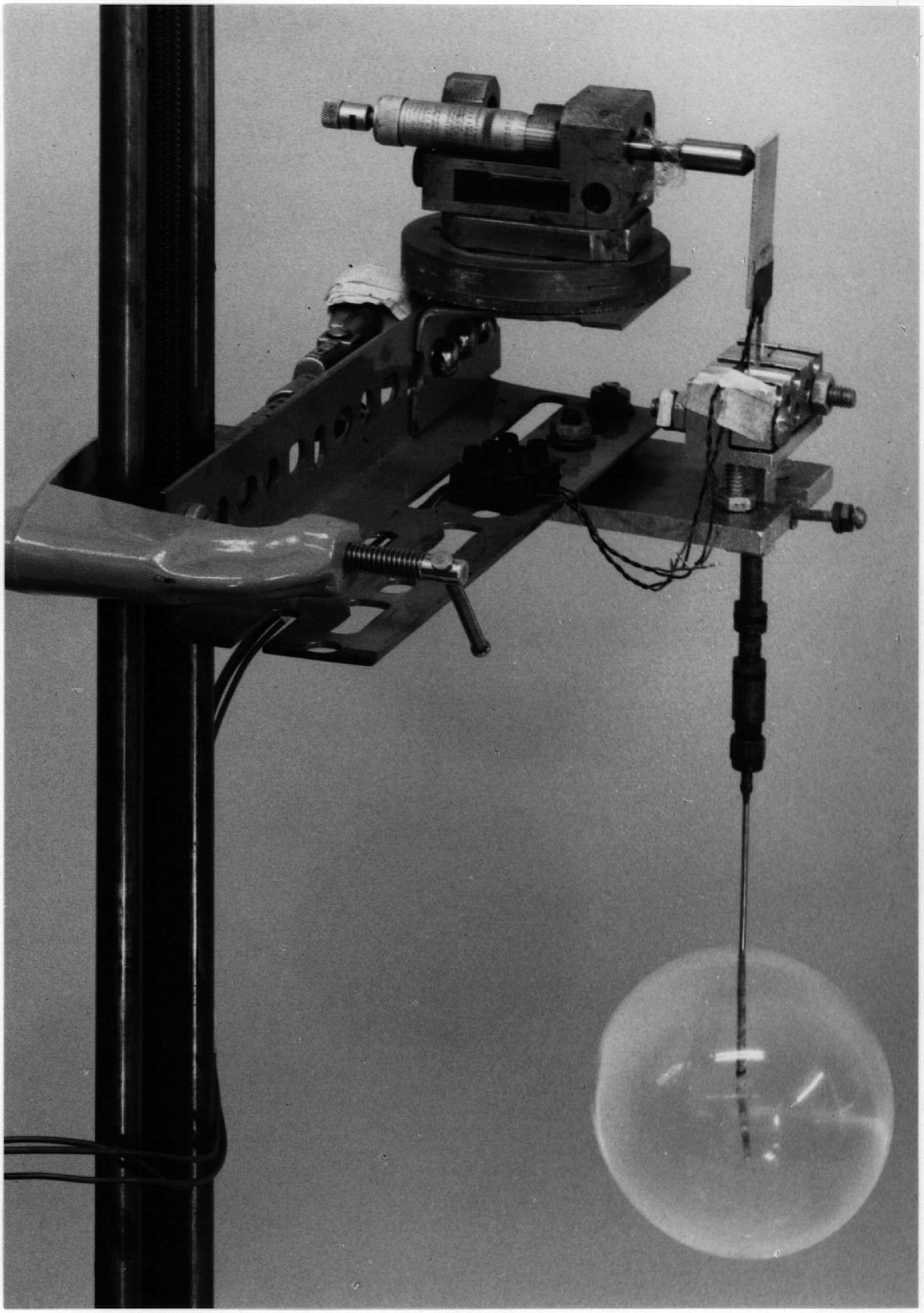

Figure 2-19 (b) Close-up view of the drag balance

2.6 Flow Visualization

To better appreciate the physical character of the fluid field associated with spherical models under confined condition, flow visualization was undertaken. The dyed glycerol-water solution of the same concentration as that of the test fluid was injected approximately 10 cm upstream of the model. The dye employed was an imitation cochineal food colour. Appropriate volumes of the dye and pure glycerin were mixed to produce a glycerol-water solution of the same density as that of the test fluid. A dye injecting probe consisting of seven #23 syringe needles (0.38 mm) placed 0.5 - 1.0 cm apart on a streamlined support, was constructed (Figure 2-20). "Intramedic" tubings (0.6 mm inside diameter) were used to connect the needles to a manifold. The rate of injection was controlled with brass needle valves. To ensure adequate flow through each needle, i.e., to provide sufficient head, the supply bottle was suspended from the ceiling 4 m above the injection level. A schematic diagram of the complete set-up is shown in Figure 2-21.

At times, particularly while studying the near wake geometry, it was convenient to inject dye directly through the pressure tap located on the surface of a sphere via the supporting stem. It was now possible to introduce dye at any desired location on the sphere. The procedure proved quite effective in identifying separation position of the ring vortex.

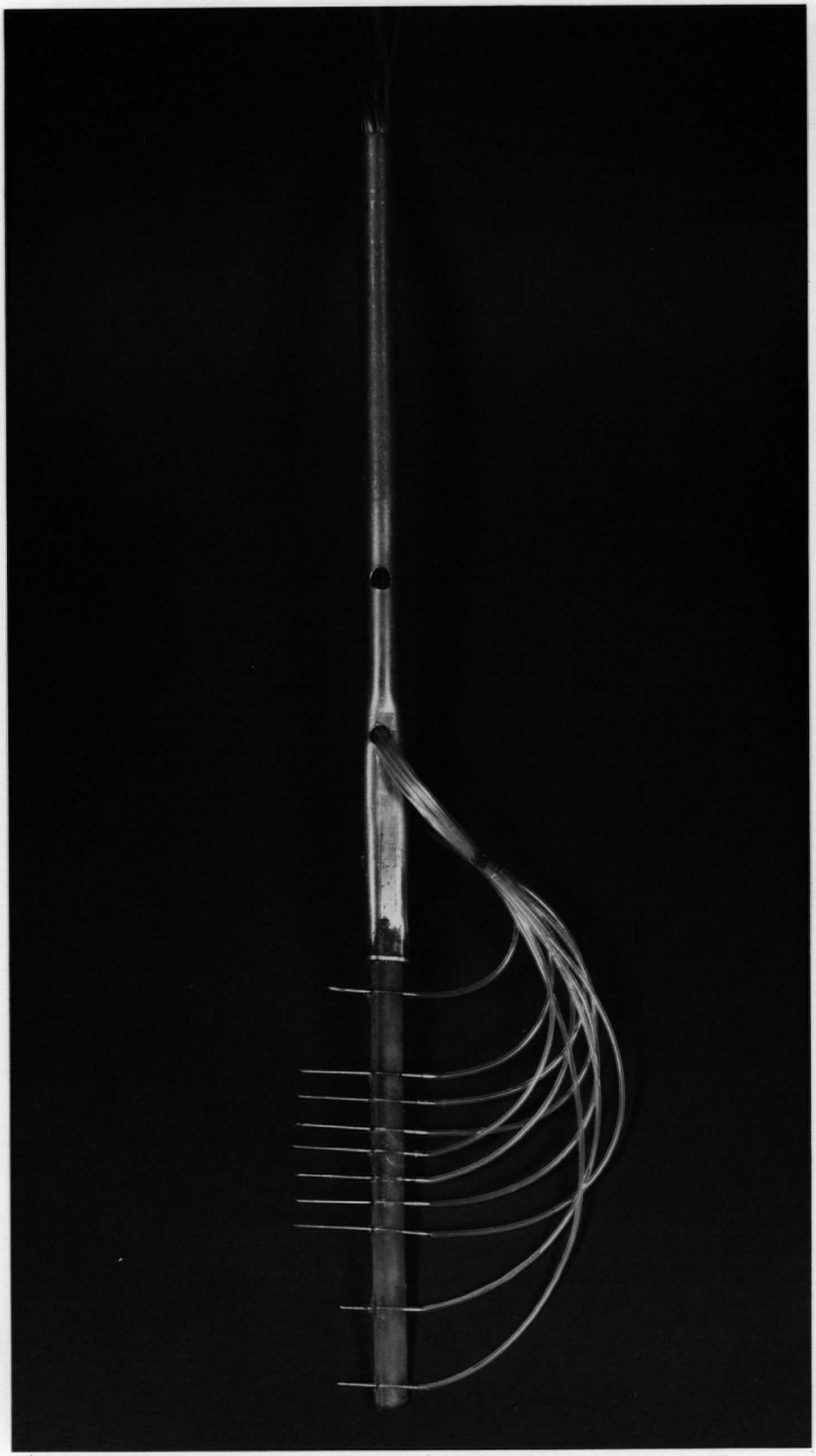

Figure 2-20 Dye injecting probe used during flow visualization

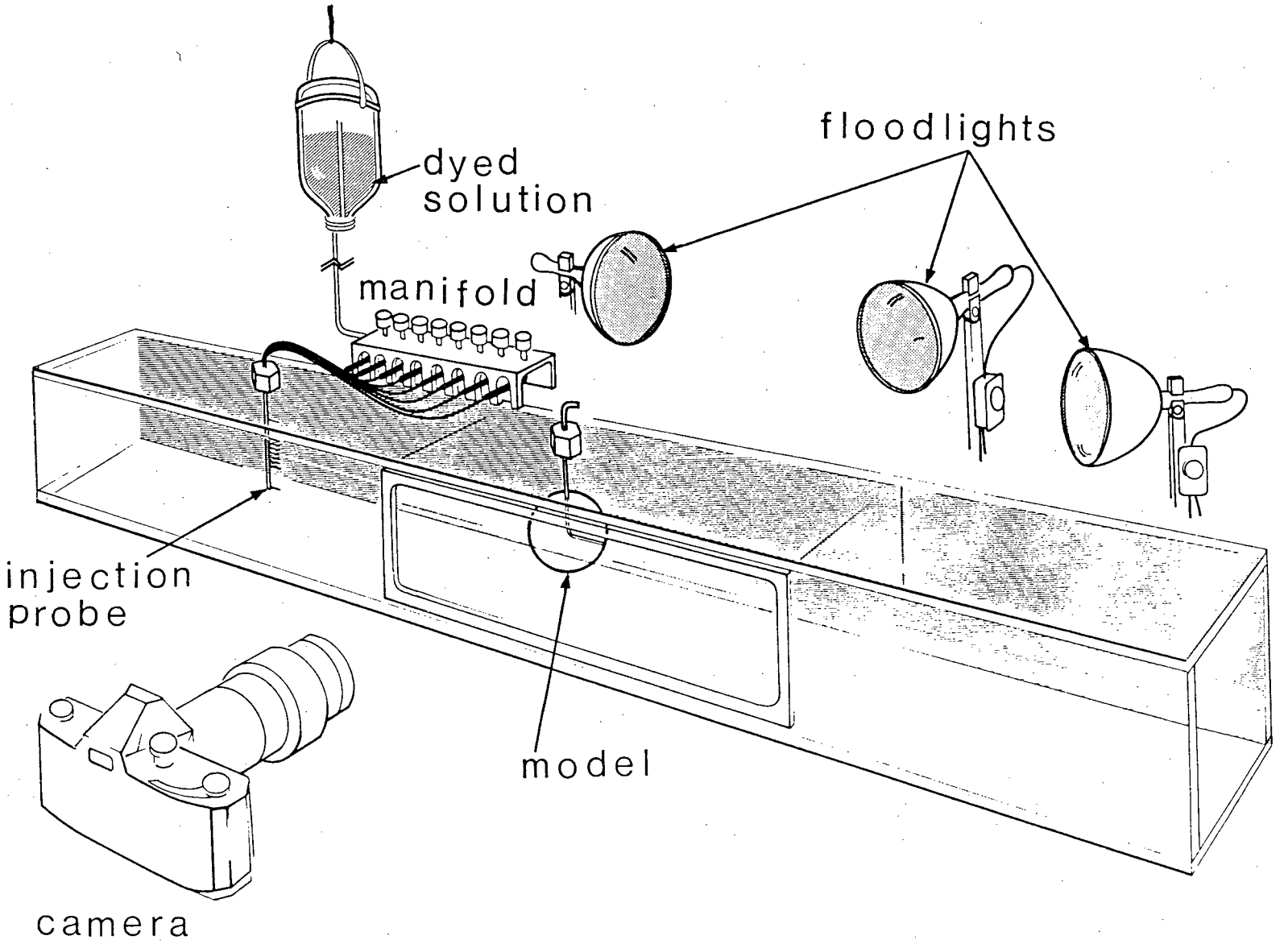

Figure 2-21 A sketch showing the equipment layout during flow visualization

It would be appropriate to point out here the type of lighting system used as it played a critical role in the photographing process. A combination of three variable intensity photo floods (maximum 500 watts, 3400°K) back-illuminated the subject through the tunnel glass window. To eliminate hot spots, the light beam was evenly diffused by masking the test section wall with a tracing paper. A set of trial runs helped arrive at the appropriate aperture setting and exposure time for the type of film used (Kodak high speed Ektachrome type EHB-135(still) or EF-7242(movie), tungsten, 3200°K, ASA 125, filter 81A).

During the course of visualization study, it was discovered that in spite of the large volume of the test fluid (40 U.S. gallons), a relatively small amount of dye (8 fluid oz) was sufficient to pollute the working fluid to the point that no clear photographs could be taken. This presented a rather serious problem in terms of time, effort and cost involved in replenishing the working fluid. Clearly, it was necessary to find an agent that would neutralize the dye without attacking the tunnel material or its circulating system and which does not alter the physical properties of the test fluid. Unfortunately, no such agent has been reported in the literature. A considerable amount of patient testing with numerous oxidizing agents led to sodium hypochlorite which has all the desirable attributes. Only 300 cc of the agent was

sufficient to completely neutralize the dye. To keep the concentration of the test fluid constant, sufficient amount of glycerin was periodically added thus offsetting the diluting effect of the dye removing agent.

3. RESULTS AND DISCUSSION

With some appreciation of background to the problem, instrumentation used and the experimental procedures adopted, we are ready to look into the test results and their interpretation. The amount of experimental data obtained is rather enormous, thus dictating a compromise in presentation between conciseness and comprehensibility. The guiding principle has been to include only those results which have immediate relevance to the study in hand, and help in establishing definite trends. In general, the sequence in which the results are presented also denote the chronological order of the tests. To begin with, an approach to data reduction, so critical at low Reynolds number, is discussed. This is followed by presentation of the surface pressure distribution results as affected by Reynolds number and blockage. Next, measured sphere drag values are analyzed as functions of system parameters and compared with integrated pressure drag to establish skin friction contribution. Finally, near-wake structure is studied using flow visualization in conjunction with still and 16 mm movie photography. Available results from literature are included when appropriate for comparison and to assist in emphasizing the influence of blockage.

3.1 Choice of Reference Velocity and Pressure

Before proceeding with presentation and analysis of the test results, one must address to several fundamental questions which are particularly significant in the low Reynolds number flow studies. Clearly, with a model immersed in an unbounded uniform stream there is no ambiguity concerning reference or characteristic velocity and pressure: It is the constant velocity and pressure of the stream far away from the model. For low Reynolds number flow in a tunnel, however, the fluid velocity and pressure vary significantly along the axis of the test section, even in absence of the model due to boundary layer growth along the walls. Presence of the model and associated wake would only accentuate the problem. Obviously some compromise is indicated in selection of these parameters.

Grove et al.[57,58] have suggested use of the pressure directly below the centerline of their model as the reference static pressure and the centerline velocity, with the model absent but at the same setting of the pump, as the characteristic velocity. For models with a small blockage this choice of reference pressure may prove to be adequate but with a larger blockage, due to acceleration of the flow at the model location, the

reference pressure is indeed affected and becomes a function of wall confinement (besides other parameters). To put it differently, the choice of reference pressure as suggested above has a degree of optimism implicit in it. It assumes that effects of the upstream adverse pressure gradient created by presence of the model exactly cancels the influence of acceleration in gaps at the model location thus giving the desired P_∞.

One possible improvement in the choice of P_∞ would be to take it as the pressure at the model location (but without the model) with operating condition of the tunnel kept the same as that used with the model in position. However, this still cannot account for the changes in velocity profile from section to section in a given tunnel, and between tunnels used by different investigators.

Usefulness of the centerline velocity as a characteristic velocity also poses several questions. In general, the velocity profiles are substantially affected by location, boundary layer growth, screen's mesh size, blockage, pump speed and the total circuit resistance. Hence the characteristic velocity U_c proposed by Grove et al. can hardly be considered a suitable reference.

Another possible compromise would be to take uniform portion of the velocity profile far upstream and use it as a characteristic velocity. However, the

distance involved to account for boundary layer effects would, in general, depend upon the tunnel used, model and its location.

A rather significant point to keep in mind in presenting data is to ensure its repeatability by other investigators, using different test facilities, to permit comparison. With this in mind and after careful consideration of the alternative methods discussed above a compromise characteristic velocity, average velocity in the test section based on the mean flow rate (U), was adopted. This approach has several obvious advantages. It eliminates most of the problems mentioned above.

Obviously, tests conducted with and without model (but at the same meter setting as with the model) would leave the average velocity in the test-section unchanged. Thus, not only does it eliminate the question of model location, type of tunnel, flow straighteners used and size of the test section but also overcomes problems of pressure gradient and blockage. The choice would facilitate duplication of R_n, reference velocity being more precisely defined. Furthermore, its measurement is quite simple and involves only conventional instrumentation. However, it must be emphasized that this does not correct for changes in velocity profile with distance and hence the resulting pressure effects due to location of the model.

This brings us to that elusive task of selecting P_∞. As discussed earlier, the P_∞ advocated by Grove et al. has little meaning here in view of the large blockage presented by the model. From the point of view of repeatability and comparison of data, the use of pressure at a specified tap on the surface of the model as reference appears quite attractive. Although this cannot account for local variations due to blockage effects (from point to point at the surface of the model), it could effectively compensate for it in an average fashion.

Thus one way to present pressure data in coefficient form would be as $\hat{C}_p = (P_\theta - P_r)/(\rho U^2/2)$ where P_r corresponds to the pressure at a specified tap on the surface of the poppet and U as calculated from the average flow rate (average flow rate/test-section area of 20.32 cm x 20.32 cm). However, this definition is still susceptible to errors introduced by non-uniformity of the velocity profile (at a pressure tap and the reference location) particularly because the denominator remains unaffected by this change. One way to virtually eliminate this shortcoming is to express pressure coefficient as explained below (Figure 3-1).

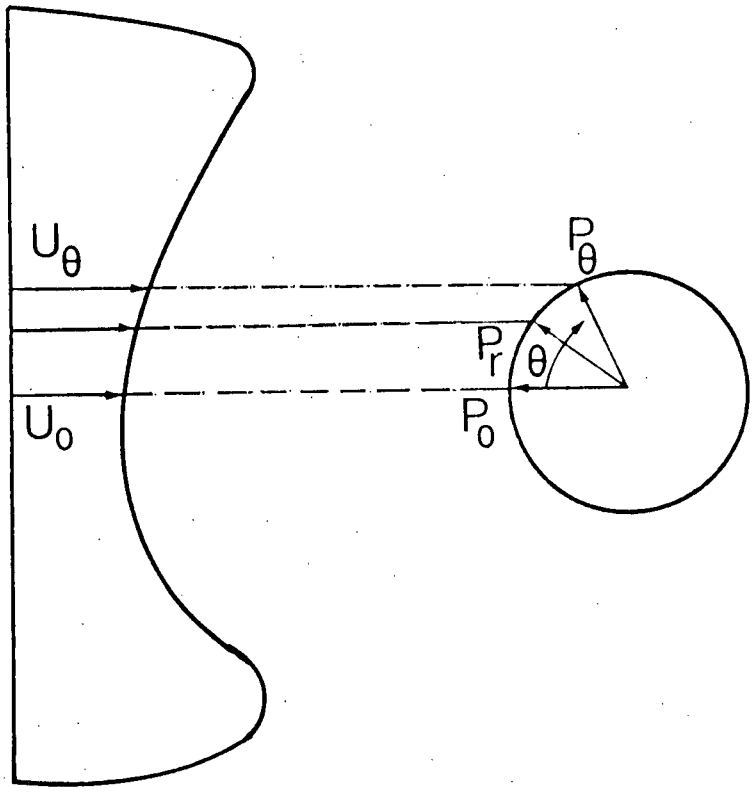

Figure 3-1 An illustration showing possible errors introduced by non-uniformity of the velocity profile

Let errors in pressure due to non-uniformity of the velocity profile be ε_0 at P_0, ε_θ at P_θ and ε_r at P_r. Expressing pressure coefficient as the ratio of the differential pressures, between that at a tap in question and the stagnation point with respect to the reference pressure, gives

$$C_p = \frac{(P_\theta + \varepsilon_\theta) - (P_r + \varepsilon_r)}{(P_0 + \varepsilon_0) - (P_r + \varepsilon_r)}$$

where P_θ, P_r, P_0 correspond to pressures with uniform velocity profile. Thus

$$C_p = \left(\frac{P_\theta - P_r}{P_0 - P_r}\right) \left\{ \frac{1 + (\varepsilon_\theta - \varepsilon_r)/(P_\theta - P_r)}{1 + (\varepsilon_0 - \varepsilon_r)/(P_0 - P_r)} \right\}$$

Note that $\varepsilon_\theta - \varepsilon_r$ and $\varepsilon_0 - \varepsilon_r$ are likely to be very small. On the other hand, $P_\theta - P_r$ and $P_0 - P_r$ represent relatively large quantities compared to the respective error differentials. Therefore,

$$\varepsilon_{\theta r} = \frac{\varepsilon_\theta - \varepsilon_r}{P_0 - P_r} \quad \text{and} \quad \varepsilon_{0r} = \frac{\varepsilon_0 - \varepsilon_r}{P_0 - P_r}$$

are likely to be vanishingly small. Consequently, the term

$$\frac{1 + \varepsilon_{\theta r}}{1 + \varepsilon_{0r}} \simeq 1 \quad \text{and} \quad C_p \simeq \frac{P_\theta - P_r}{P_0 - P_r} \ .$$

Both numerator and denominator being sensitive, the proposed definition of the pressure coefficient promises to provide adequate compensation for errors introduced by non-uniformity of the velocity profile.

The reference location was taken to be at $\theta = 60°$. The choice was prompted by the test data which showed C_p

to reach zero in the general vicinity of $\theta = 60°$, i.e., $P_{60°} \simeq P_{\infty}$ (Figure 3-2). Of course, in general, location of the reference pressure is entirely arbitrary. The pressure data presented in this chapter use the definition of pressure coefficient as

$$C_p = \frac{P_\theta - P_{60°}}{P_0 - P_{60°}} \quad .$$

It is easy to recognize the term $P_0 - P_{60°}$ as an approximation of $(1/2)\rho U_\infty^2$. However, now we are likely to account for the errors introduced by non-uniformity of the velocity profile. Thus, in summary, this coefficient has several advantages: it tends to compensate for the pressure gradient, blockage effects, irregularity of the velocity profile and possible errors in pressure measurements caused by electrical drifts of the pressure sensing system (the electrical drift was discussed in Chapter 2). Furthermore, in conjunction with the Reynolds number (based on average flow velocity and sphere diameter), it promises to assist in comparison with similar data by other investigators using different test facilities.

A question may arise as to the possible difficulty this new definition may cause in comparing test

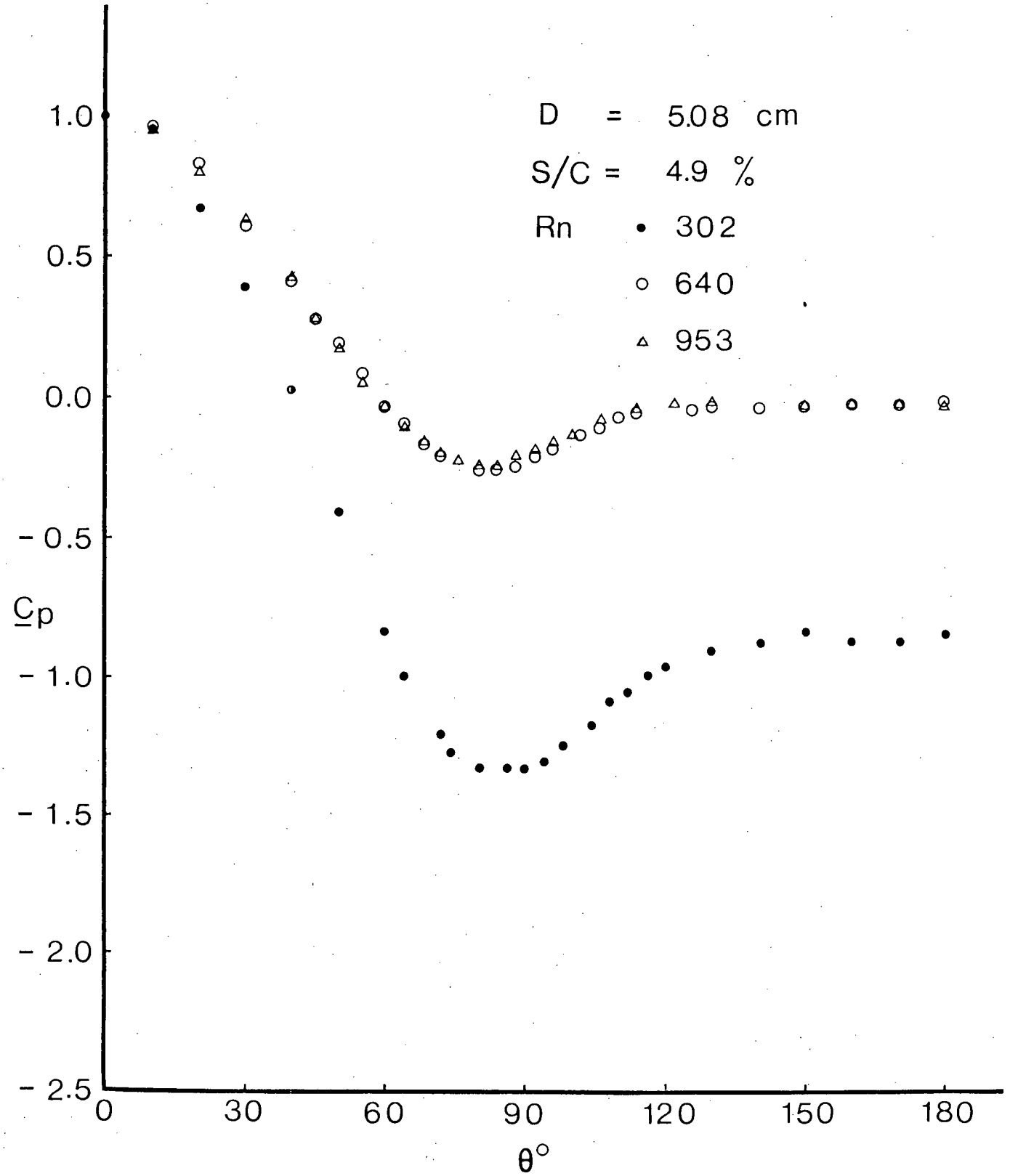

Figure 3-2 Typical pressure profiles for a sphere using the conventional definition of pressure coefficient, $C_p = (P_\theta - P_\infty)/(1/2)\rho U_c^2$. Note the pressure coefficient is zero in the vicinity of $\theta = 60°$

data with other published information. Fortunately, this does not present any problem. As shown in Appendix I , conventional pressure coefficient $\overline{C_p}$ can be written in terms of measured information as

$$\overline{C_p} = \frac{P_\theta - P_\infty}{1/2\rho U^2} = \frac{(P_\theta - P_{60°}) - (P_0 - P_{60°})}{1/2\rho U^2} + 1$$

with an error of <3% in the Reynolds number range investigated here.

Representative surface pressure data as presented in Figures 3-3 to 3-5 dramatically emphasize effectiveness of this new definition of the pressure coefficient.

The effect of differences in velocity profiles, as encountered by a model located at different stations in the test-section is shown in Figure 3-3. The conventional pressure coefficient $\overline{C_p}$ shows large variations almost over the entire surface except for a small region in the vicinity of the stagnation (Figure 3-3a). Although $\hat{C}_p$ fairs better in the region $\theta > 60°$, the plots are considerably distorted in the upstream direction (Figure 3-3b). Surprisingly, the new pressure coefficient C_p remains quite insensitive to the velocity changes over

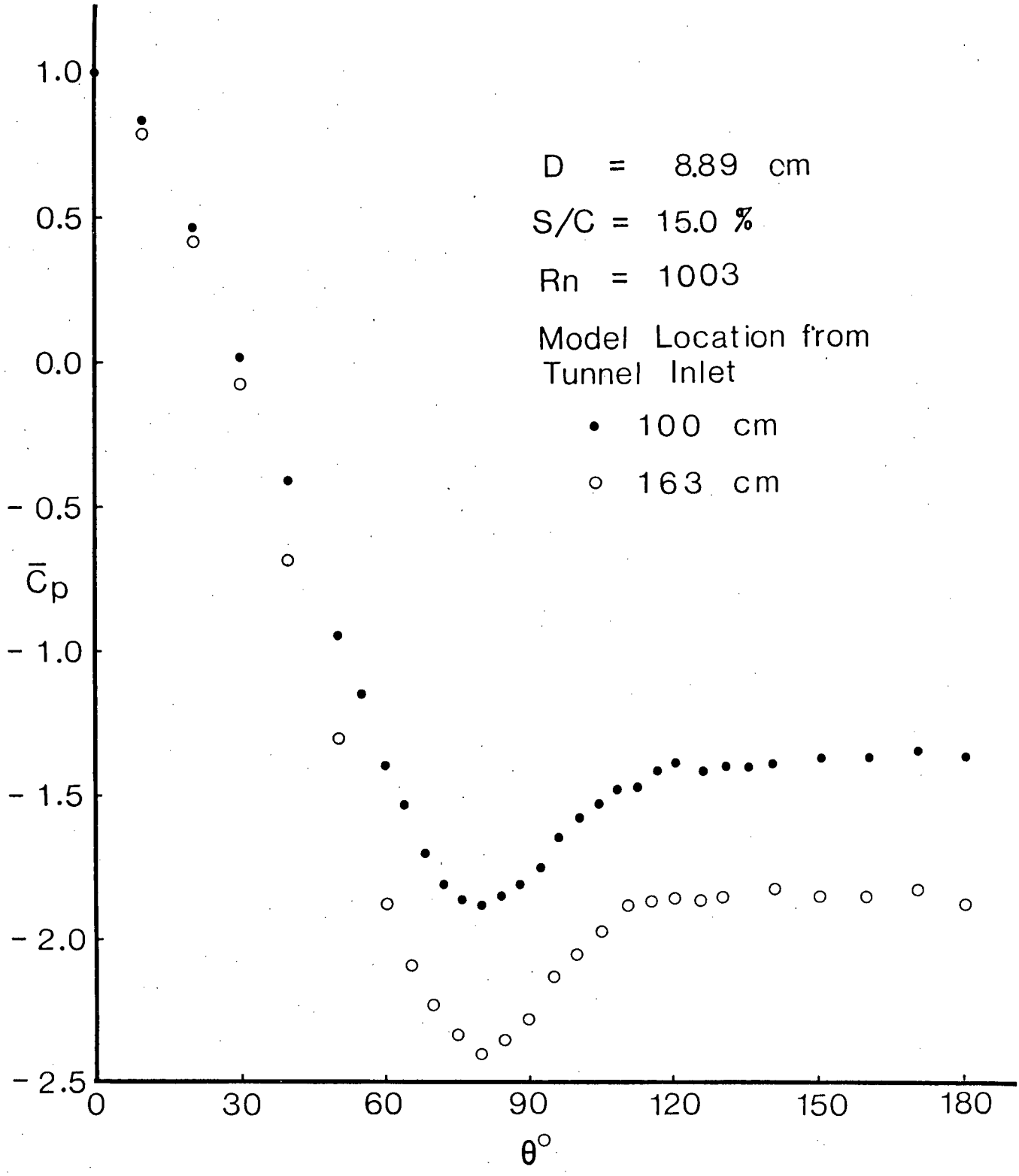

Figure 3-3 Plots showing sensitivity of different definitions for pressure coefficient to changes in velocity profile:
(a) $\bar{C}_p = (P_\theta - P_\infty)/(1/2)\rho U^2$

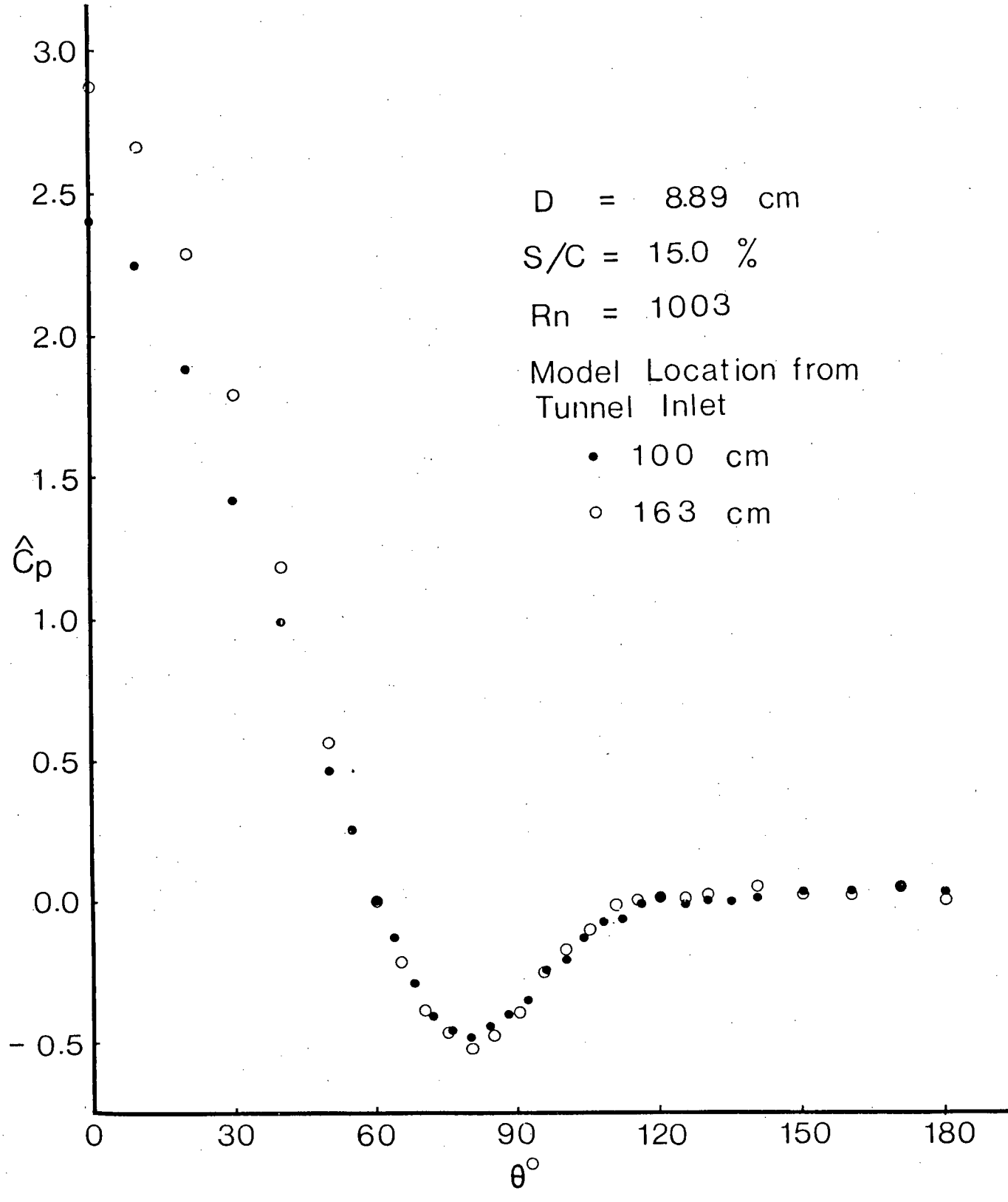

Figure 3-3 Plots showing sensitivity of different definitions for pressure coefficient to changes in velocity profile:

(b) $\hat{C}_p = (P_\theta - P_{60°})/(1/2)\rho U^2$

the entire surface even with the enlarged scale used in plotting the data (Figure 3-3c).

Figure 3-4 summarizes effect of the Reynolds number on the surface pressure for three different definitions of the pressure coefficient. Note that both the conventional definition $\overline{C_p}$ as well as its modification $\underline{C_p}$ as given by the use of centerline velocity are quite susceptible to the influence of Reynolds number (Figure 3-4a,b). On the other hand, the proposed definition C_p (Figure 3-4c) shows only slight sensitivity in and near the wake region. Note that the scale used in Figure 3-4c magnifies deviations by a factor of 2.5. Thus the new definition performs exceptionally well and makes the pressure distribution virtually independent of the Reynolds number in the range investigated. The relative independence of the wall confinement effects for the blockage ratio as large as 30.6% as shown in Figure 3-5 makes the proposed definition extremely attractive.

As pointed out before, the choice of reference pressure is quite arbitrary. However, effective compensation of errors introduced through various sources mentioned earlier will indeed depend on a given P_r for a specific pressure gradient, velocity profile, blockage,

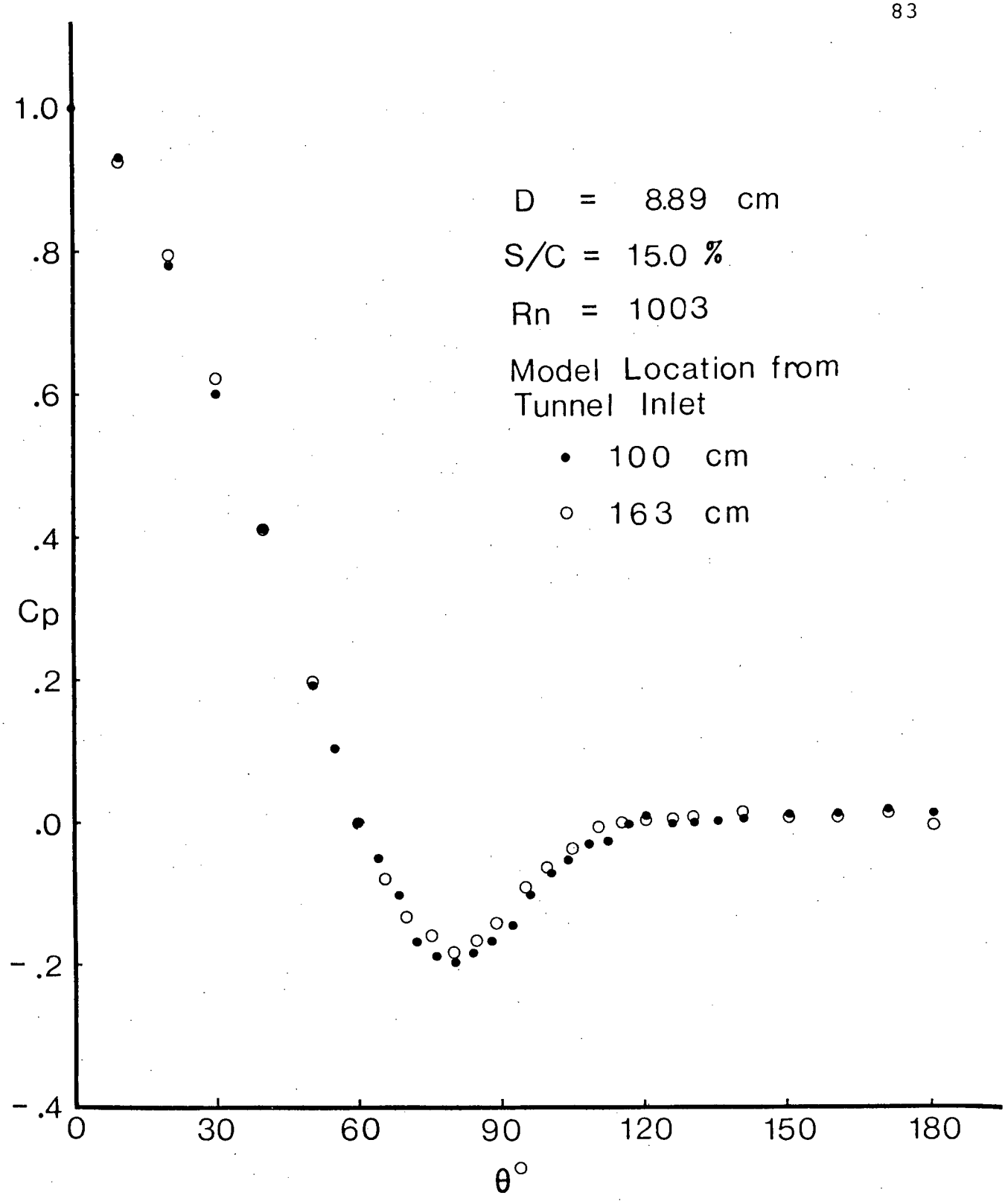

Figure 3-3 Plots showing sensitivity of different definitions for pressure coefficient to changes in velocity profile:

(c) $C_p = (P_\theta - P_{60°})/(P_0 - P_{60°})$

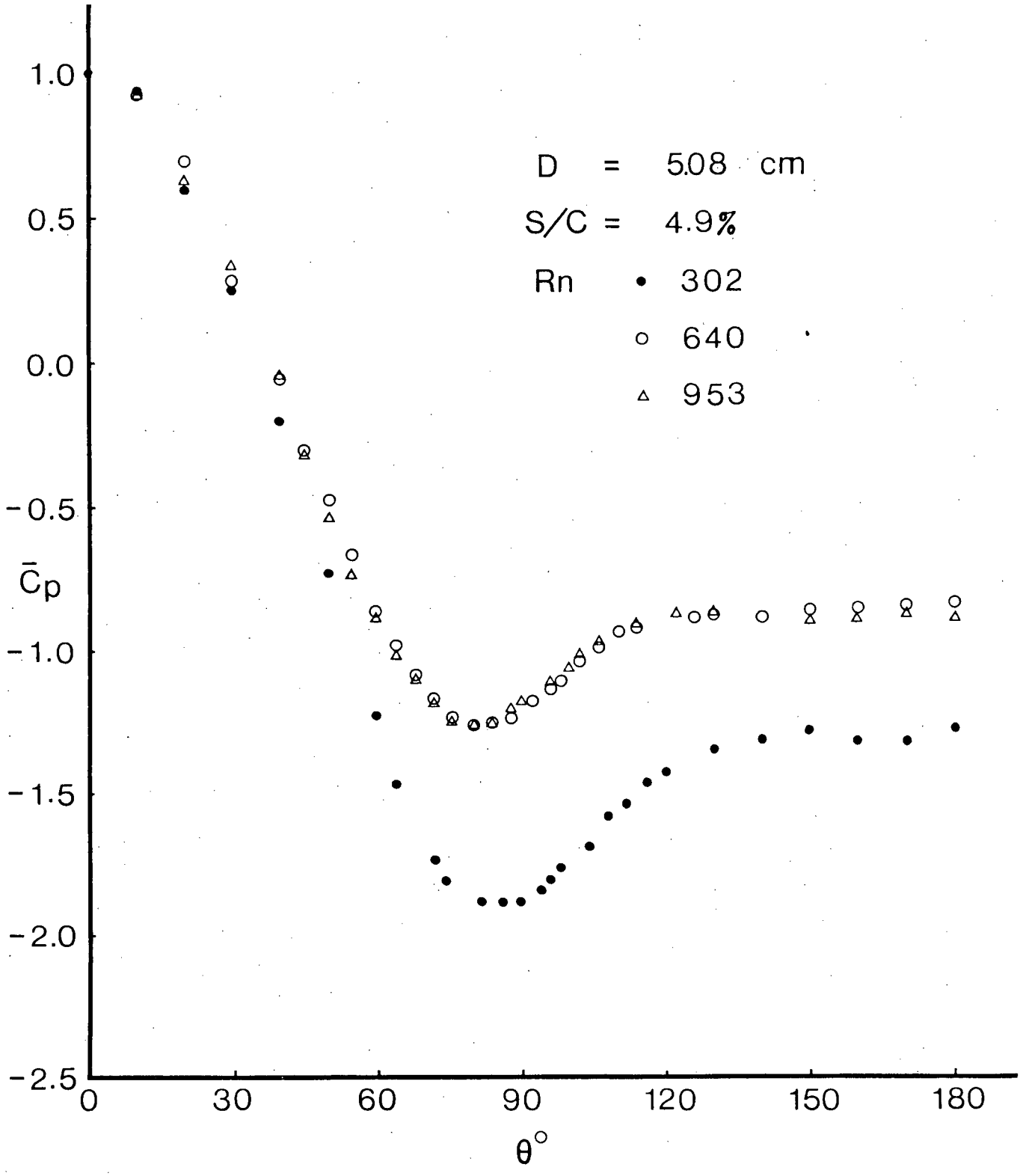

Figure 3-4 Effect of Reynolds number on surface pressure distribution in terms of:
(a) $\bar{C}_p = (P_\theta - P_\infty)/(1/2)\rho U^2$

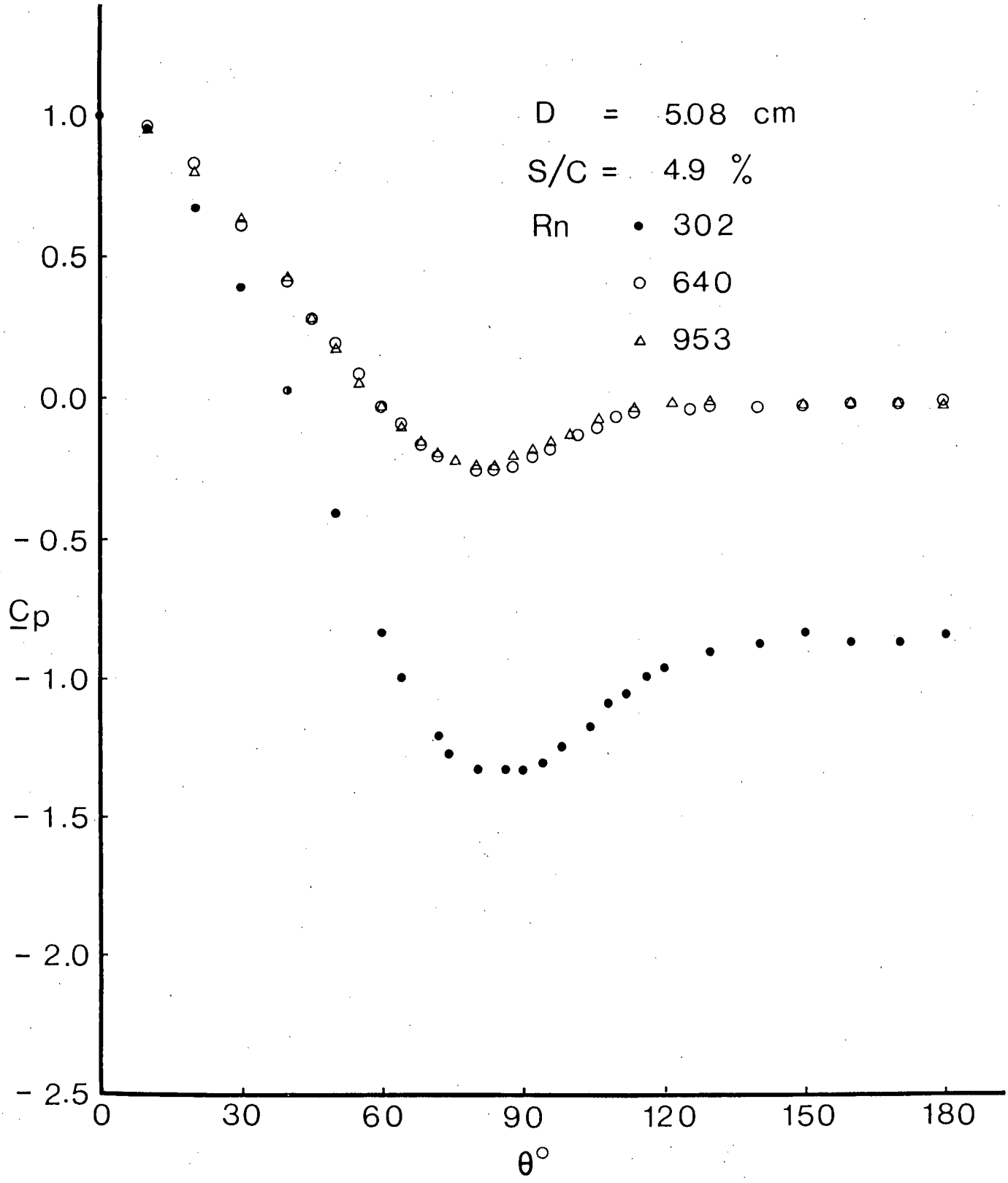

Figure 3-4 Effect of Reynolds number on surface pressure distribution in terms of:

(b) $\underline{C_p} = (P_\theta - P_\infty)/(1/2)\rho U_c^2$

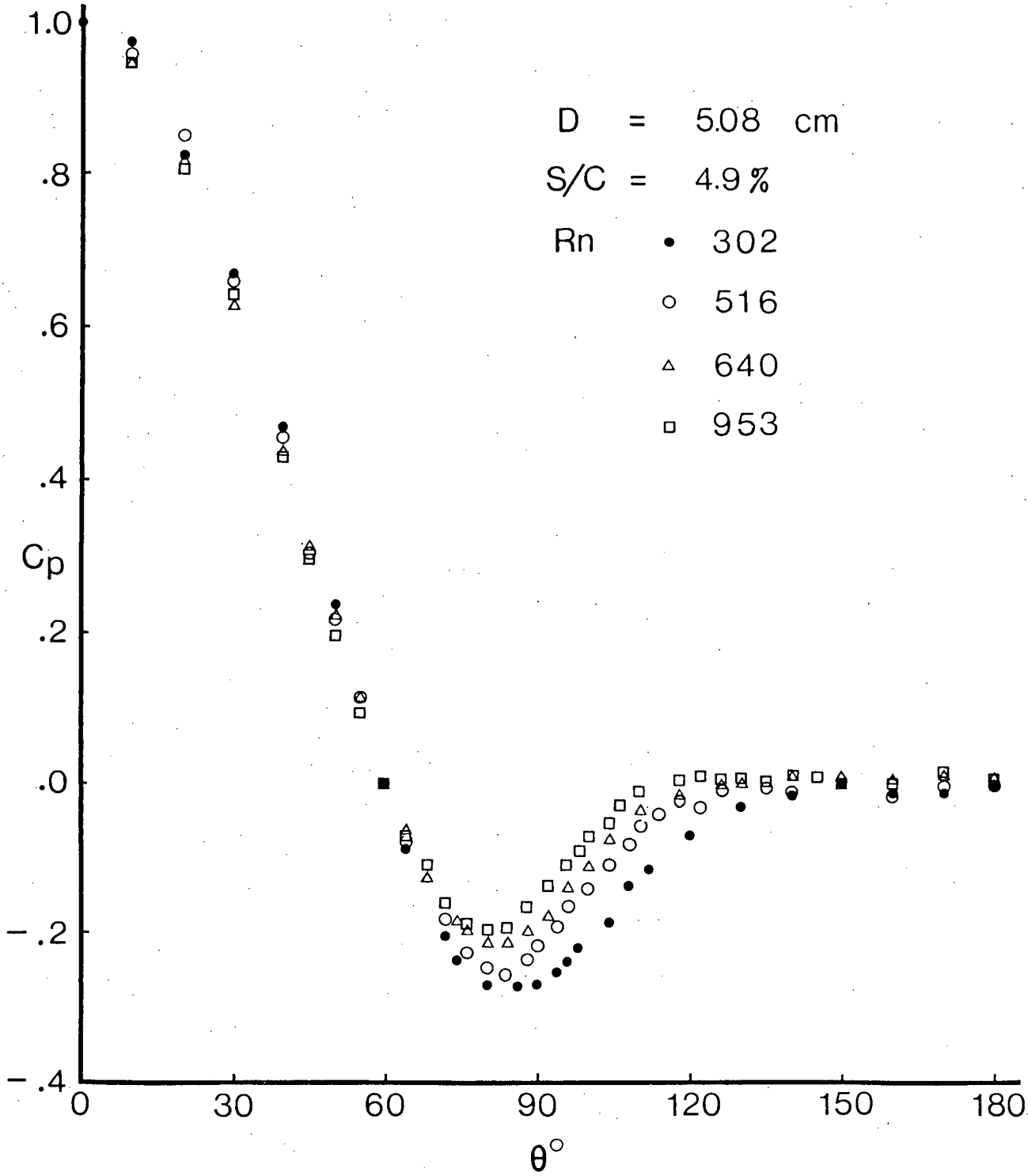

Figure 3-4 Effect of Reynolds number on surface pressure distribution in terms of:

(c) $C_p = (P_\theta - P_{60°})/(P_0 - P_{60°})$

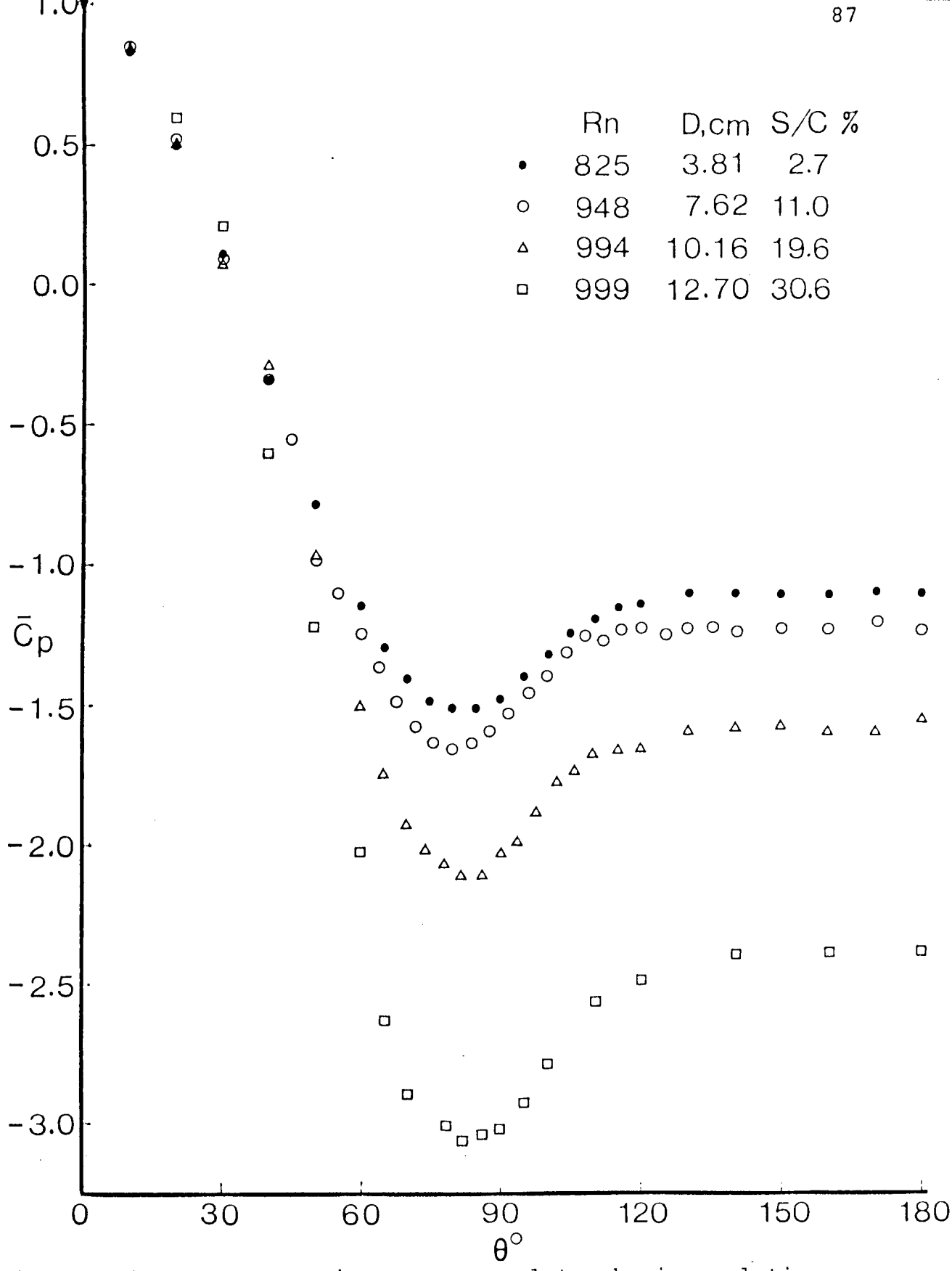

Figure 3-5 Representative pressure plots showing relative insensitivity of the proposed pressure coefficient to blockage effects: (a) conventional pressure coefficient ($\bar{C}_p$) based on average velocity, $\bar{C}_p = (P_\theta - P_\infty)/(1/2)\rho U^2$

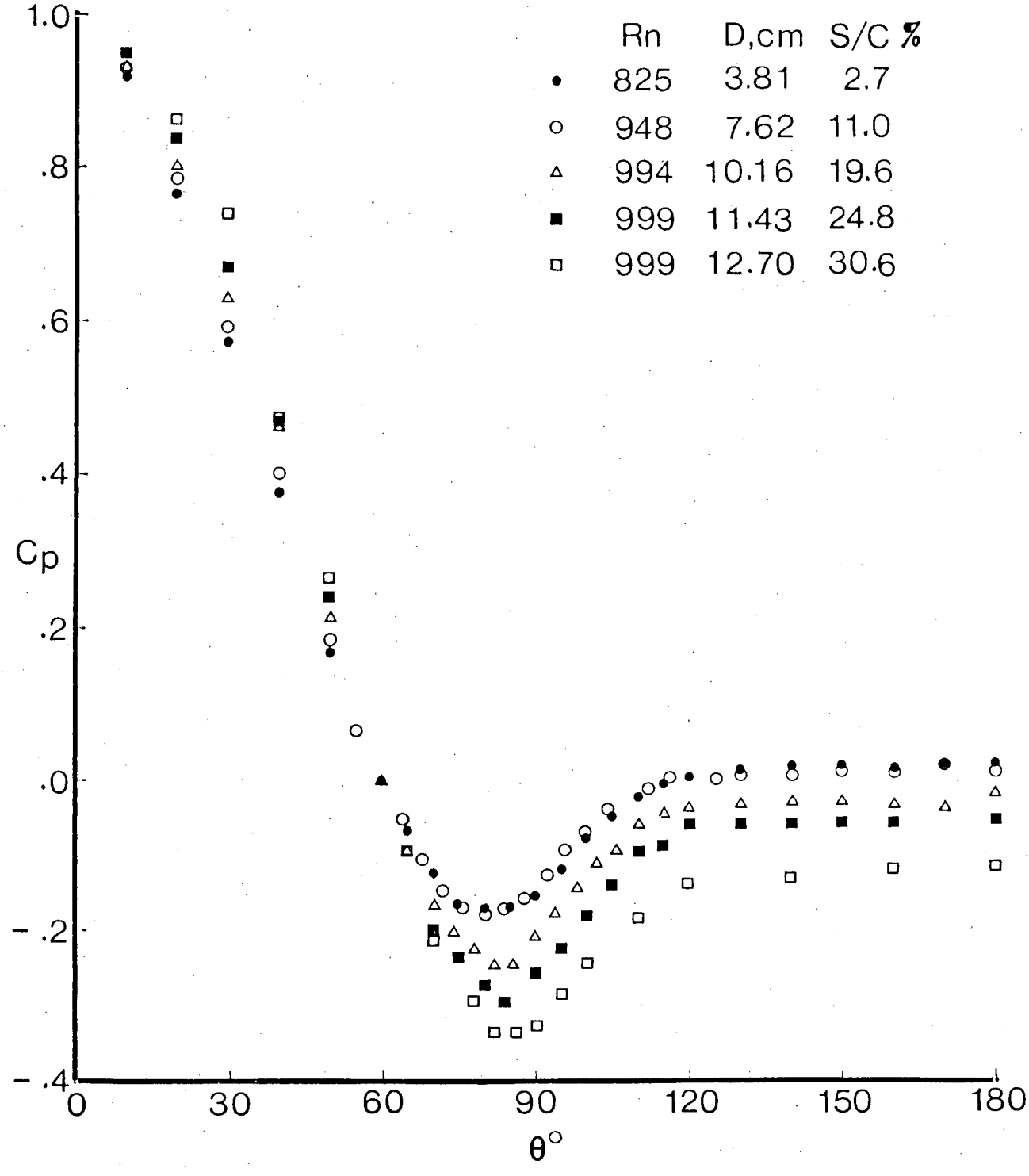

Figure 3-5 Representative pressure plots showing relative insensitivity of the proposed pressure coefficient to blockage effects: (b) suggested pressure coefficient defined as

$$C_p = (P_\theta - P_{60°})/(P_0 - R_{60°})$$

geometry of test model, etc. Hence, although the proposed definition is likely to be less dependent on fluid dynamical parameters compared to the conventional $\overline{C_p}$, the degree of variation may indeed depend upon the chosen reference pressure. Data reduced using $\theta = 30°$, $60°$, and $90°$ as references substantiate this observation. Thus a question concerning the optimum choice of the reference pressure arises. In general, it would be impossible to identify an optimum reference for all cases. However, recognizing the fact that for most bluff bodies the difference between the minimum and base pressures remains relatively constant, reference θ in the range of around $50° - 120°$ is likely to lead to good results. Figure 3-6 shows the effect of velocity profile, Reynolds number and blockage on the pressure coefficient defined using $P_{90°}$ as reference. Note that plots remain essentially unaffected except for a small region in the vicinity of the stagnation.

3.2 Effect of Reynolds Number

Figures 3-7 through 3-9 summarize a rather comprehensive set of data on the surface pressure distribution for a sphere as affected by the Reynolds number for a given blockage in the range 4.9 - 30.6%. Results

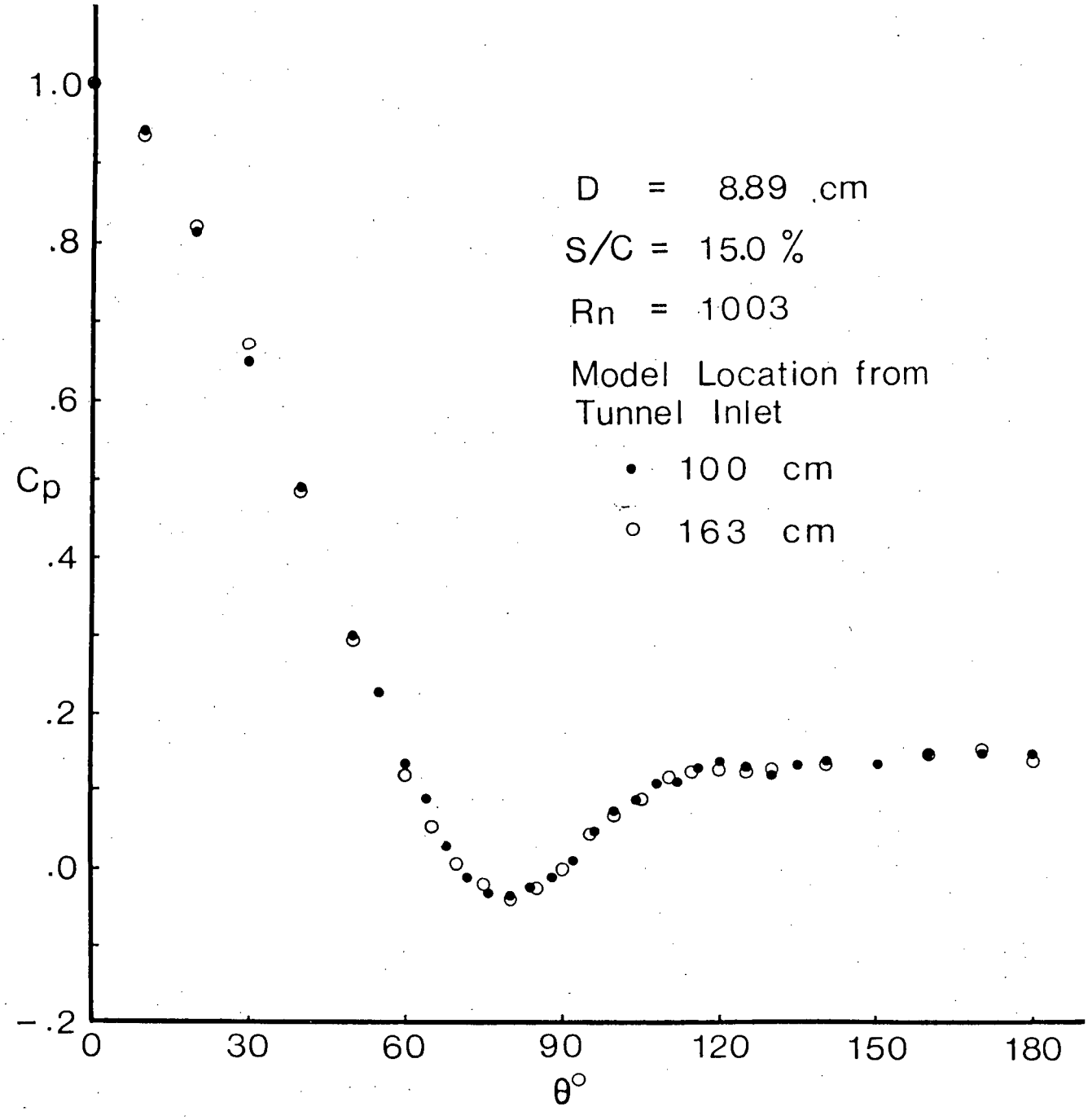

Figure 3-6 Surface pressure distribution on spheres using $P_{90°}$ as reference. Note the plots show very little dependence on; (a) velocity profile

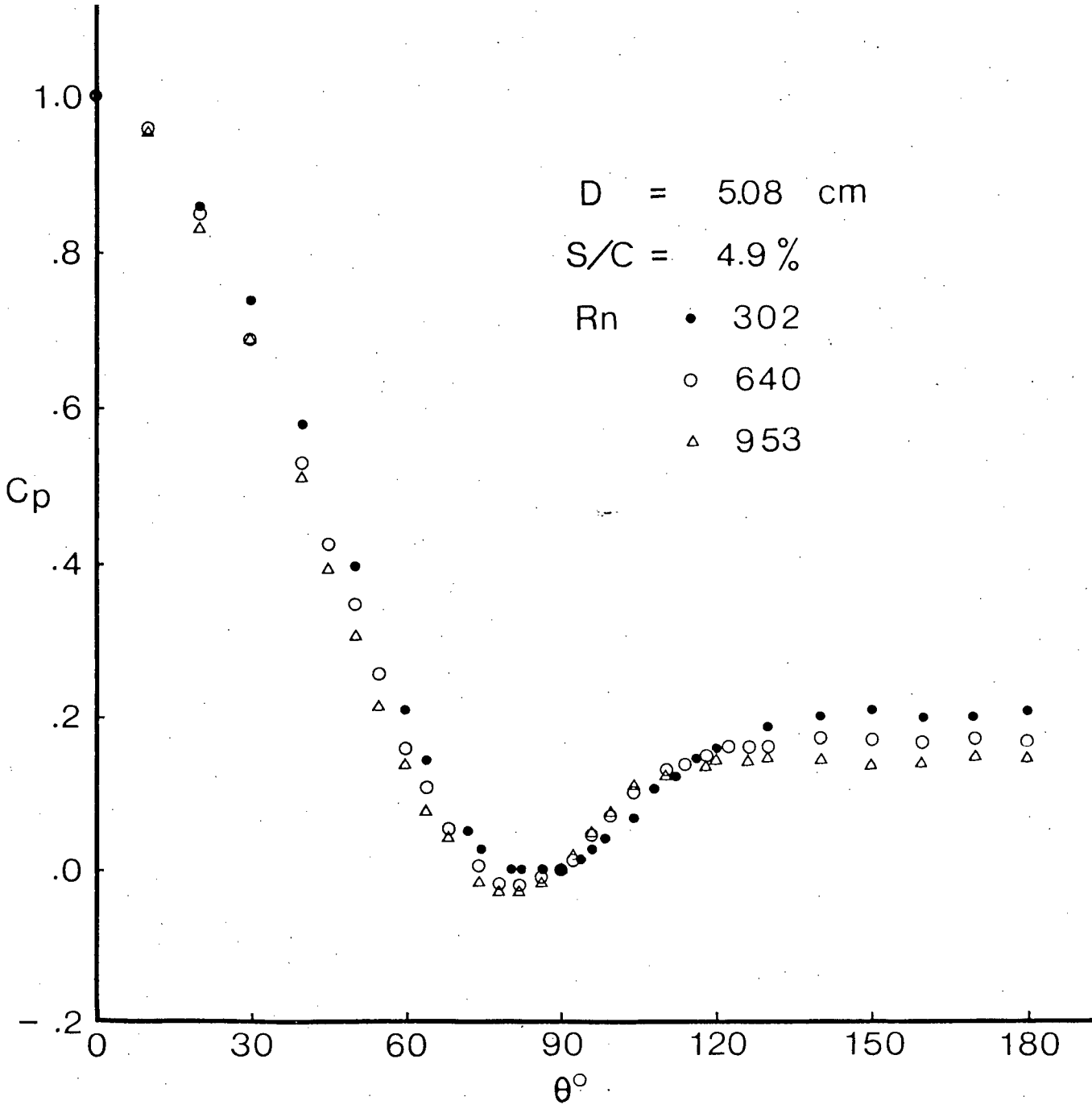

Figure 3-6 Surface pressure distribution on spheres using $P_{90°}$ as reference. Note the plots show very little dependence on:(b) Reynolds number

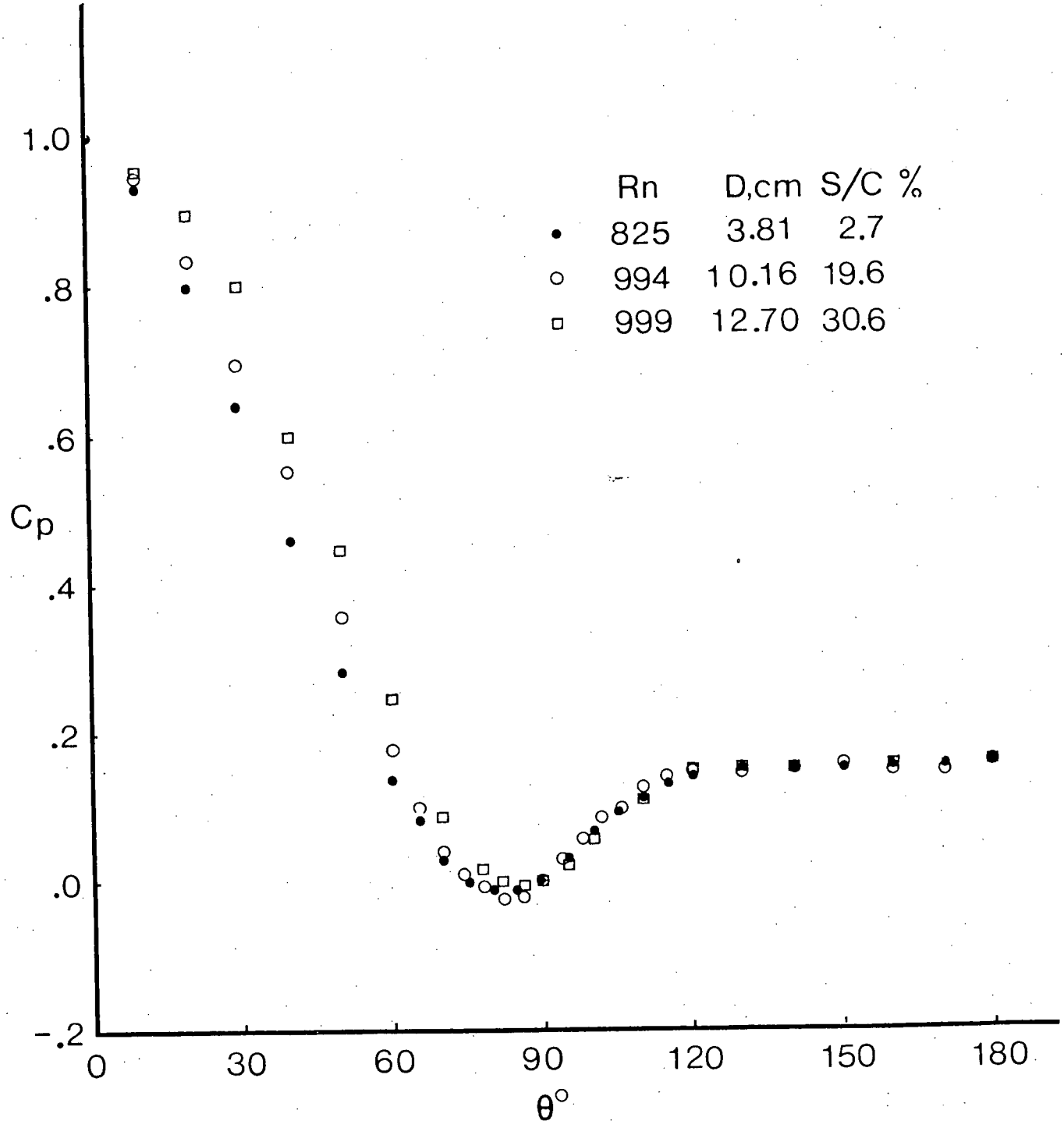

Figure 3-6 Surface pressure distribution on spheres using $P_{90°}$ as reference. Note the plots show very little dependence on: (c) blockage

by other investigators are also included for comparison when available. In most cases, the information is presented using the new definition of the pressure coefficient discussed before, however, typical results in terms of $\overline{C_p}$ are also included to illustrate identical trends predicted by both approaches (Figures 3-7b and 3-8d).

At the outset one can say that the effect of Reynolds number is essentially confined to the region downstream of the zero pressure point and even here it is limited to $R_n < 1000$, except for the very high blockage ratio of 30.6%. In general, the effect of Reynolds number is to increase the minimum as well as the wake pressures. Furthermore, location of the minimum pressure point together with the approximate location of the separation point (as indicated by the beginning of the uniform pressure region of the wake) tend to shift a little upstream. It is of some interest to note that in the region bounded by the front stagnation and the zero pressure point, the effect of Reynolds number appears to be just the opposite, i.e., the pressure decreases with an increase in the Reynolds number.

Figure 3-7(c) compares the present data with the higher Reynolds number results as obtained by Aminzadeh[47] and Maxworthy[11]. Aminzadeh's pressure data at $R_n = 5848$ tend to substantiate earlier observation

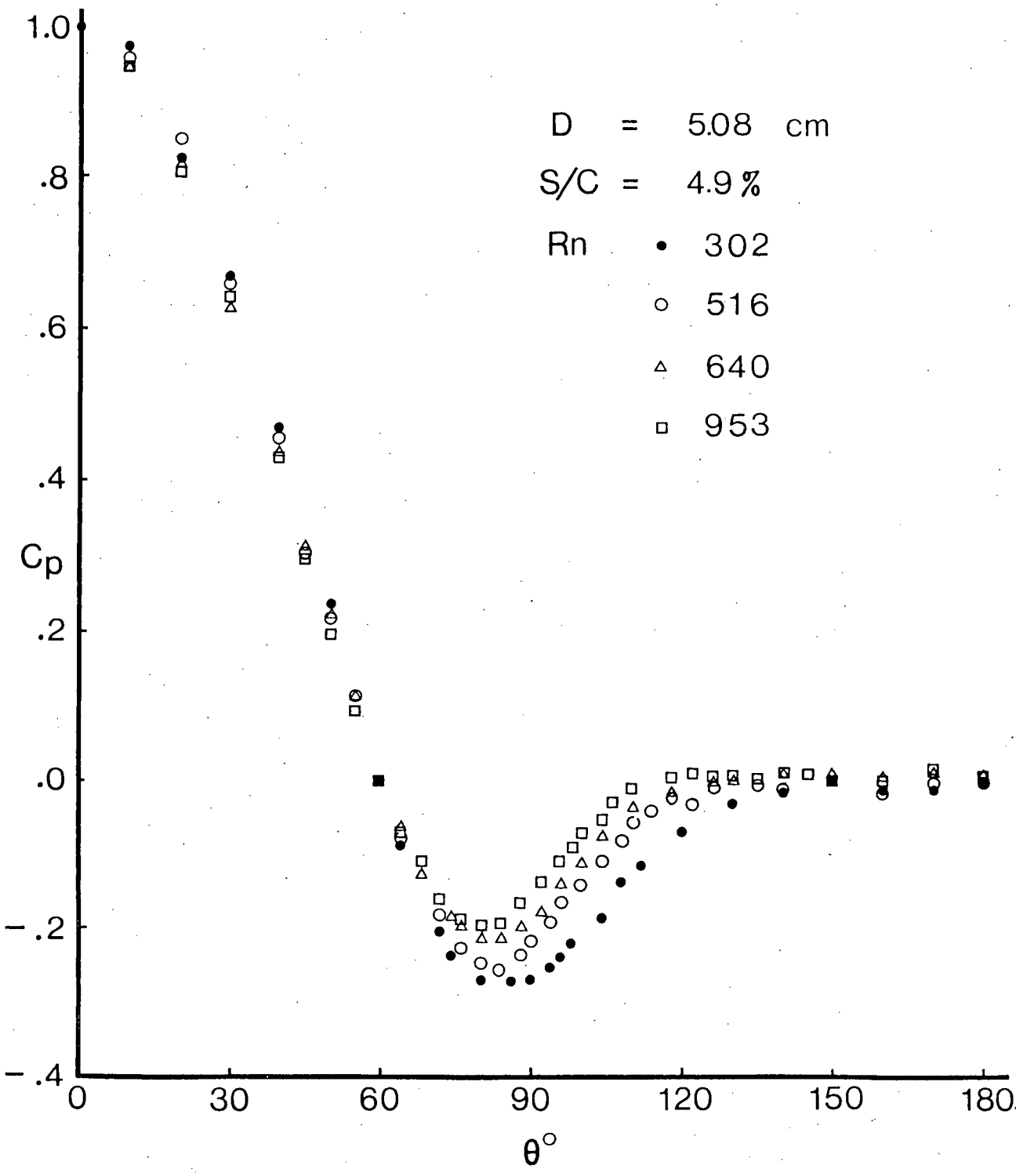

Figure 3-7 Surface pressure distribution as affected by Reynolds number at a small blockage ratio of 4.9%:

(a) $C_p = (P_\theta - P_{60°})/(P_0 - P_{60°})$

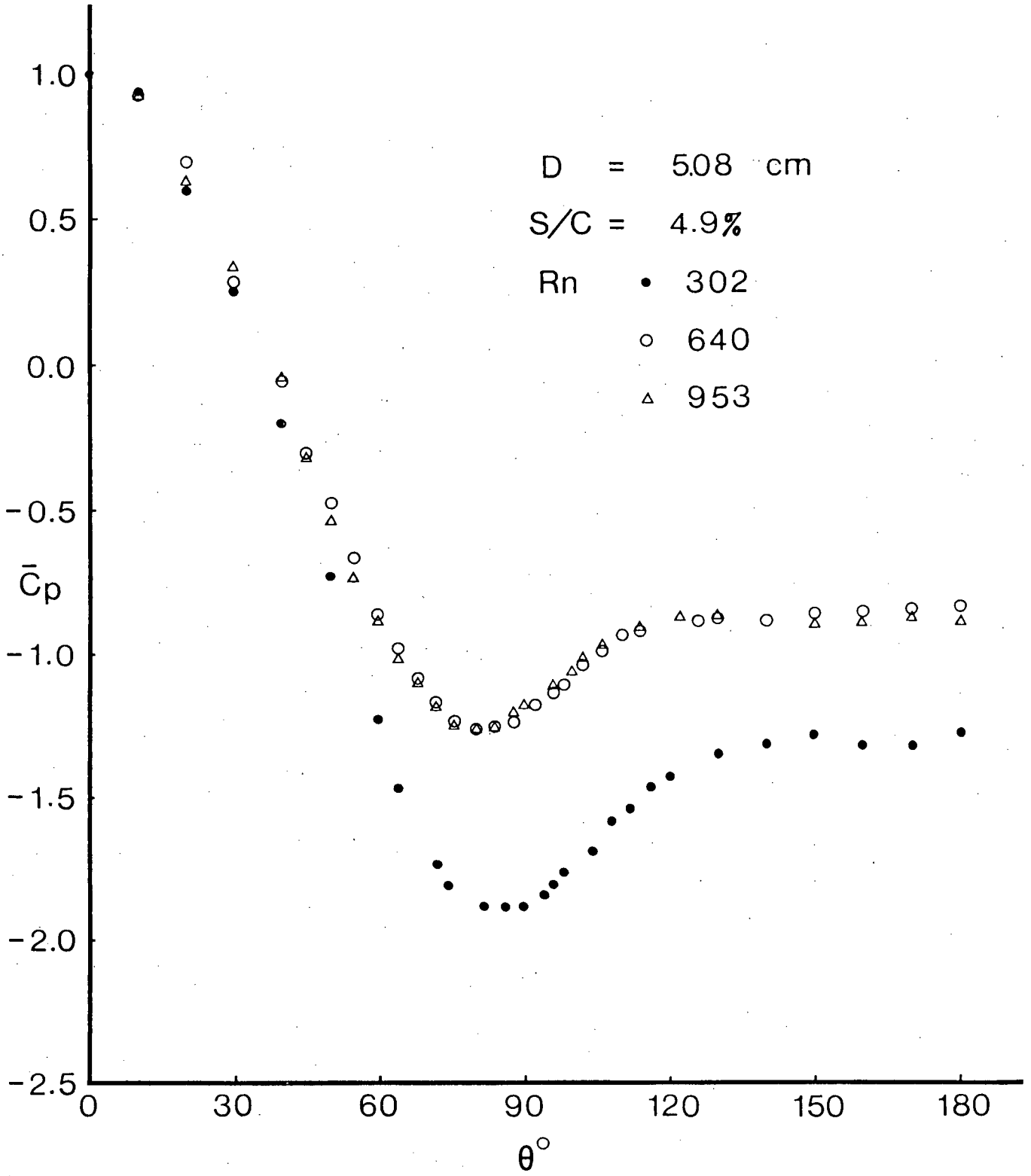

Figure 3-7 Surface pressure distribution as affected by Reynolds number at a small blockage ratio of 4.9%:

(b) $\bar{C}_p = (P_\theta - P_\infty)/(1/2)\rho U^2$

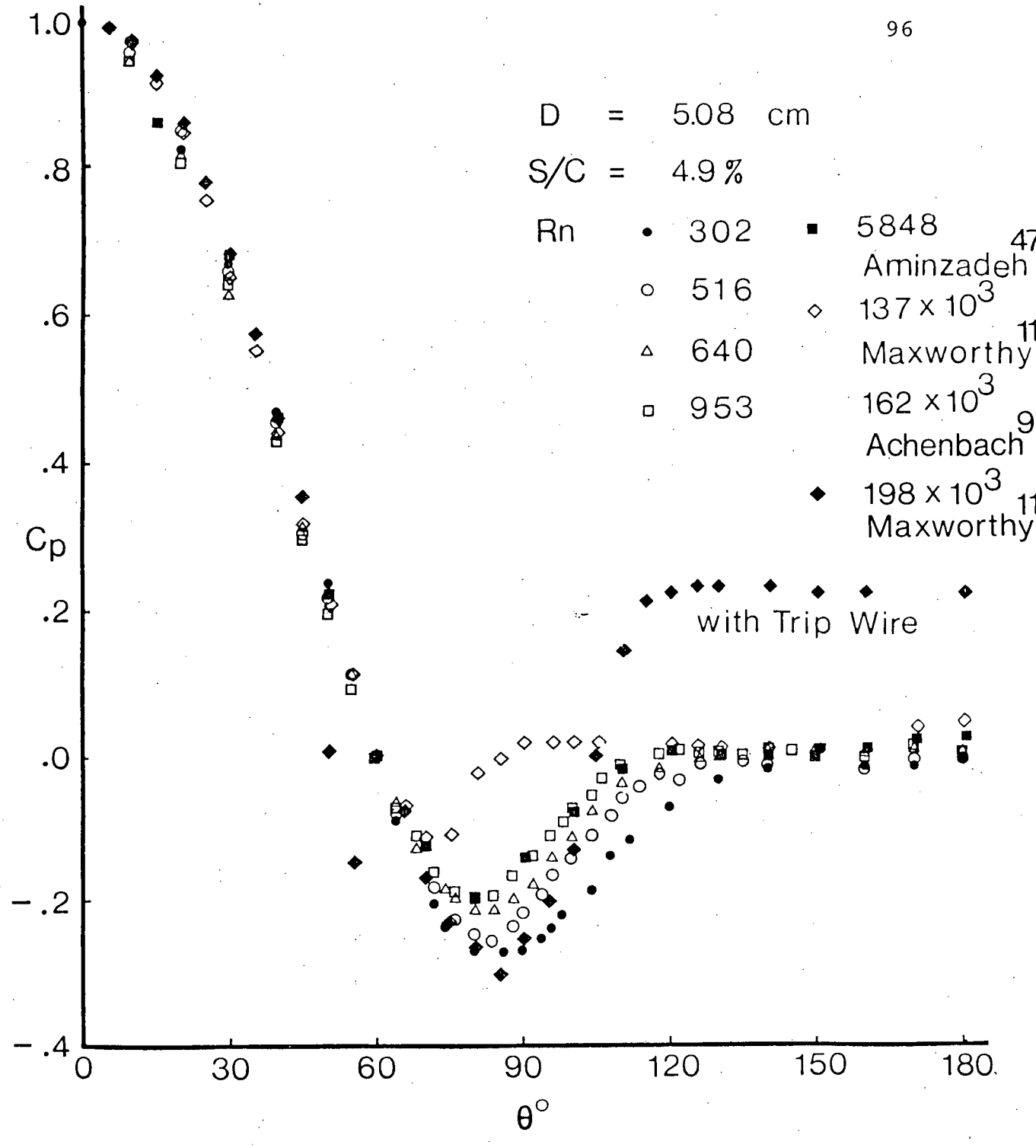

Figure 3-7 Surface pressure distribution as affected by Reynolds number at a small blockage ratio of 4.9%: (c) comparison with recent data by other investigators. Note the results by Maxworthy and Achenbach are near critical Reynolds number ($R_{n,cr} = 3.7 \times 10^5$, Reference 9)

concerning independence of the pressure for $R_n > 1000$. However, note the change in the pressure profile as one approaches the critical Reynolds number (Maxworthy[11], $R_n = 137 \times 10^3$). There is a sudden increase in the minimum pressure value and an upstream shift in the separation point. This is associated with the familiar slight increase in the drag in this region ($R_n = 6 \times 10^3 - 2 \times 10^5$). However, at the critical Reynolds number ($R_{n,critical} \doteqdot 2 \times 10^5$) there is a sudden rise in the base pressure and the downstream movement of the separation point resulting in the classical reduction in drag (Maxworthy[11], $R_n = 198 \times 10^3$).

At higher blockage ratios of 11 - 19.6% (Figure 3-8) essentially the same trend is maintained. However, for any further increase in the wall confinement the base pressure begins to be a little sensitive to the Reynolds number (Figure 3-9). It is interesting to note here that Modi and Sherbiny[59] also observed the same trend in their study with a circular cylinder of 35.5% blockage.

3.3 Wall Confinement Effects

Figures 3-10 and 3-11 summarize results on the influence of blockage offered by the spherical models. It must be recognized that the minimum and maximum attainable speeds in any liquid tunnel are fixed by

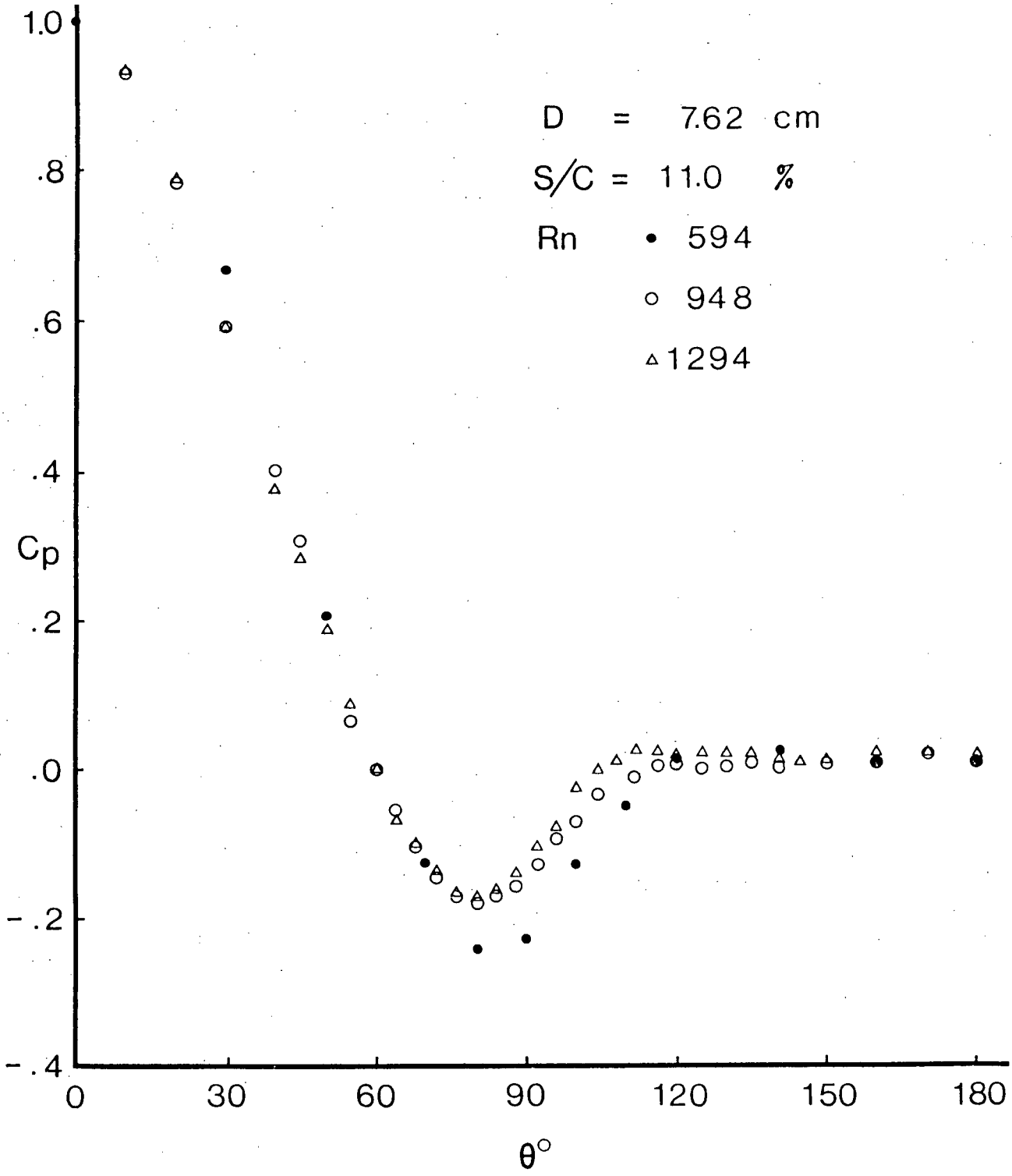

Figure 3-8 Pressure plots showing their relative insensitivity to Reynolds number > 1000 and for intermediate values of blockage: (a) C_p, S/C = 11.0%

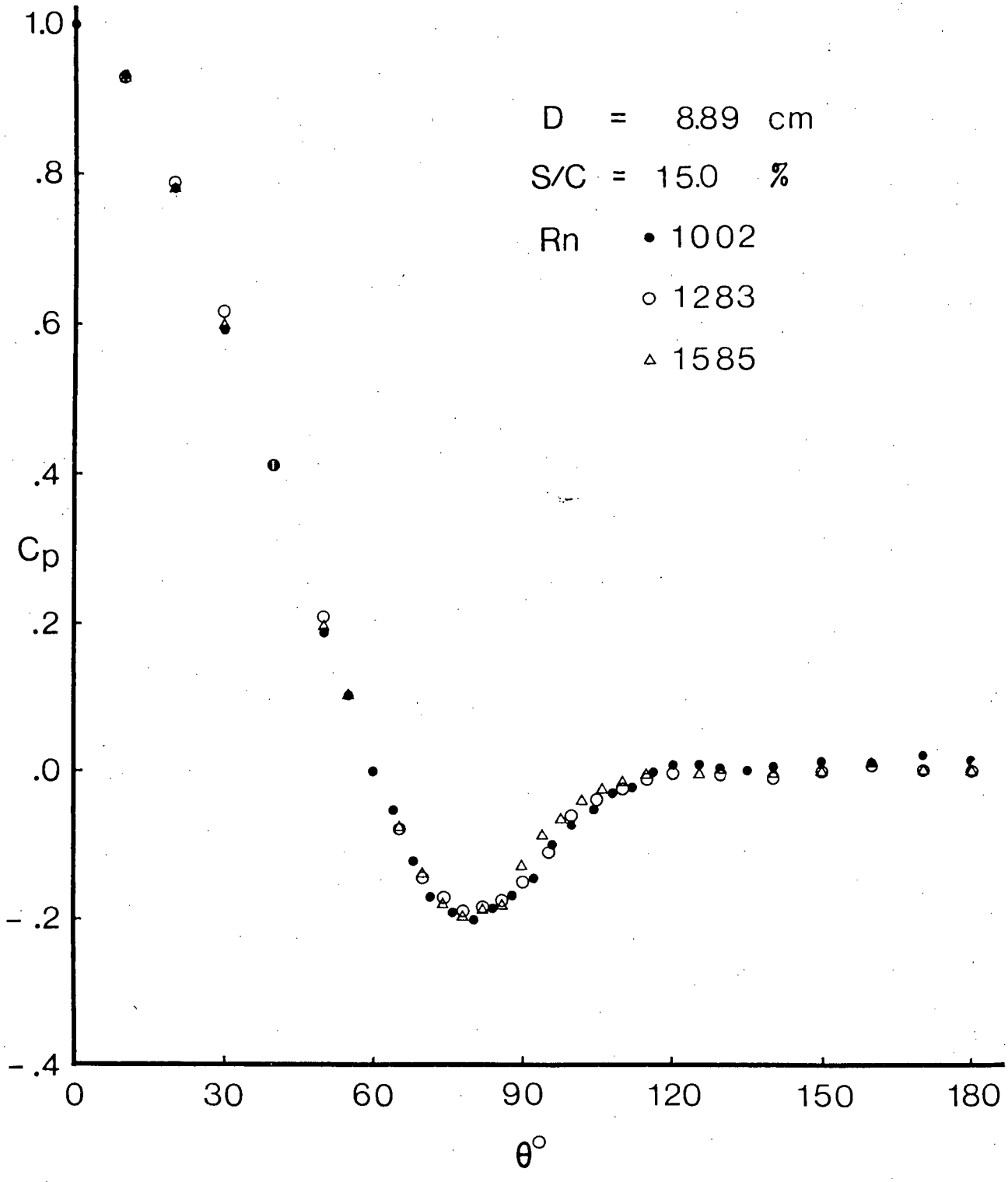

Figure 3-8 Pressure plots showing their relative insensitivity to Reynolds number ≥ 1000 and for intermediate values of blockage: (b) $\bar{C}_p$, S/C = 15.0%

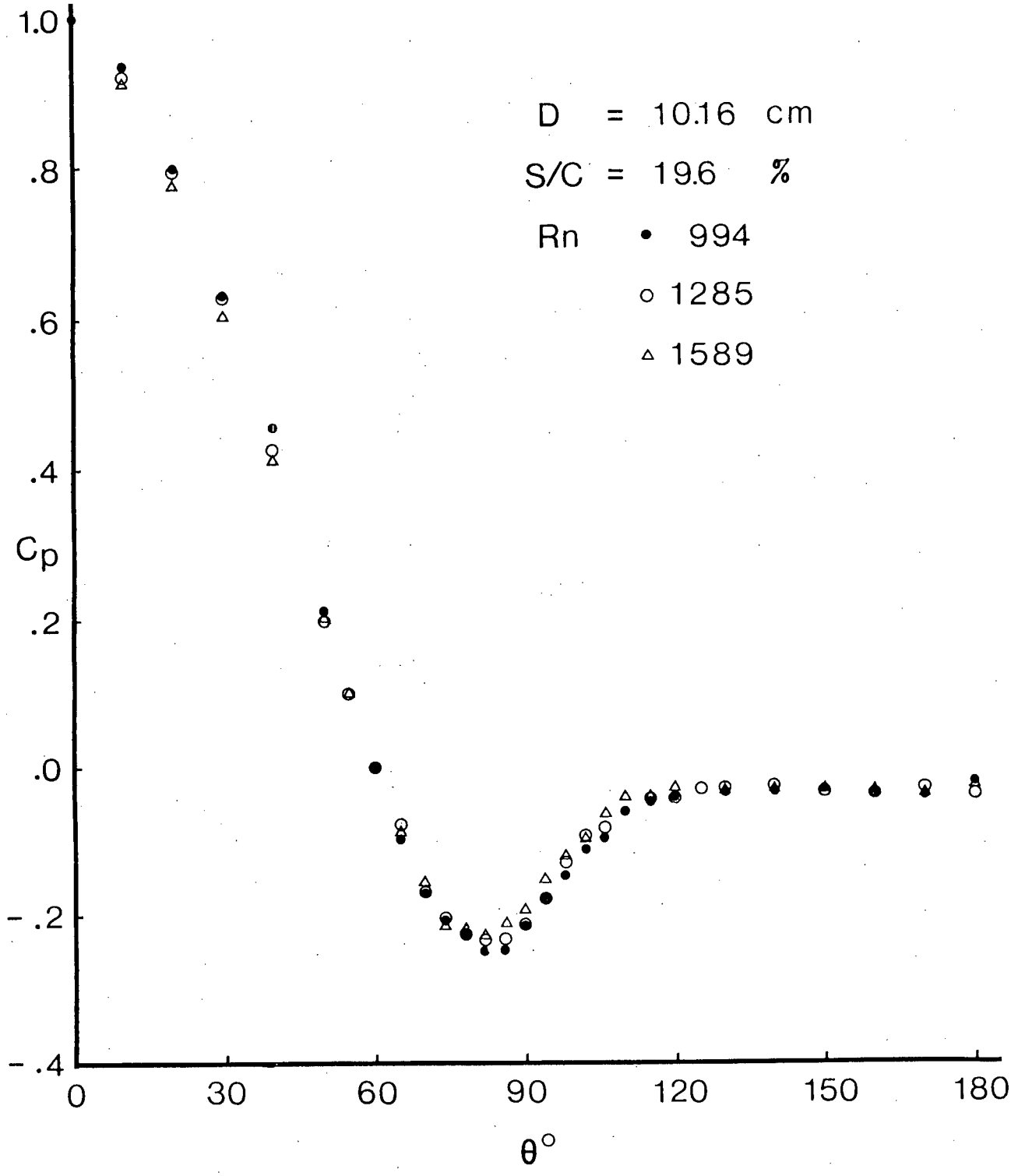

Figure 3-8 Pressure plots showing their relative insensitivity to Reynolds number ≥ 1000 and for intermediate values of blockage: (c) $\bar{C}_p$, S/C = 19.6%

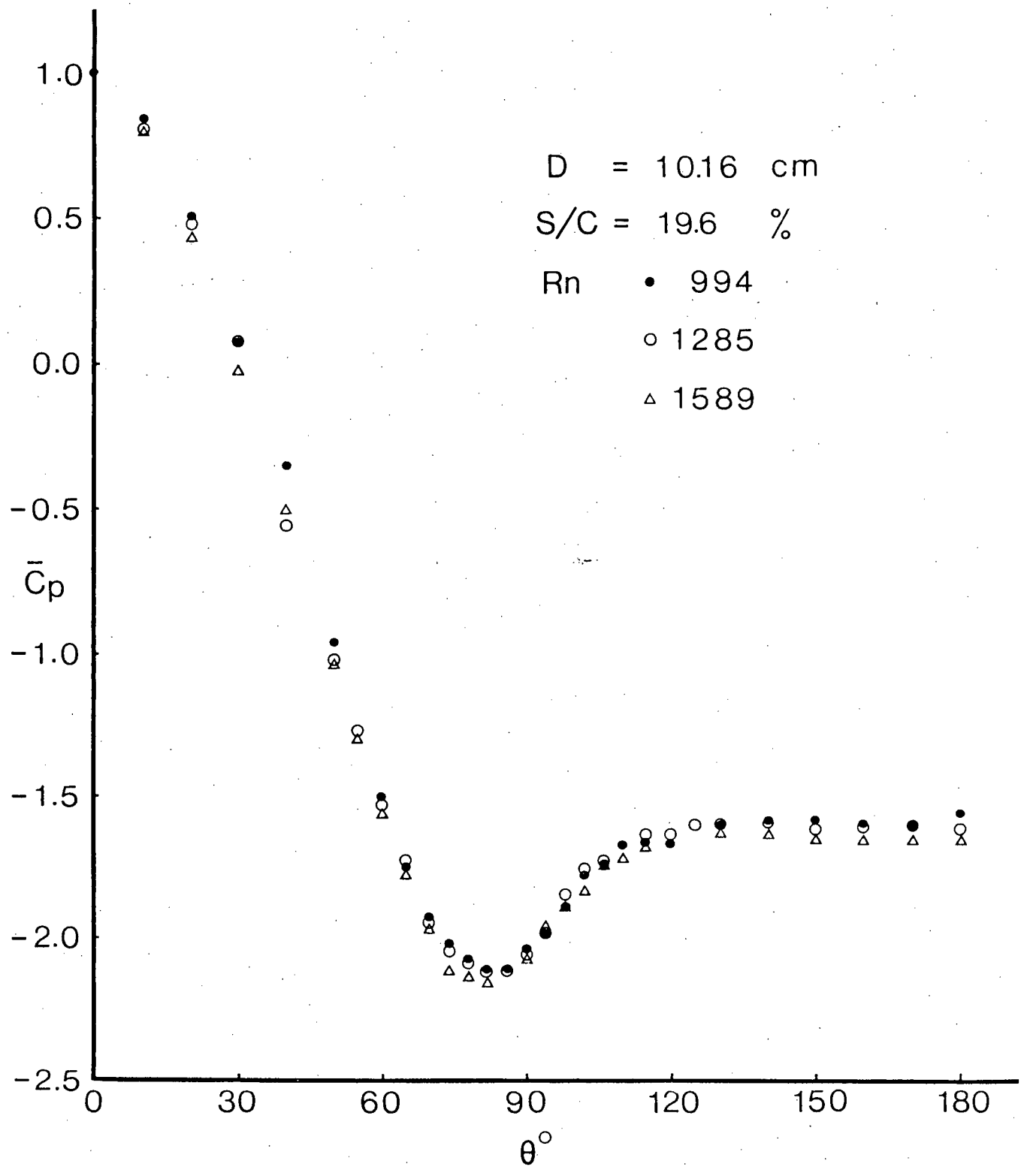

Figure 3-8 Pressure plots showing their relative insensitivity to Reynolds number ≥ 1000 and for intermediate values of blockage: (d) $\bar{C}_p$, S/C = 19.6%

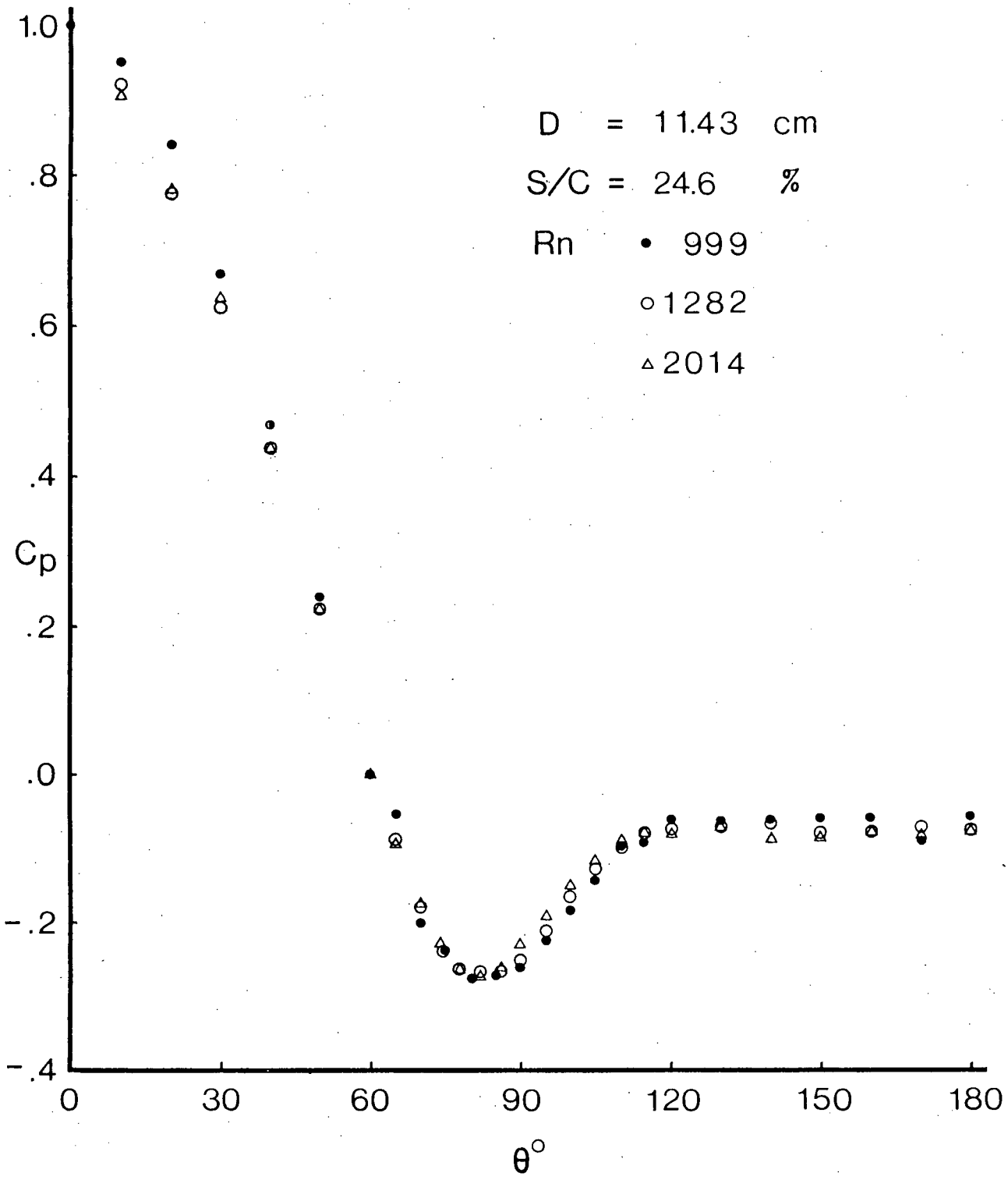

Figure 3-9 Reynolds number effect on the pressure distribution at higher blockage ratios:

(a) C_p, S/C = 24.6%

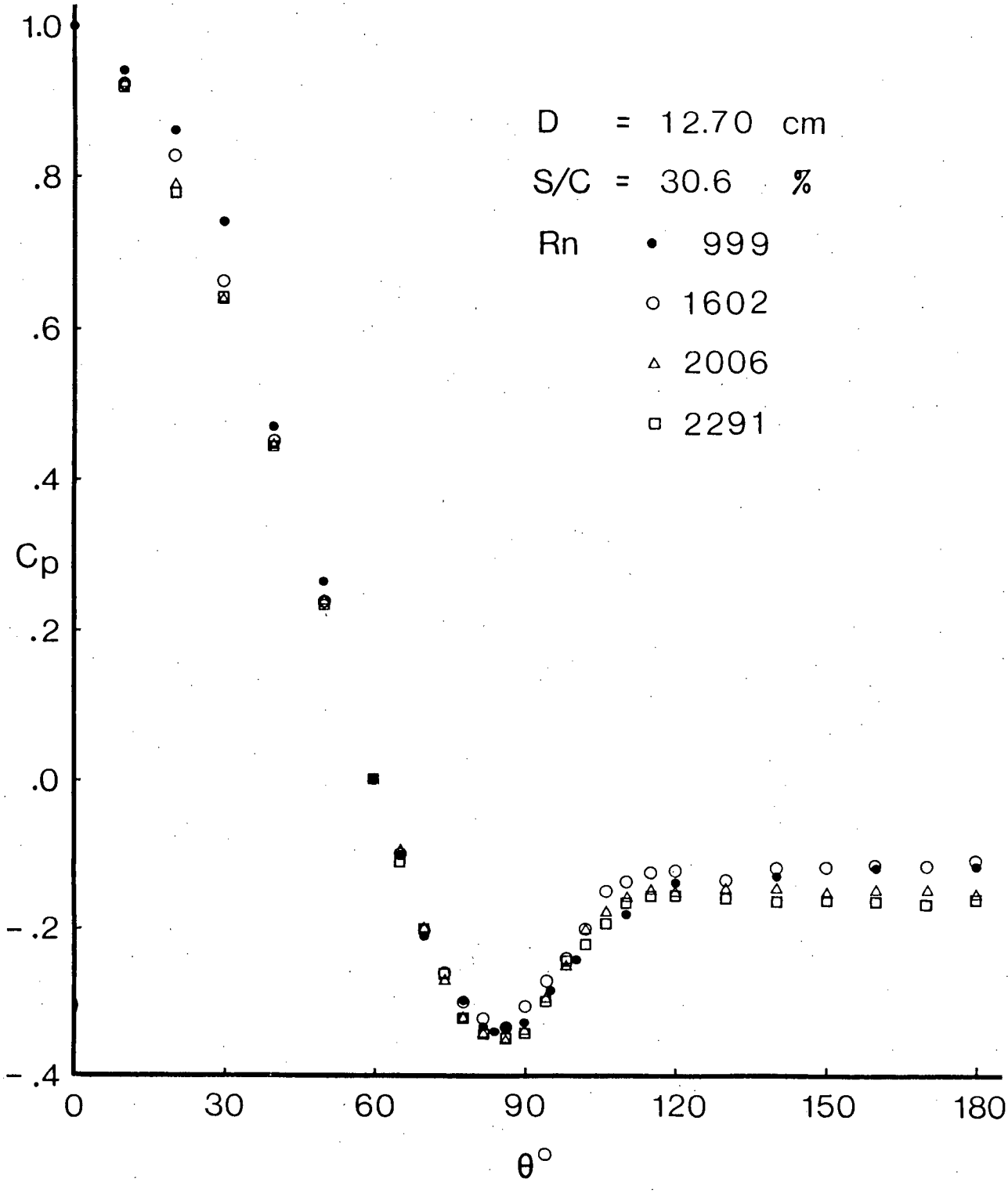

Figure 3-9 Reynolds number effect on the pressure distribution at higher blockage ratios:

(b) C_p, S/C = 30.6%

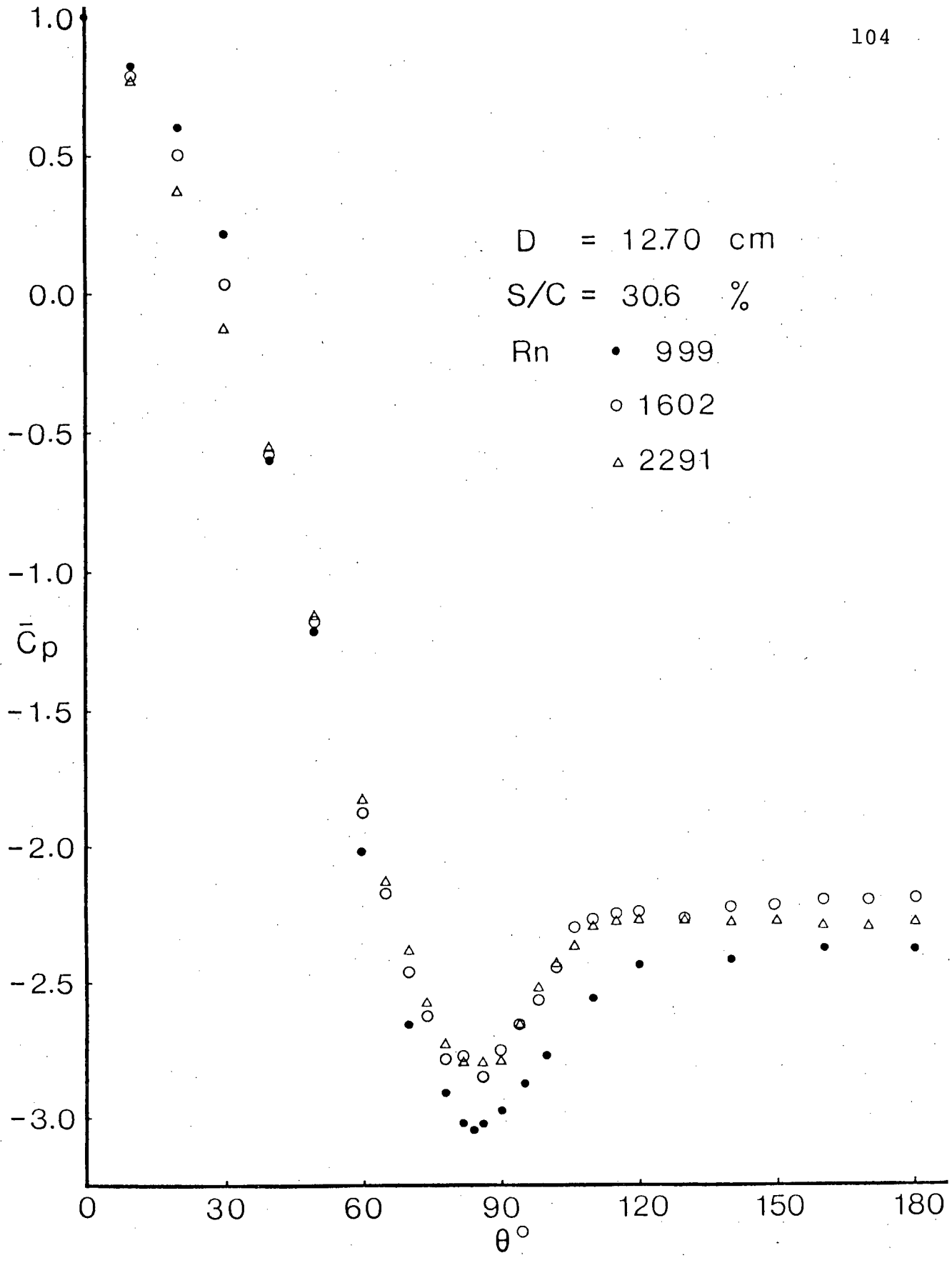

Figure 3-9 Reynolds number effect on the pressure distribution at higher blockage ratios:
(c) $\bar{C}_p$, S/C = 30.6%

design considerations. For the present facility they were 0.5 cm/s and 15 cm/s, respectively. Hence, for a given blockage, it wasn't always possible to cover the desired range of Reynolds number (300 - 2000). This has led to unavoidable gaps in the results presented here, however, the trends are reasonably well established for $R_n > 600$. From Figure 3-10 it is apparent that for up to around 11%, the confinement effects are essentially negligible but beyond that the blockage has definite tendency to reduce the minimum and base pressures (Figure 3-11). The minimum pressure point shows a distinct rearward shift. Similar downstream movement of the separation point can also be discerned although it is not quite distinct. A flow visualization study described later (Section 3.6) confirmed this trend. As can be expected from the previous discussion, the blockage effect remains essentially the same for $R_n > 1000$. Corresponding results in terms of conventional pressure coefficient were presented earlier (Figure 3-4d).

Figure 3-12 shows variation of the average base pressure and the minimum pressure with blockage. Up to S/C of around 12 - 15% the base pressure as well as the minimum pressure remains essentially constant, however, beyond that there is a distinct reduction in

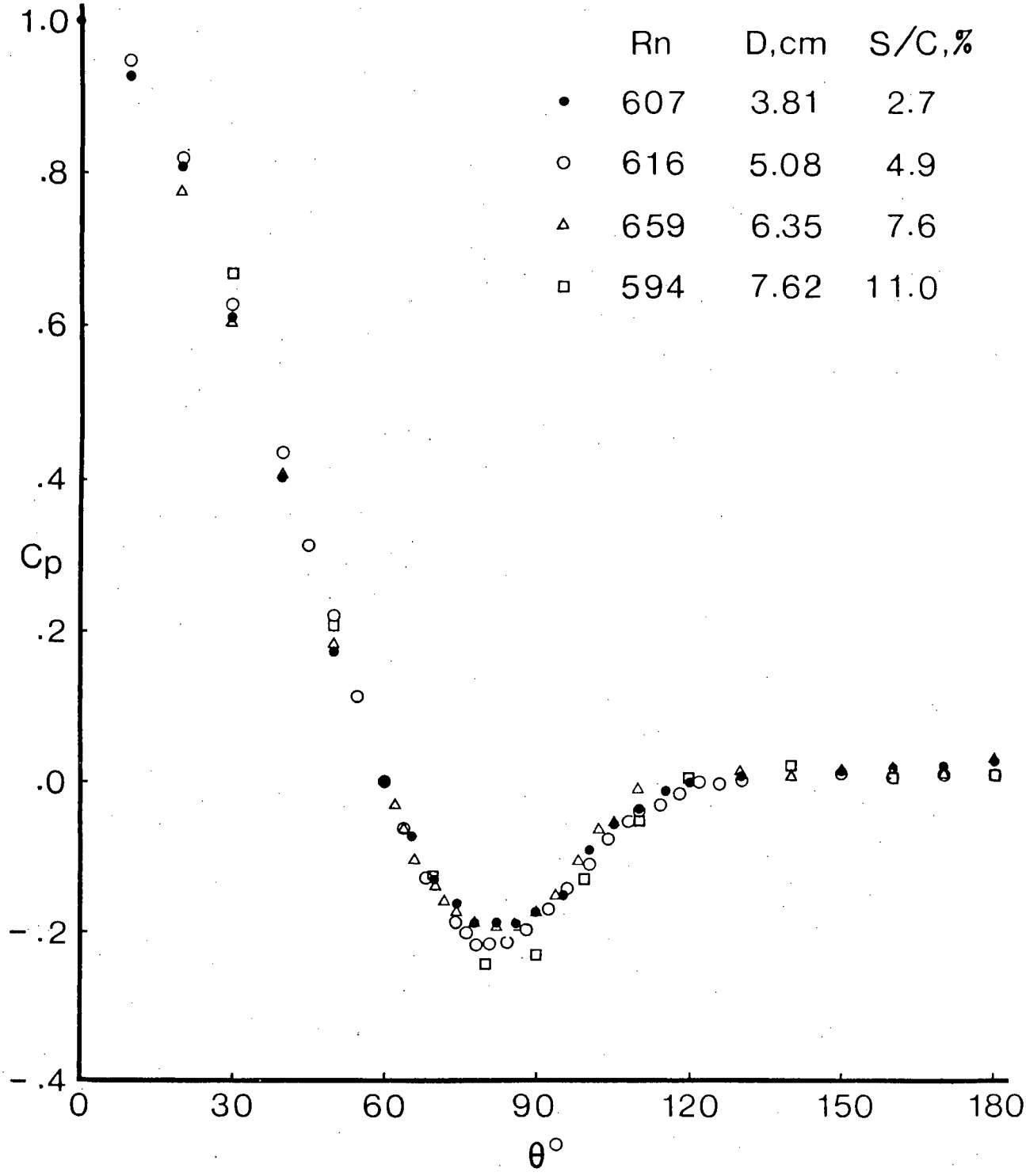

Figure 3-10 Representative plots showing negligible effect of wall confinement for blockage ratios up to 11%

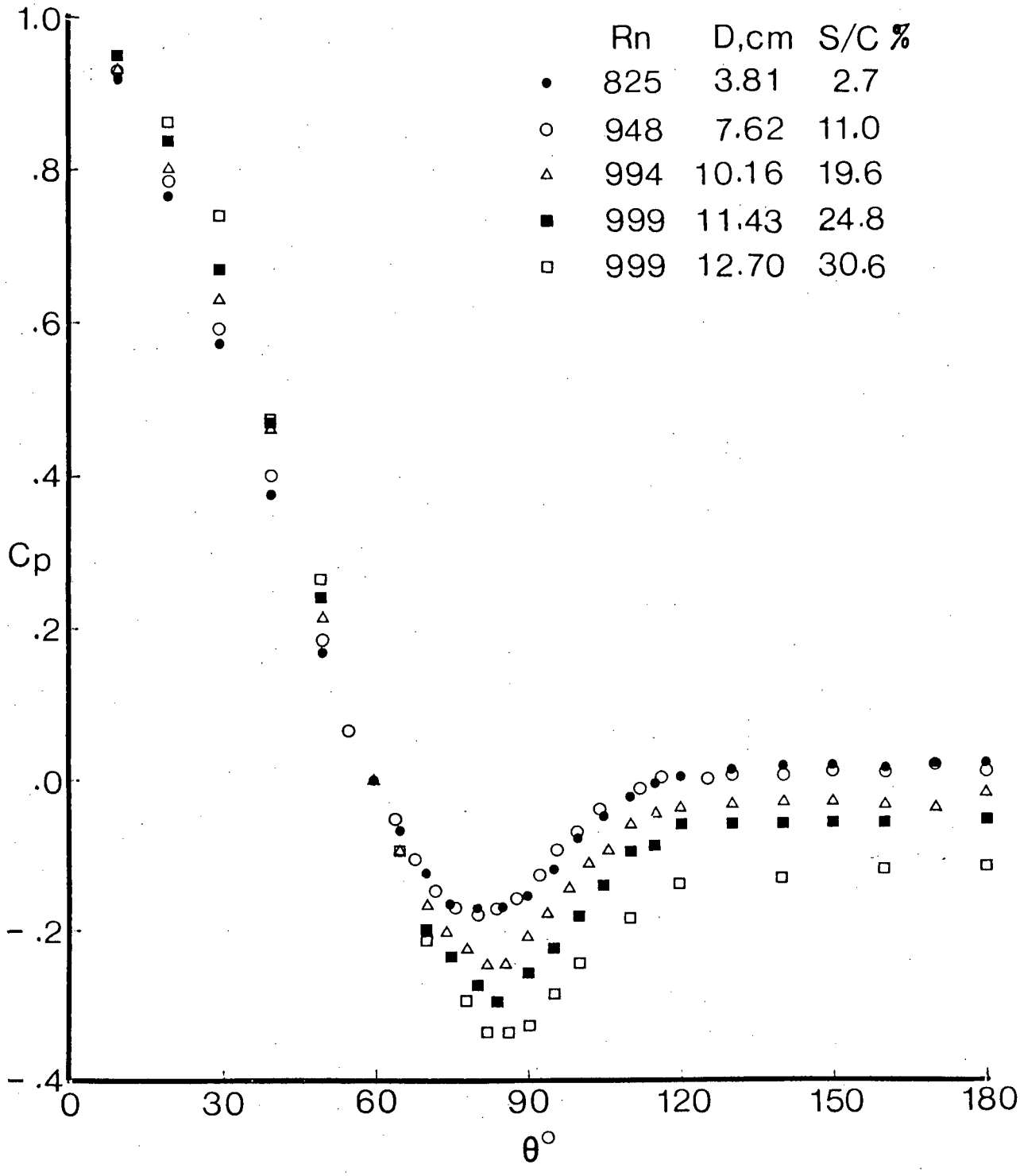

Figure 3-11 Pressure plots as affected by higher blockage: (a) $R_n \doteqdot 950$

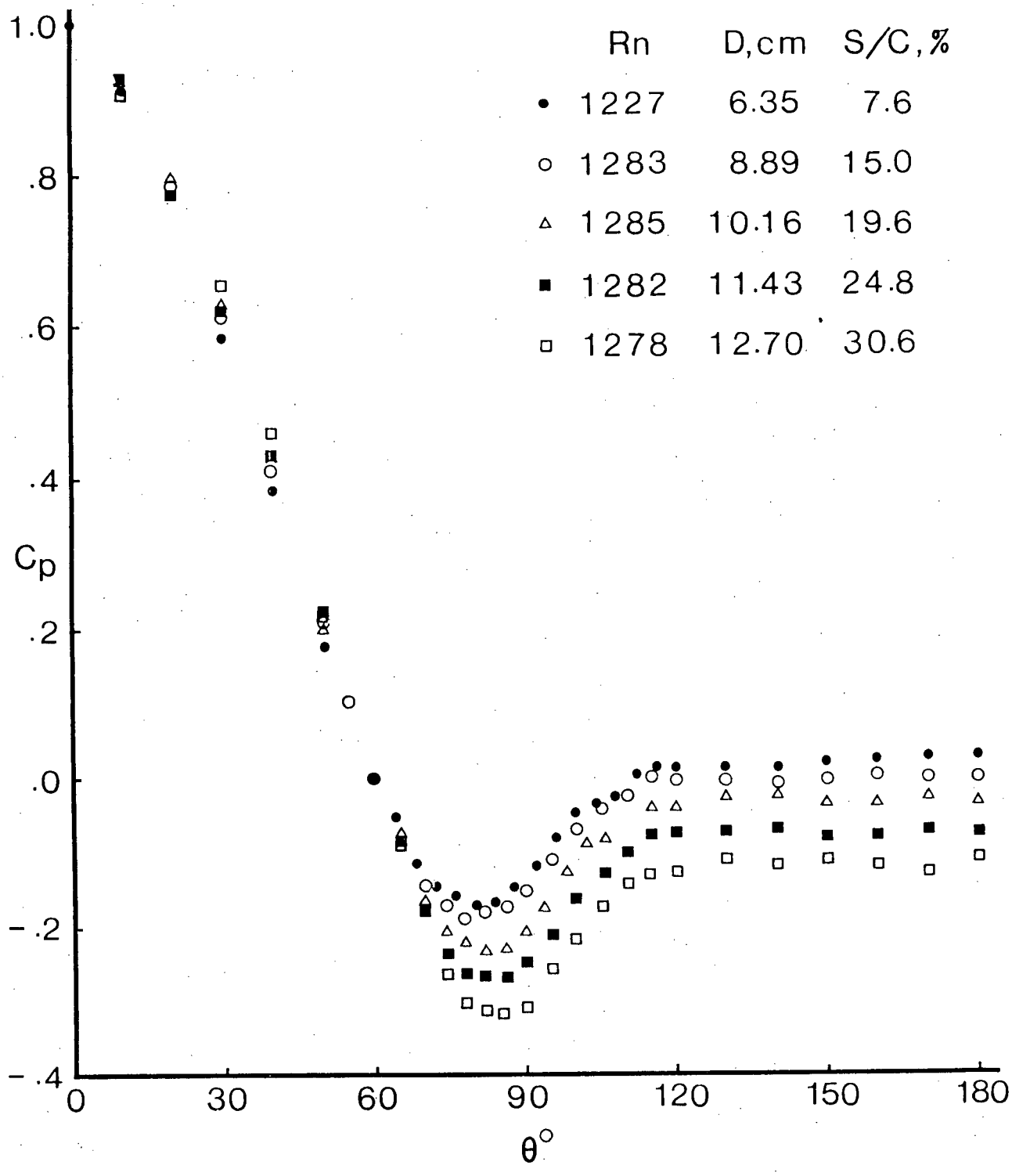

Figure 3-11 Pressure plots as affected by higher blockage: (b) $R_n \doteqdot 1250$

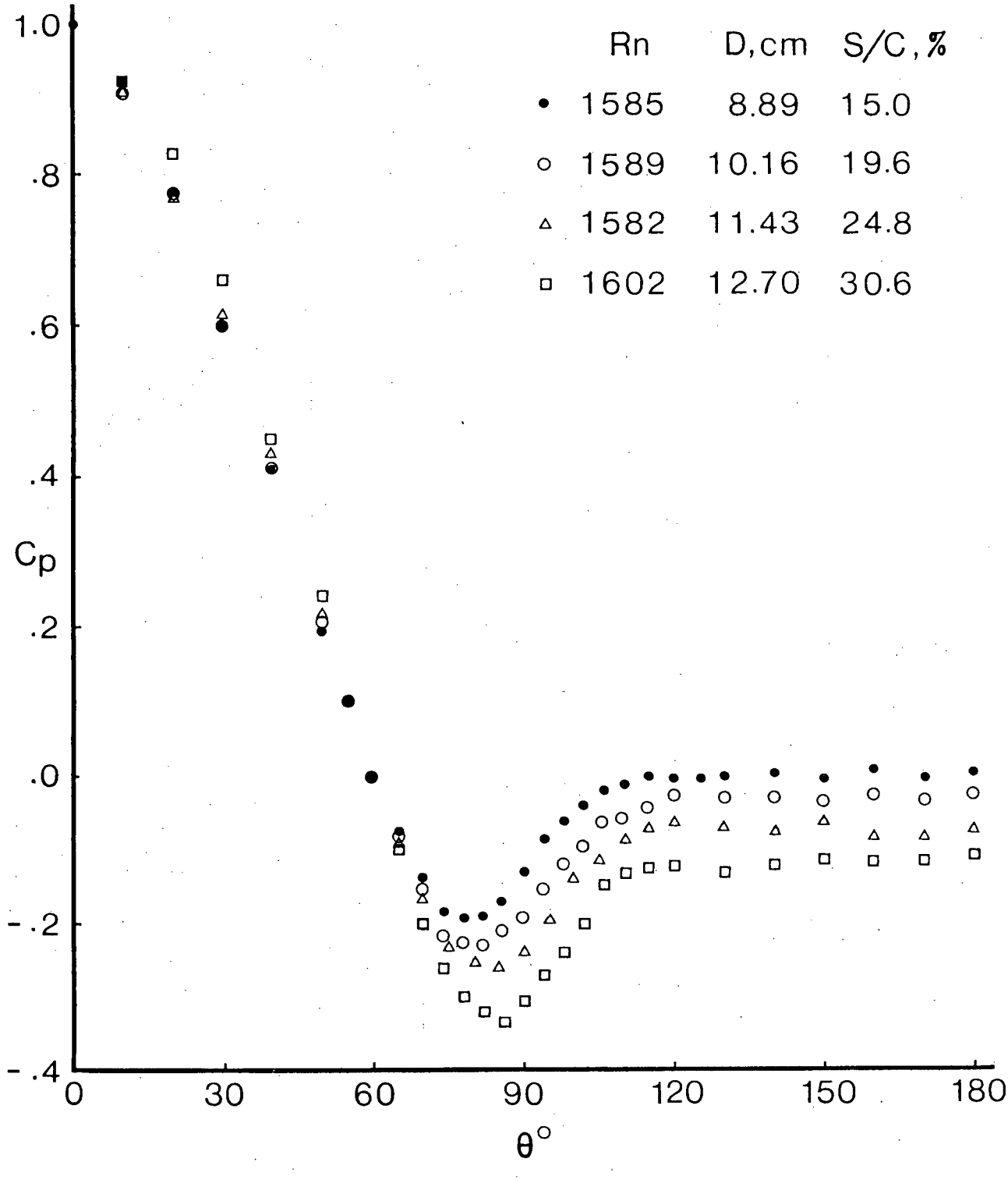

Figure 3-11 Pressure plots as affected by higher blockage: (c) $R_n \doteqdot 1600$

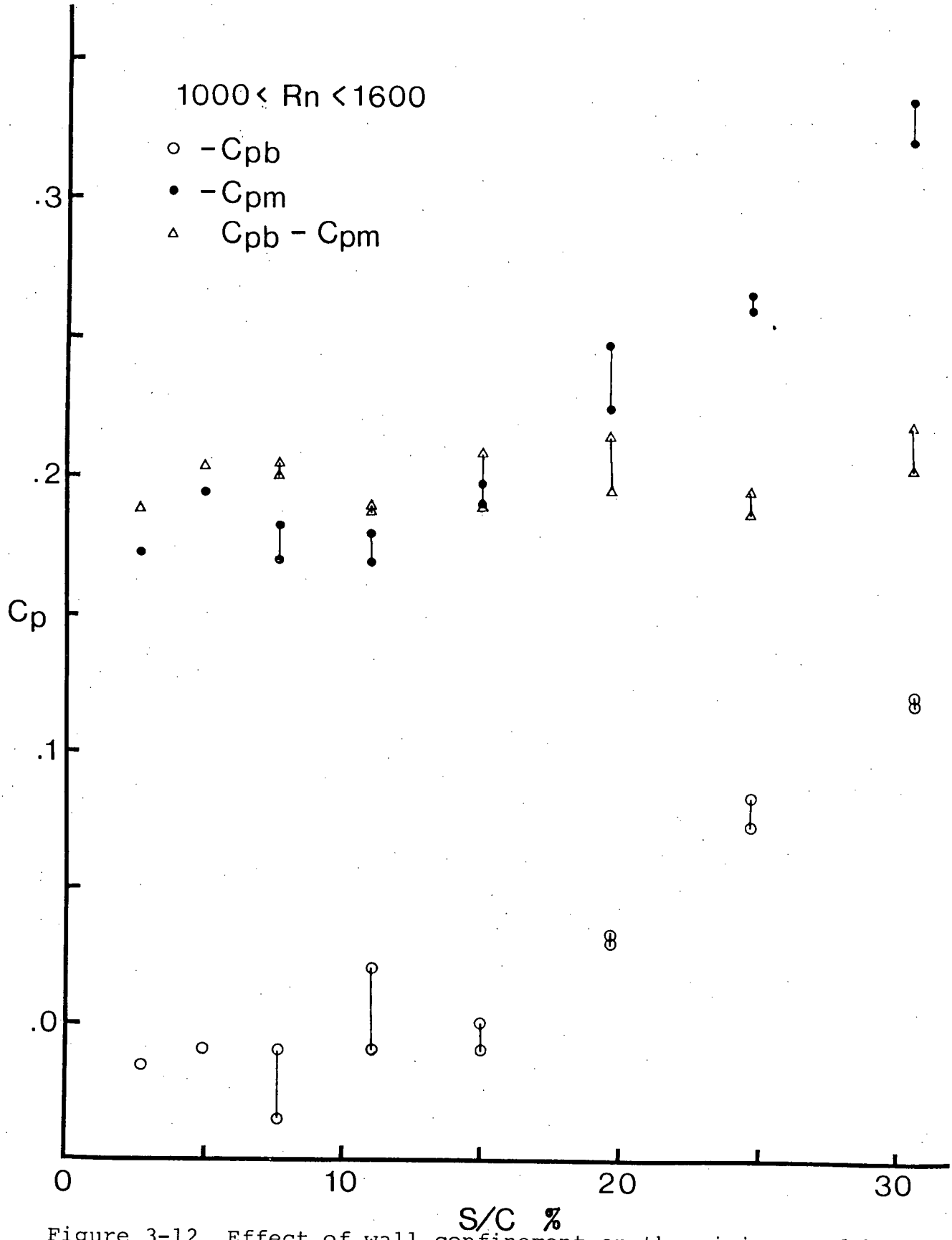

Figure 3-12 Effect of wall confinement on the minimum and base pressures, $1000 < R_n < 1600$. Note both C_{p_b} and C_{p_m} are essentially constant up to the blockage ratio of around 13%

the pressures with blockage. Thus there appears to be a critical value of the blockage ratio above which the effect of wall confinement tends to become significant. This represents information of considerable practical significance.

Interestingly the difference $C_{p_b} - C_{p_m}$, which is a measure of the pressure rise sustained by the boundary layer prior to separation, remains virtually independent of the blockage throughout. The near independence of this quantity from the confinement effects suggests relative insensivity of the boundary layer to the local changes in the free stream velocity resulting from blockage. However, at lower Reynolds number, due to dominance of viscous forces, one would expect this trend to change. Measurements conducted at $R_n = 600$ confirmed this (Figure 3-13). Although the base pressure continues to remain relatively insensitive to blockage, there is a definite drop in the minimum pressure resulting in a clear increase of $C_{p_b} - C_{p_m}$.

Useful condensation of Reynolds number and blockage effects on base pressure is presented in Figure 3-14. The results suggest that Reynolds number effects are confined to the range $R_n < 1000$ for all blockage ratios and $R_n > 1600$ for the higher blockage (S/C of 30.6% in the present case).

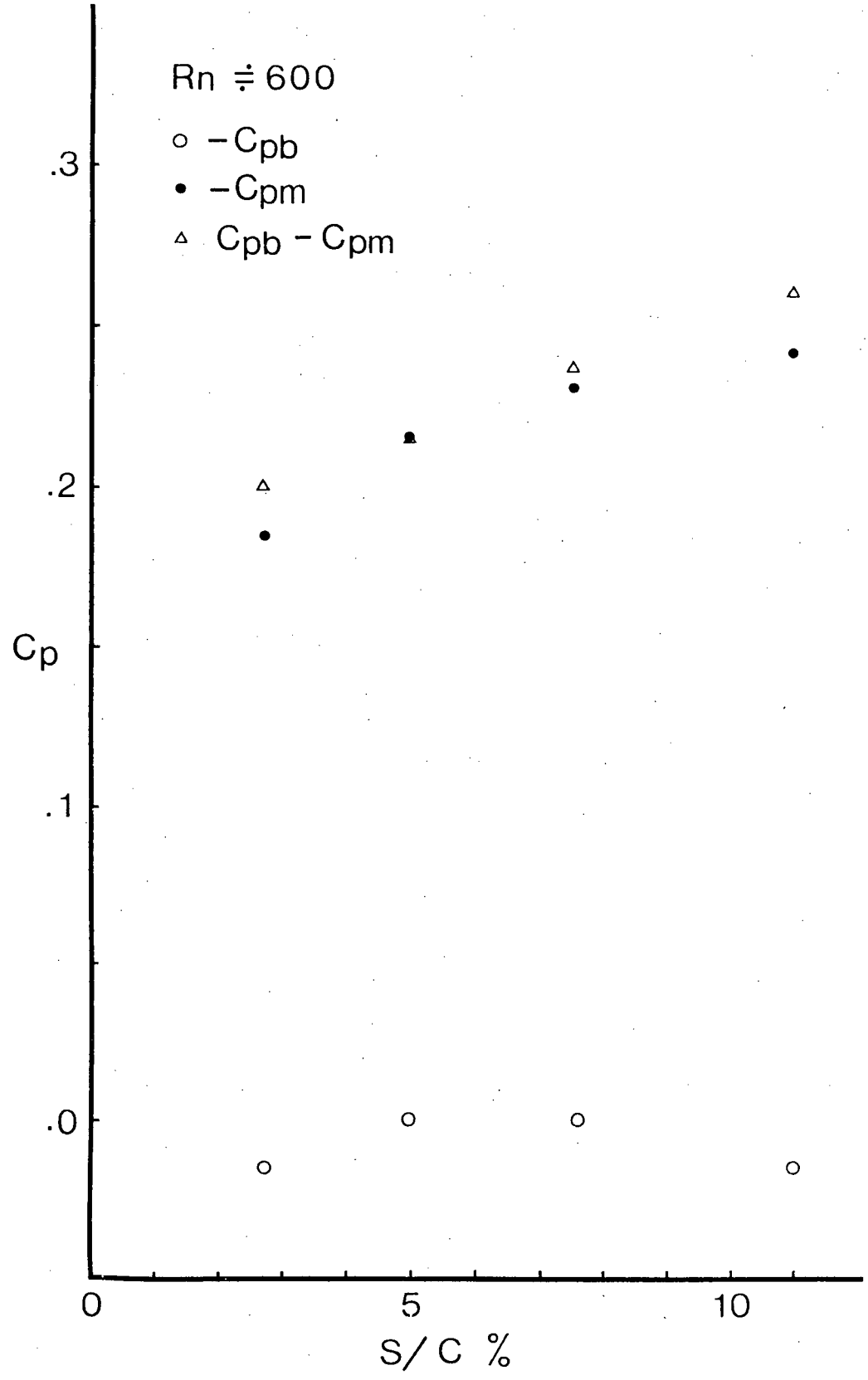

Figure 3-13 Plots showing dependence of C_{p_m} (and hence $C_{p_b} - C_{p_m}$) on wall confinement, even when S/C is less than 13%, at $R_n < 1000$

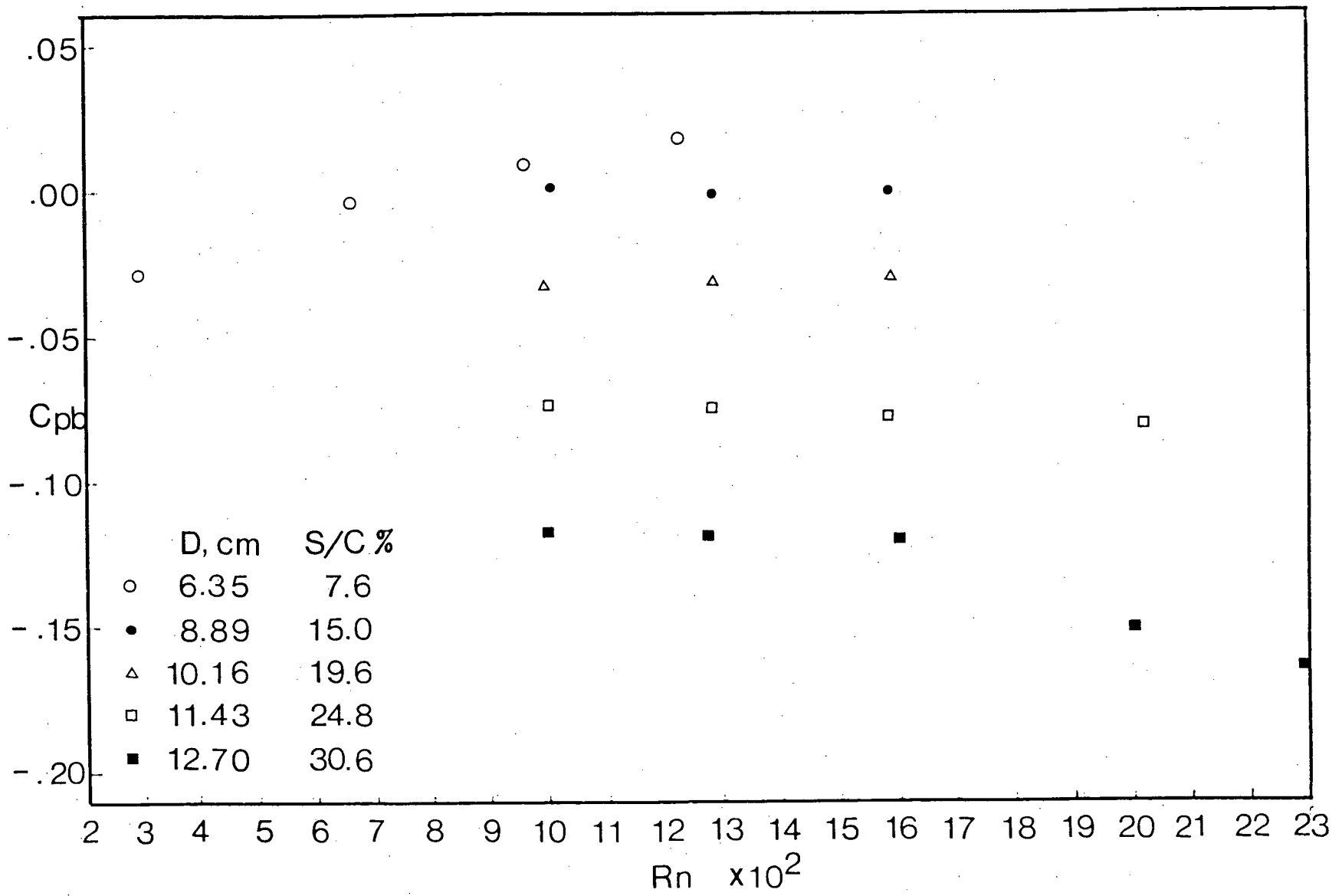

Figure 3-14 Condensation of the base pressure data showing the influence of Reynolds number and blockage

3.4 Drag Coefficient

Pressure distribution on the surface of a sphere having been established, the next logical step was to obtain the pressure integrated value of drag and assess its dependence on blockage. This, of course, cannot account for the skin friction contribution. On the other hand, the direct measurement of skin friction is confined to the high Reynolds number range of 5×10^4 - 6×10^6, by Achenbach[9]. The corresponding information at lower Reynolds number ($R_n < 5 \times 10^4$) is totally missing. With this as background, it was decided to undertake measurement of the total drag using a strain gage balance described in Section 2.5. The information proved useful in checking available results by other investigators (in absence of blockage). It also helped establish the influence of wall confinement on the total as well as the skin friction drag components and their comparison with several empirical relations found in literature.

One would expect the drag coefficient to be primarily governed by magnitude and location of the minimum pressure point, the pressure distribution downstream of it, as well as the skin friction contribution. Since the pressure profiles do not change beyond $R_n = 1000$, the pressure drag coefficient for a

given blockage is expected to remain essentially constant (Figure 3-15a). However, the total drag would show a drop with an increase in Reynolds number. This is precisely the trend shown in Figure 3-15(b). As can be expected, the effect of blockage is to increase the drag coefficient because of local increase in the free stream velocity. Note, a change in blockage by approximately 30% changes the drag coefficient by more than 100%. It would be useful to point out that both the drag coefficient and Reynolds number are based here on the average velocity in the test section.

For comparison with available results, plots in Figure 3-16 are ideal being based on measured values of the total drag and reduced using the centerline velocity. This is because most of the results recorded in literature are obtained using spheres either towed or in free fall condition. The figure shows present experimental data together with the standard drag curve results by Sivier[3], Zarin[4], Ross and Willmarth[5], and the empirical relation suggested by White[60]. It was heartening to note a rather excellent correlation of the present results at smaller blockage thus substantiating their accuracy.

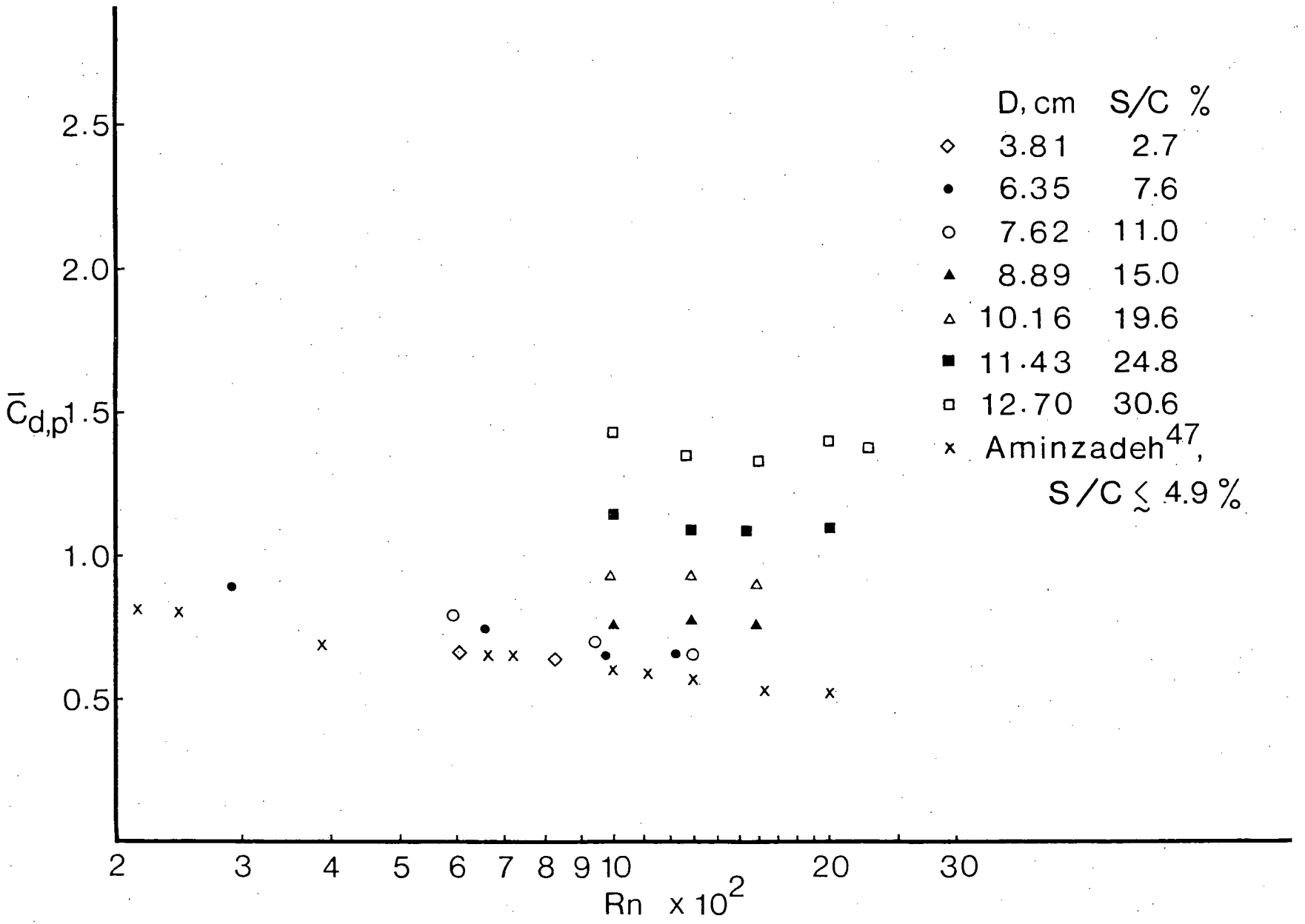

Figure 3-15 Variation of the measured drag coefficient with Reynolds number and blockage: (a) pressure drag coefficient

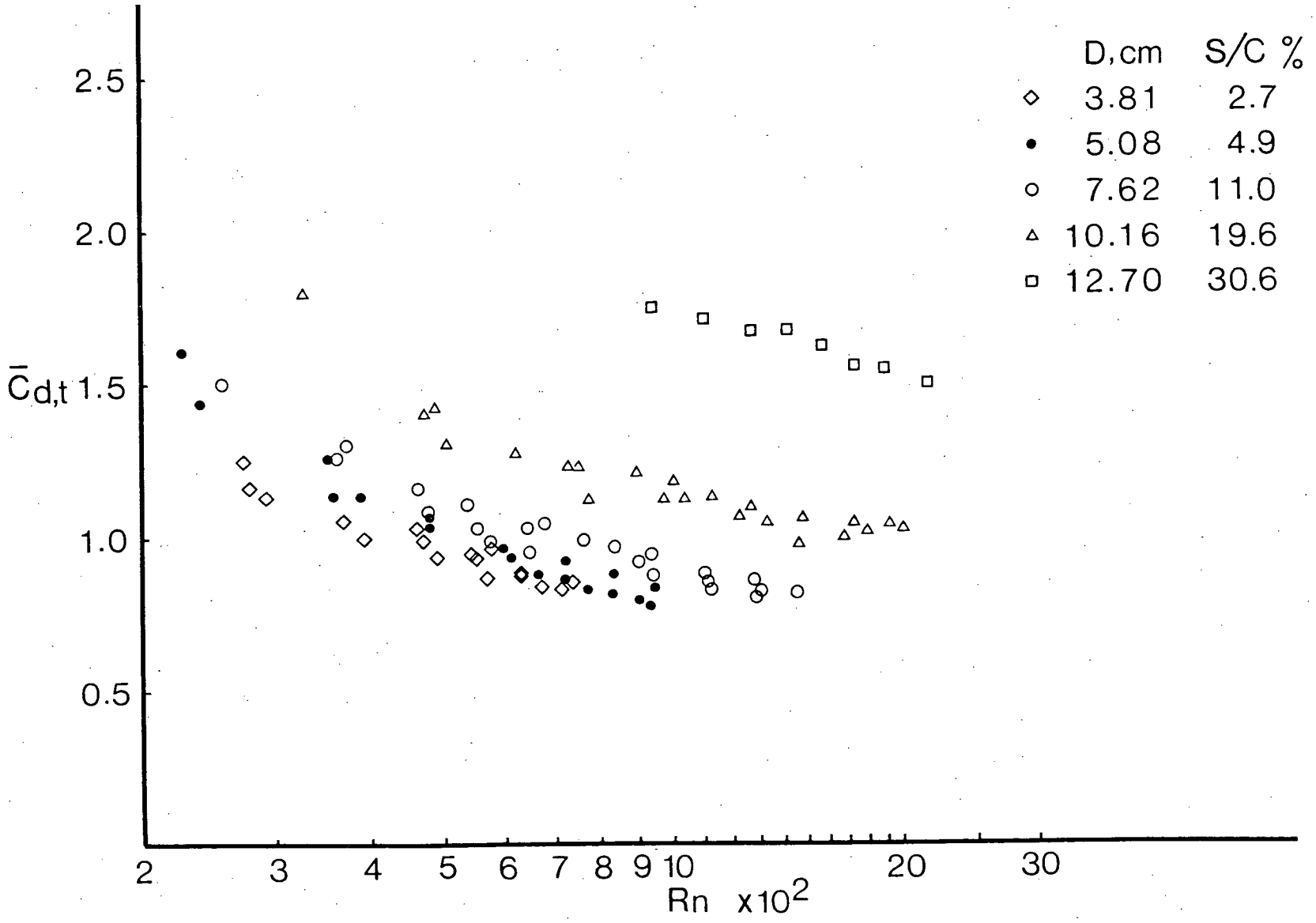

Figure 3-15 Variation of the measured drag coefficient with Reynolds number and blockage: (b) total drag coefficient. The drag coefficient is based on average velocity in the test-section

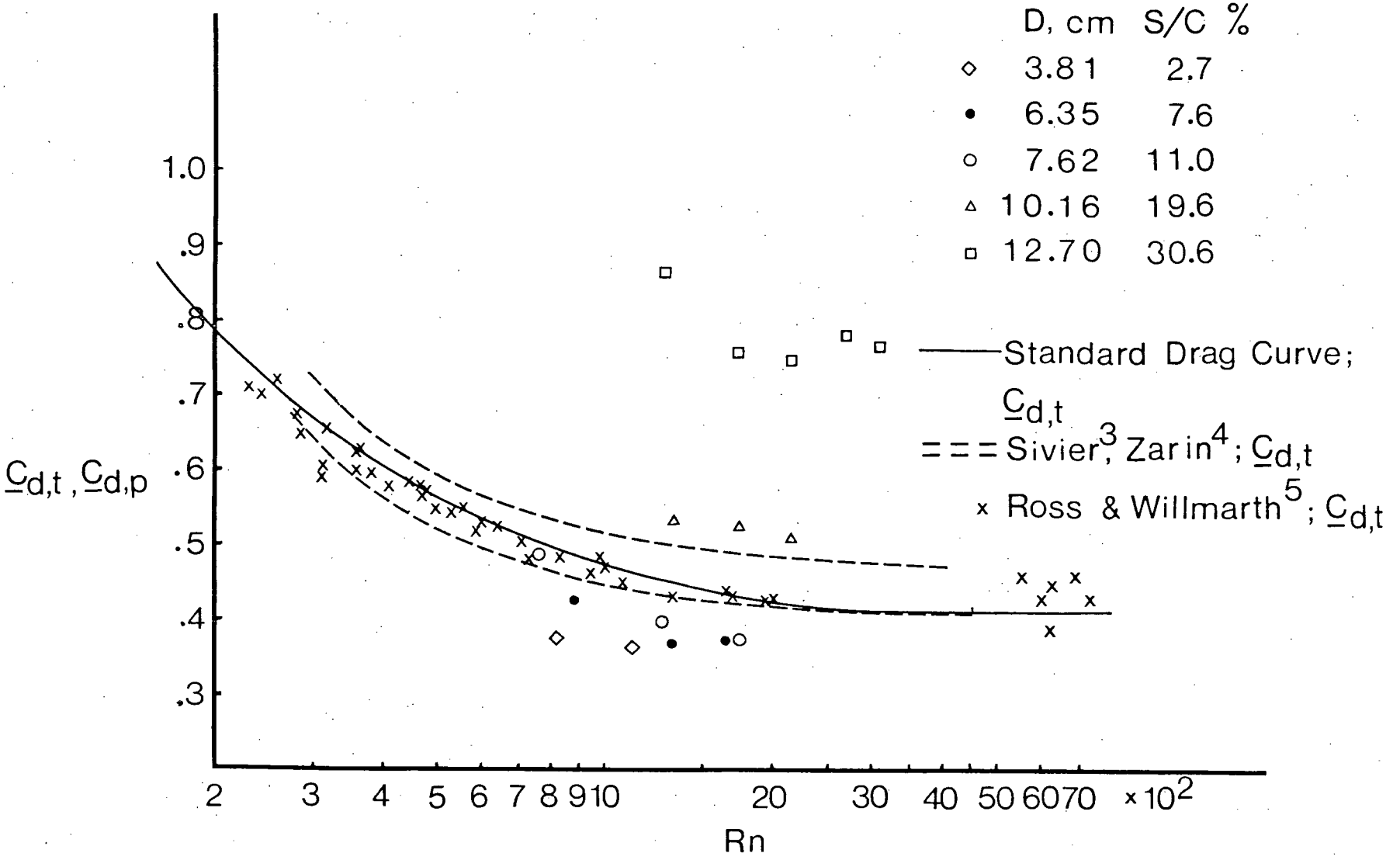

Figure 3-16 Comparison of the pressure and total drag coefficients with the standard drag curve and recent data reported in literature. Note the results are based on the centerline velocity: (a) pressure drag coefficient

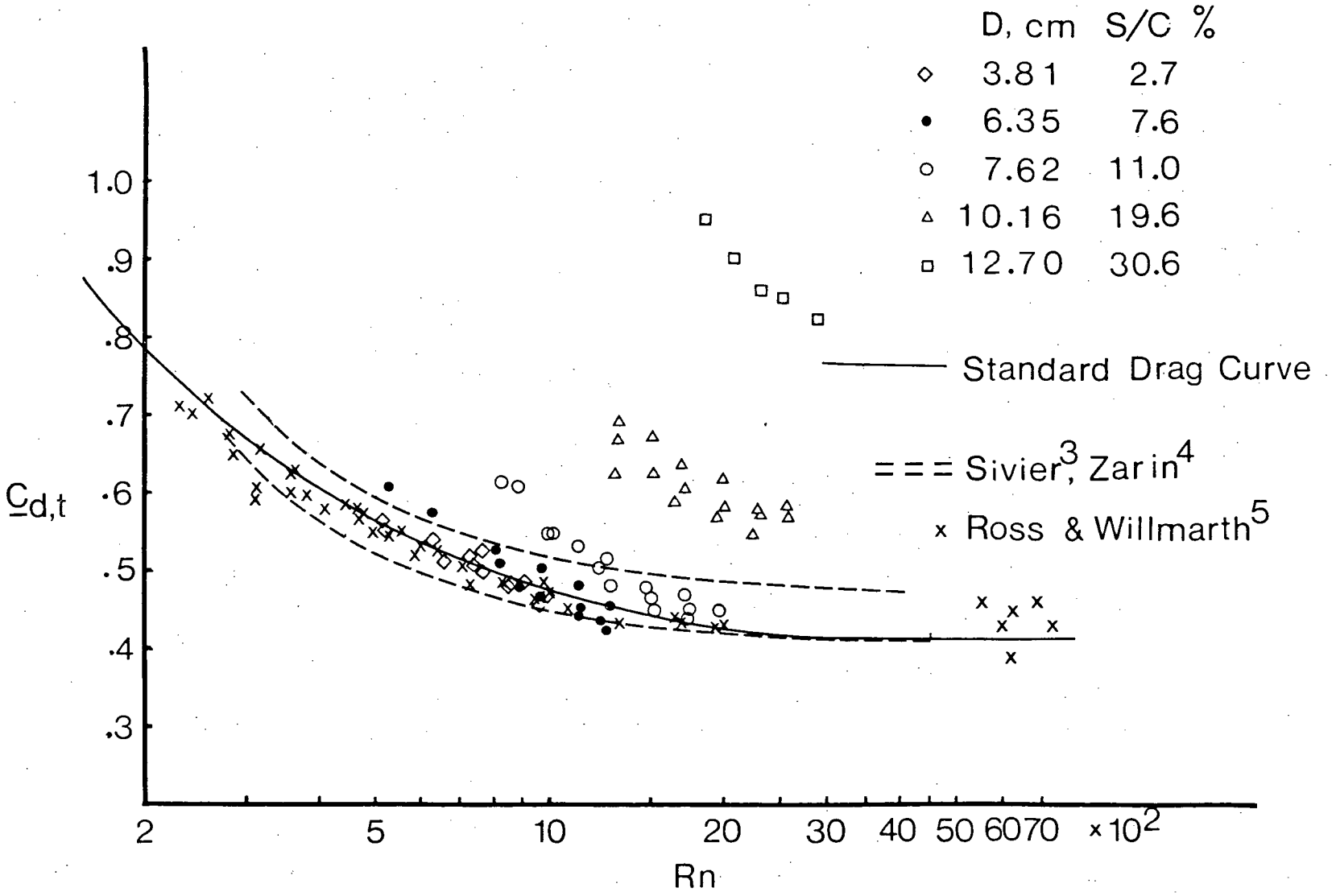

Figure 3-16 Comparison of the pressure and total drag coefficients with the standard drag curve and recent data reported in literature. Note the results are based on the centerline velocity: (b) total drag coefficient

With pressure and total drag information at hand it was convenient to plot variation of skin friction with Reynolds number and blockage. Corresponding results by Achenbach[9](unconfined flow) near critical end of the Reynolds number range and empirical relations as suggested by Rosenhead[61] and White[60] are also included for comparison (Figure 3-17). The results tend to confirm the classical dependence of skin friction on the Reynolds number, $C_{d,f} \propto R_n^{-1/2}$, however, the information is not extensive enough to establish any well defined trend for the blockage effect. Achenbach's results near the critical Reynolds number and the present data in a relatively lower Reynolds number range can be fitted quite well along the line

$$\frac{C_{d,f}}{C_{d,t}} = 6.08\ R_n^{-0.5} ,$$

which corresponds to $C_{d,f} = 2.432/(R_n^{0.5} - 6.08)$ and $C_{d,p} = 0.4$. On the other hand, White and Rosenhead's predictions show considerable discrepancy which tends to increase with an increase in the Reynolds number.

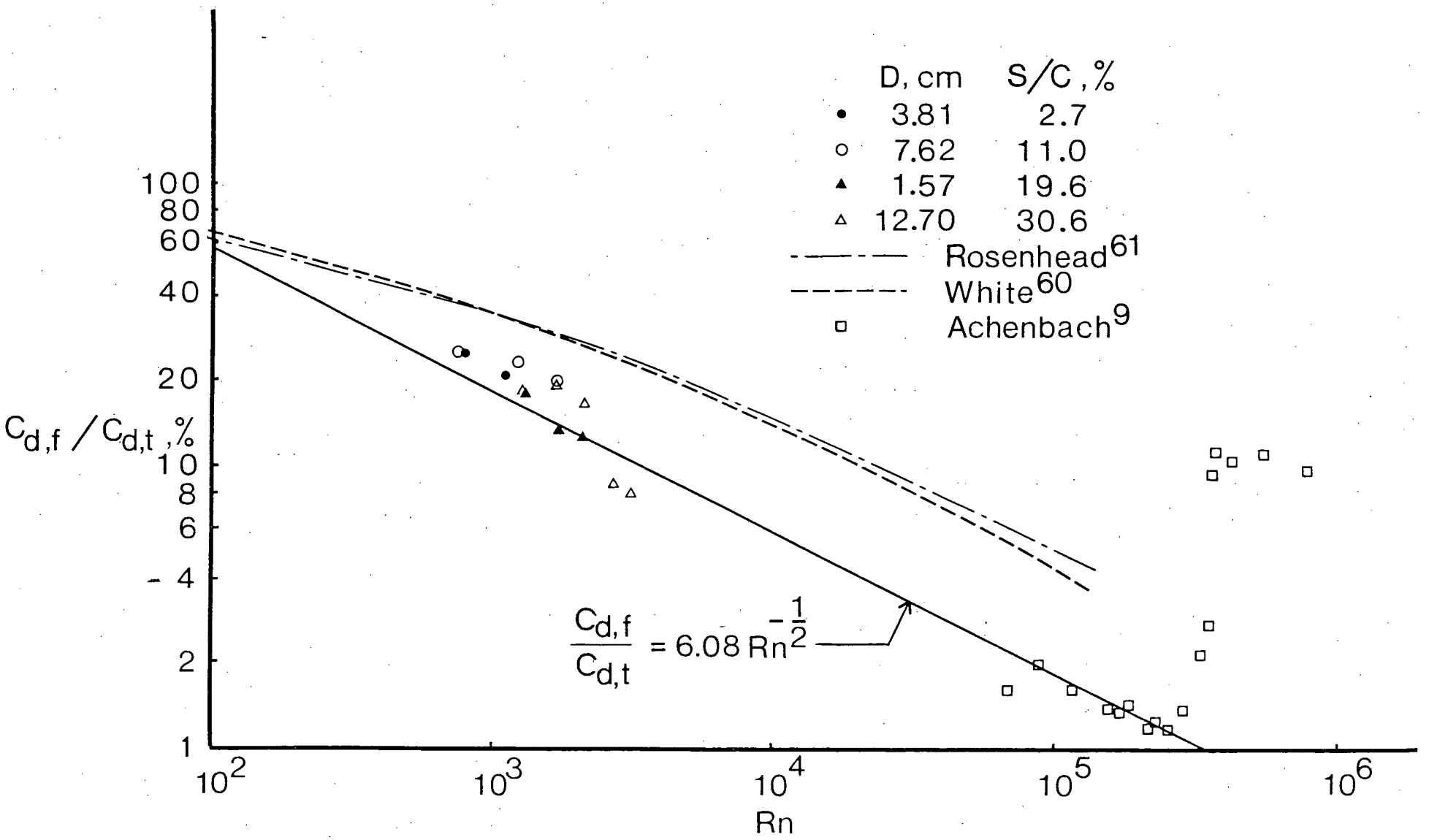

Figure 3-17 Friction force as a percentage of the total drag

3.5 Blockage Correction Using Maskell's Theory

Maskell developed a theory for blockage correction based on momentum balance between the undisturbed flow upstream of the body and that downstream where effective wake reaches its maximum width, B. For a square plate normal to the flow, and assuming pressure in the wake to be uniform and equal to the base pressure, P_b, the drag coefficient is given by

$$C_d = m\,[K^2 - (1 - m\,S/C)^{-1}]$$

where m = B/S. Here K represents ratio of the velocity on separating streamline to the free stream velocity. By hypothesis, he derived an expression for the effect of blockage on the wake width as

$$\frac{m}{m_c} = 1 - \frac{C_d - C_{d_c}}{(K^2 - 1)(K_c^2 - 1)}\left(\frac{S}{C}\right)$$

where the subscript c stands for corrected values. This gives the correction formula as

$$\frac{K^2}{K_c^2} = 1 + \frac{C_d}{K_c^2 - 1}\frac{S}{C} + o\left[\left(\frac{S}{C}\right)^2\right]$$

where the terms of order $(S/C)^2$ were considered negligibly small. With this the correction for drag and pressure

coefficients are directly given by

$$\frac{1 - C_p}{1 - C_{p_c}} = \frac{C_d}{C_{d_c}} = \frac{K^2}{K_c^2} = \frac{q_c}{q} \quad .$$

It should be mentioned here that the theory considers invariance of the separation point under constraint, hence Maskell doubted its applicability to well-rounded bodies. However, the correction procedure has been quite popular with industrial aerodynamicists, who have applied it to situations totally unrelated with that considered in the theory. It was decided to assess validity of Maskell's correction procedure in the present case.

Figure 3-18 shows variation of pressure integrated as well as total measured drag as functions of blockage at $R_n \simeq 1000$. The corrected values using Maskell's approach are also presented. It is apparent that this correction procedure is quite inadequate particularly at higher blockage ratios. The error was found to vary from 8% to 84% over the blockage ratio range of 7.6 - 30.6%.

Correction relations for total and pressure drag coefficients are summarized in Figure 3-19. For the convenience of application, the relations are specified in terms of average as well as centerline velocities.

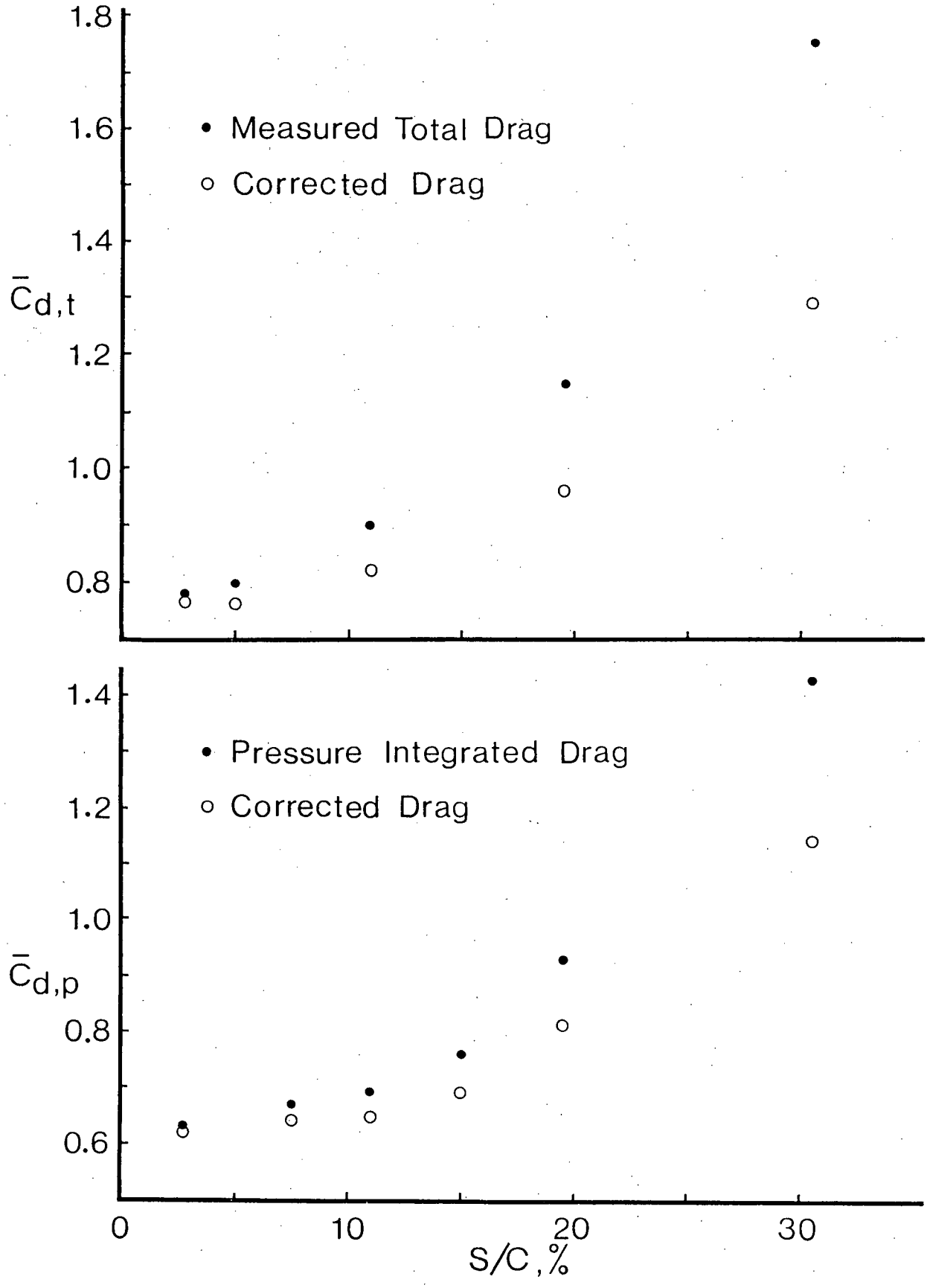

Figure 3-18 Corrected drag coefficients showing inadequacy of Maskell's procedure, particularly at higher blockage

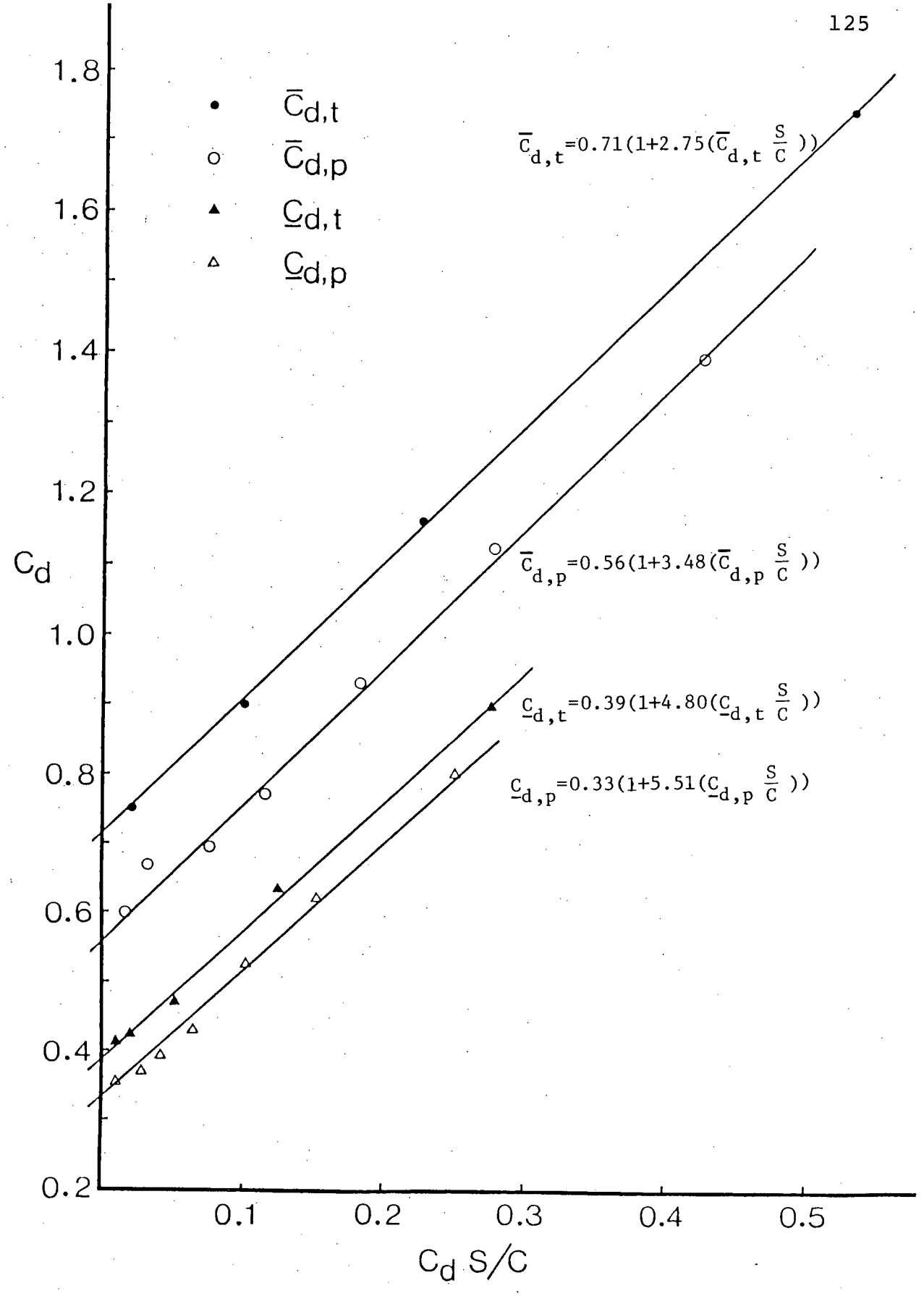

Figure 3-19 Empirical correction formulae for sphere drag

3.6 Flow Visualization and Near-Wake Analysis

To provide better appreciation as well as substantiation of the certain behaviour exhibited by the measured data, it was decided to undertake extensive flow visualization program. A set of spheres ranging in diameter from 0.95 - 12.7 cm were used in the glycerol-water solution of 54% concentration by weight. The main objective was to observe the formation, development and instability of the vortex ring and the associated influence on the measured pressure data. It was also hoped that this would provide some indication concerning location of the separation position and its movement. The use of dye injection procedure, explained in detail earlier, proved to be quite effective in achieving these objectives. It showed formation of the vortex ring in a rather spectacular fashion as presented in Figure 3-20. Numerous photographs were taken at systematic increments of the Reynolds number. Only a few of the typical pictures illustrating formation, symmetric elongation, onset of asymmetry and instability followed by turbulent shedding are presented in Figure 3-21.

The existence of an axisymmetric, stable vortex ring for low Reynolds number in a stream,

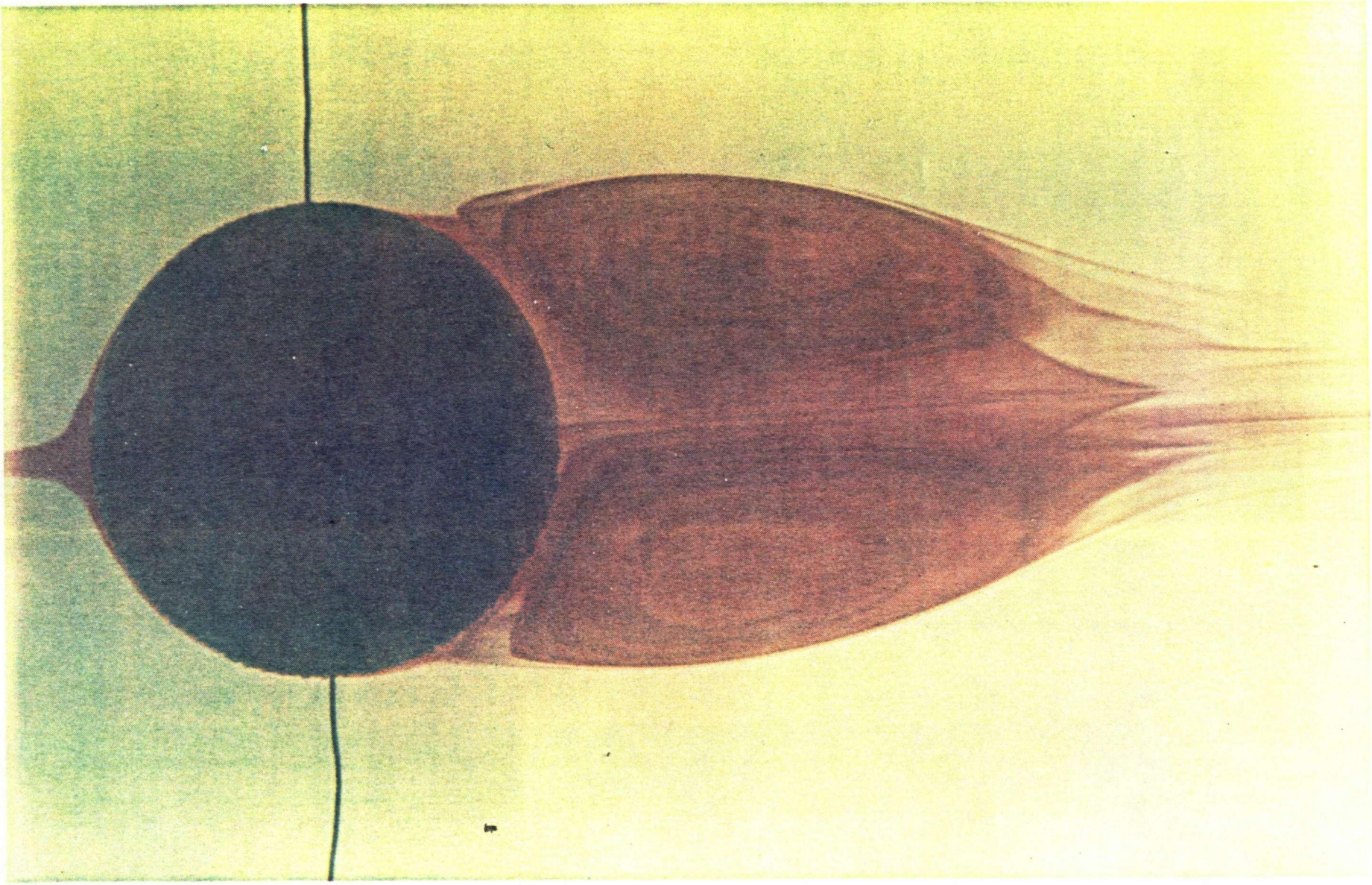

Figure 3-20 A typical photograph illustrating formation of a vortex ring behind a sphere

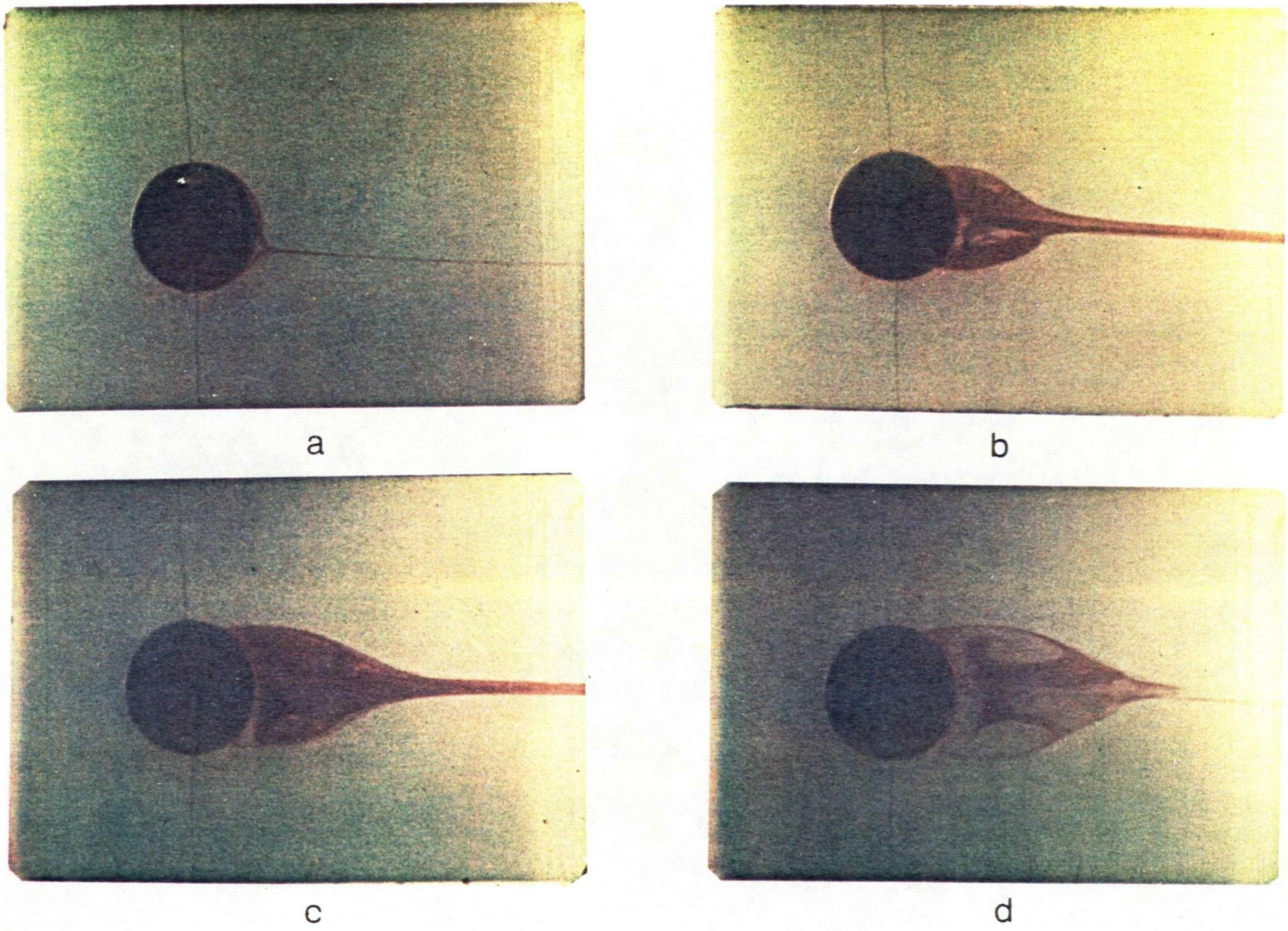

Figure 3-21 A flow visualization study showing development and instability of vortex ring with Reynolds number: (a) R_n=30; (b) R_n=65; (c) R_n=115; (d) R_n=165

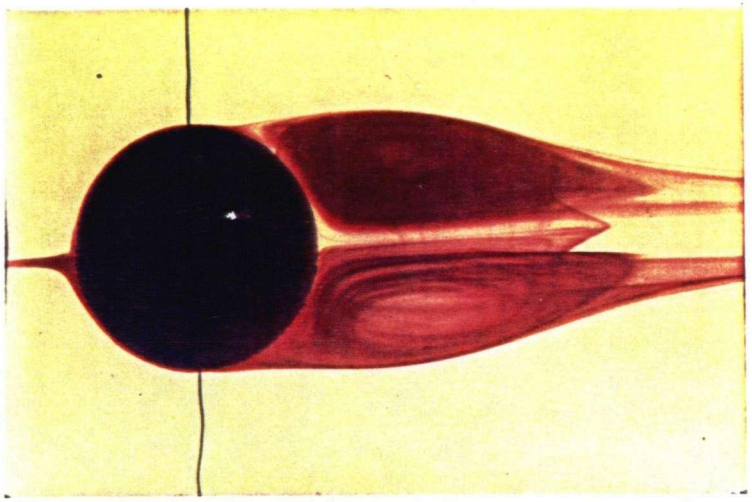

e

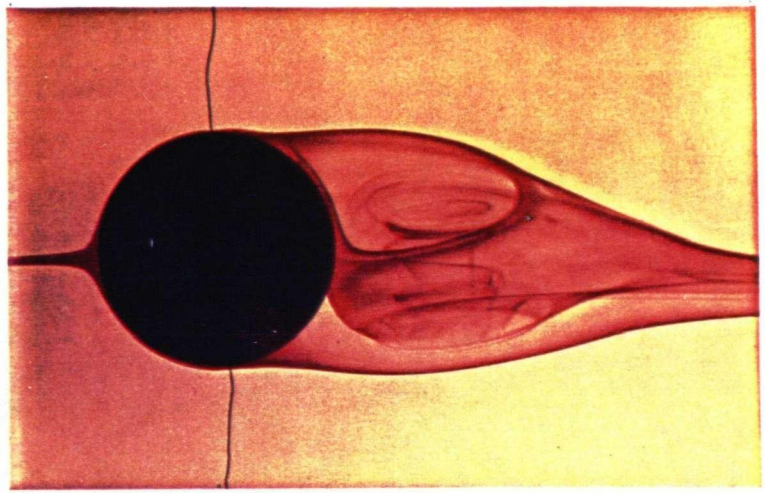

f

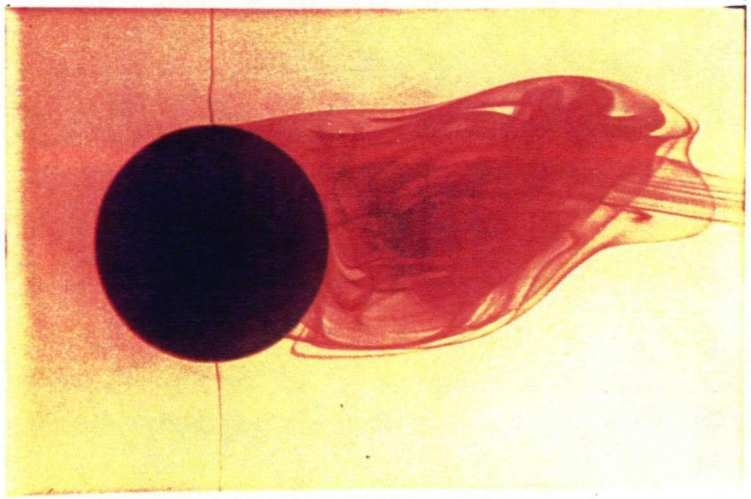

g

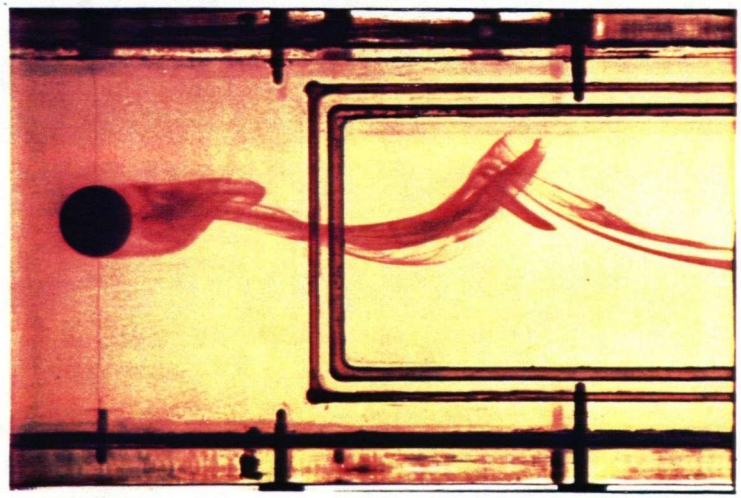

h

Figure 3-21 A flow visualization study showing development and instability of vortex ring with Reynolds number: (e) R_n=221; (f) R_n=265; (g) R_n=280; (h) R_n=280

essentially free of macroscopic turbulence is shown in Figures 3-21(a) to 3-21(e). For the Reynolds number above a critical value (corresponding to the first formation of a stable ring, $R_n \simeq 24$), the streamlines separate from the surface and form a closed region immediately behind the sphere. A single stream emerges from the vertex of the closed region extending to a long distance behind the sphere. The size of the ring is such as to maintain an equilibrium between the rate at which vorticity is generated and dissipated into the main stream. As the Reynolds number is increased the vortex ring becomes elongated in the flow direction to maintain this equilibrium, and the separation points move upstream towards the front stagnation point (Figure 3-21). This forward movement of the separation points was also suggested by the pressure plots presented earlier (Figure 3-7).

For Reynolds number between 170 - 230 an asymmetry in the circulatory motion within the vortex sheet produces a corresponding asymmetry in the circulatory motion in the ring itself and a resultant shift from the centerline.

The state of unsymmetrical but steady wake is disturbed by further increase in the Reynolds number. The rate at which vorticity is diffused from the sheet into

the main body of the fluid remains practically constant, but the increased rate at which it is transferred to the vortex ring creates unstable condition within the vortex sheet. Basically, the process is one of build-up and release, but no sizeable portion of the ring escapes through an opening in the end of the vortex sheet during the cycle. This in turn causes the oscillation of the asymmetrical wake about the axis of symmetry. When the vortex strength of the ring reaches a critical value, a sudden motion of the ring disturbs the sheet, which in turn is responsible for a release of vorticity and a consequent return of the ring to its original position and shape. This phenomenon appears to occur in the Reynolds number range of about 250 - 300 (Figures 3-21f-h).

With further increase in the Reynolds number, the oscillatory motion of the vortex ring assumes higher frequency and the circulation within the sheet ceases to be symmetrical. In the cycle of build-up and release, the vorticity generated in the boundary layer becomes concentrated on diametrically opposite sides of the flow axis within the vortex sheet. The sections in which the vortex strength is the greatest are alternately discharged into the main body of the fluid. With each ejection a portion of the sheet is carried away. The

vortex element discharged into the stream interacts with the dispersed liquid to form a regular wake pattern. Figures 3-22 shows a typical cycle of initiation, development and shedding of the ring vortex.

As mentioned before, the flow visualization results provide useful information concerning location of the separating shear layer. To this end the photographs were analyzed systematically and the separation position plotted as a function of R_n as shown in Figure 3-23. Note that the separation point moves forward by as much as 20° for blockage ratio of 2.7%, over the Reynolds number range of 100 - 600. For comparison, available results by other investigators are also included. Here the line attributed to Pruppacher et al.[38] represents an average value based on his own data as well as those by Jensen[35], Hamielec et al.[36] and, Rimon and Cheng[40]. The figure also shows effect of blockage on position of the separating vortex sheet. Typical photographs of the vortex ring associated with spheres offering different blockage are presented in Figure 3-24. In general, for a given Reynolds number, the wall confinement tends to move the separation position downstream. It must be emphasized that the visual determination of separation point is,

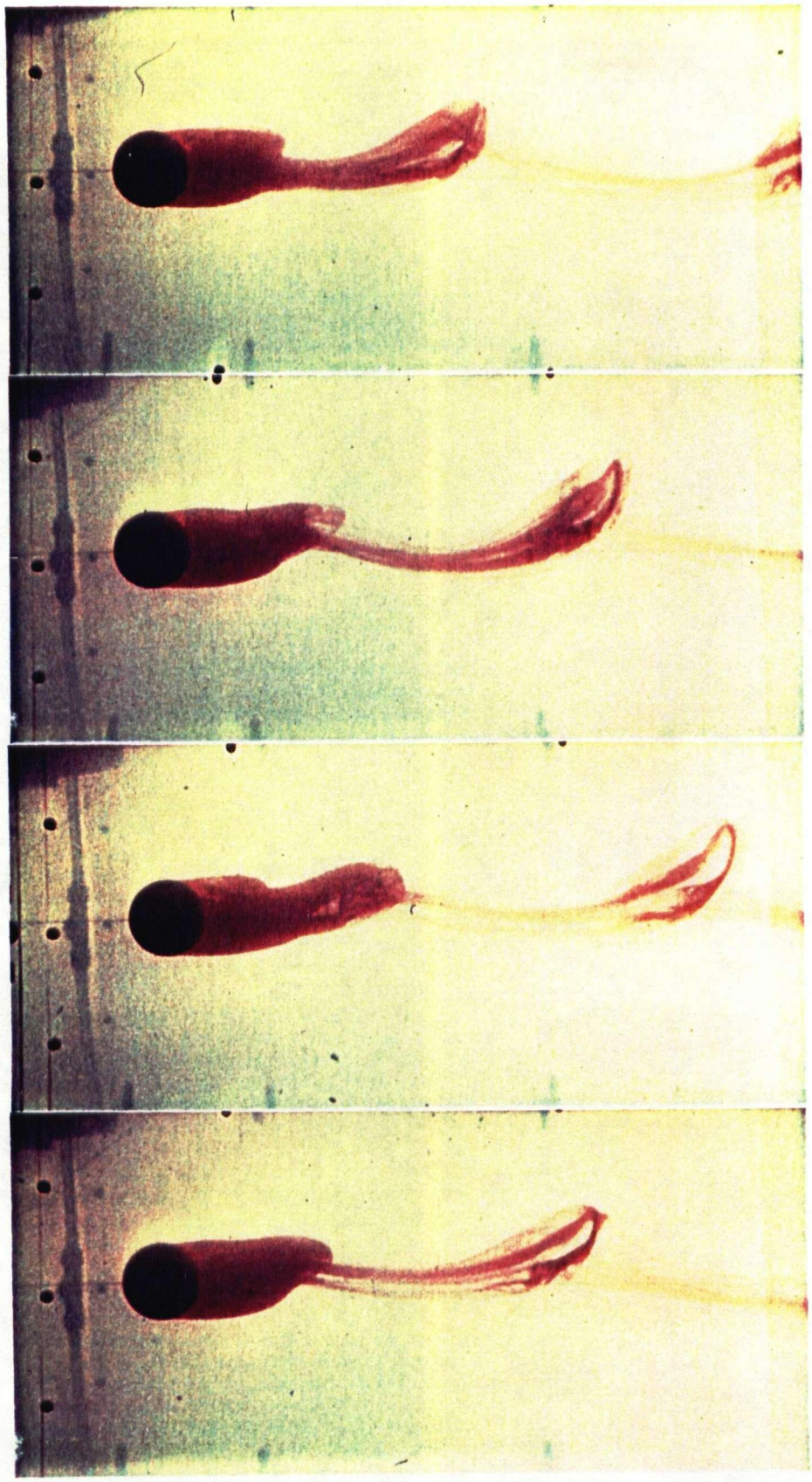

Figure 3-22 Typical cycle of initiation, development and shedding of the ring vortex at Reynolds number R_n = 360 .

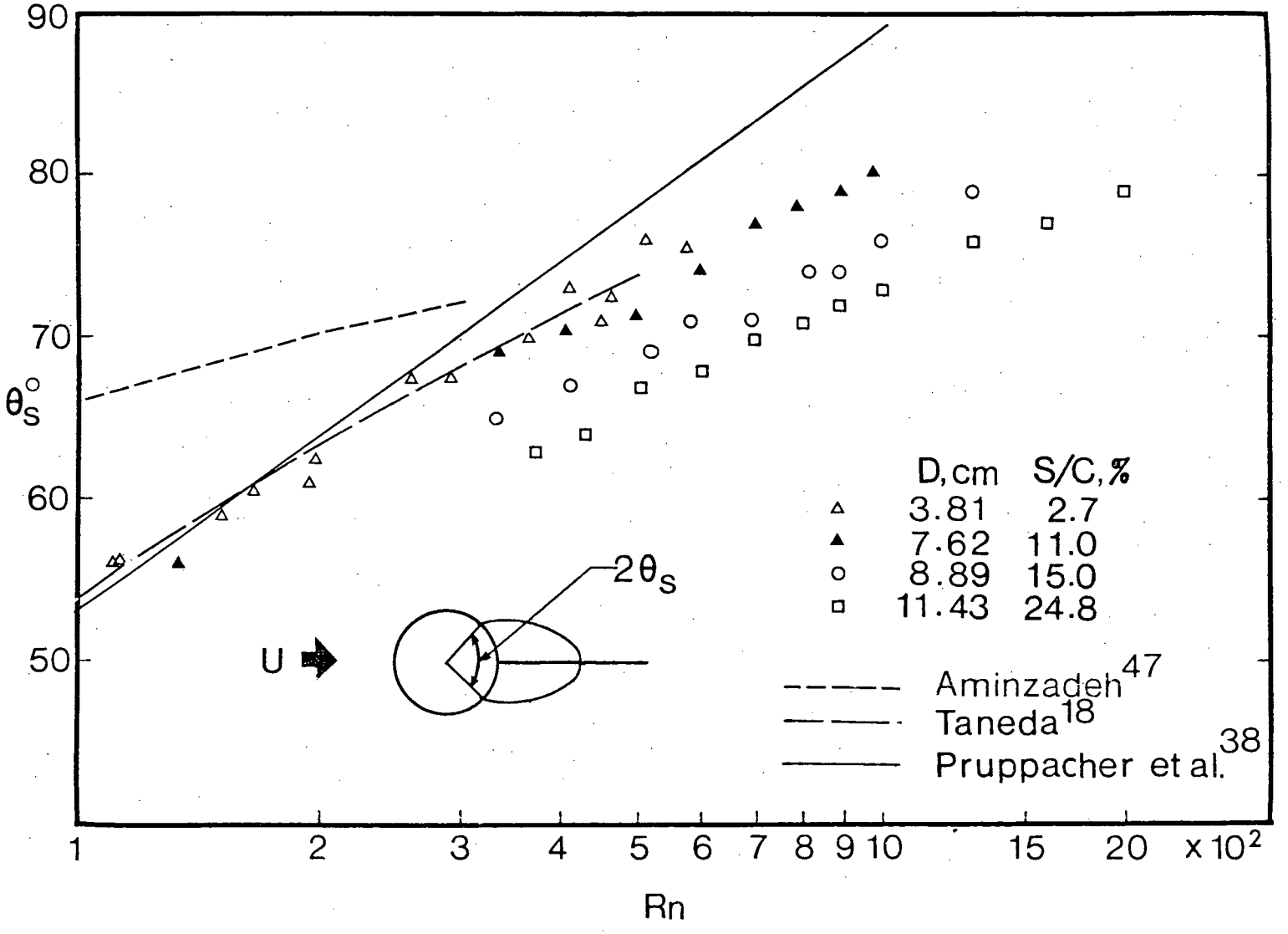

Figure 3-23 Position of separation as affected by Reynolds number and wall confinement

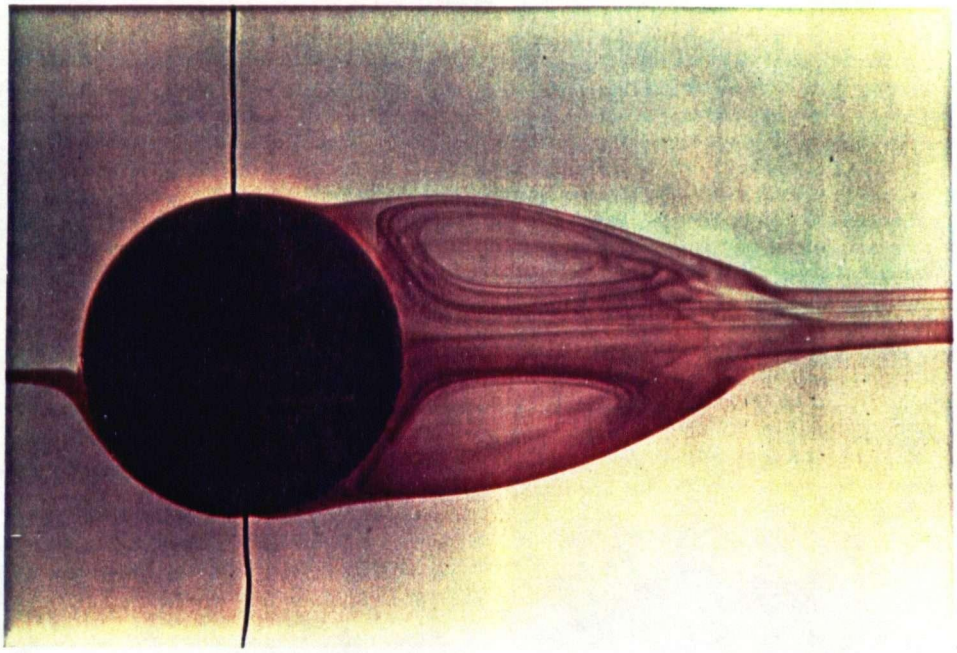

a

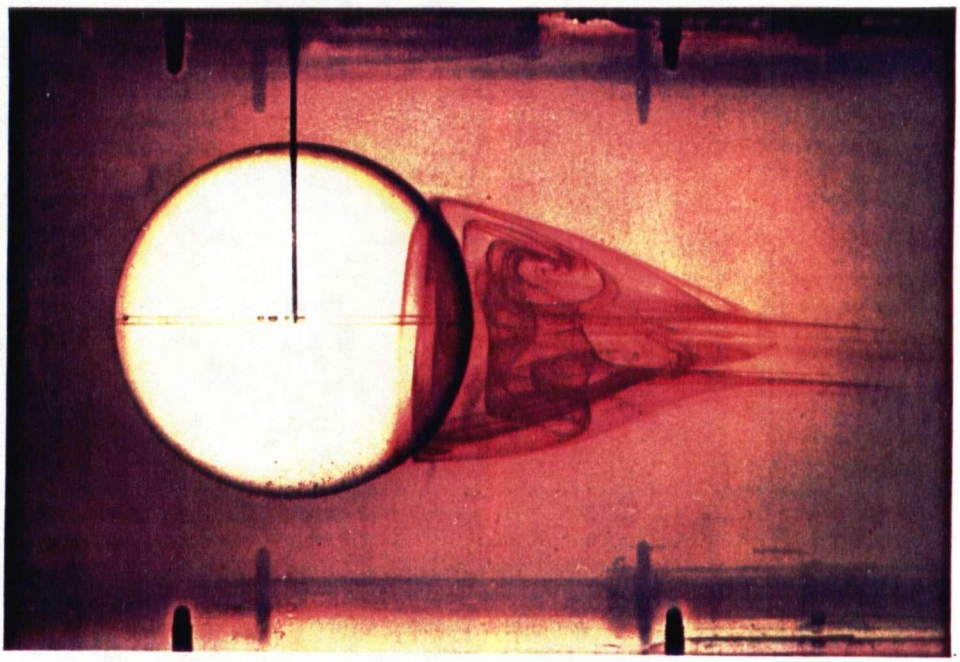

b

Figure 3-24 Typical photographs showing downstream movement of the separation position due to blockage: (a) R_n = 170, S/C = 2.7%; (b) R_n = 170, S/C ≅ 30.6%

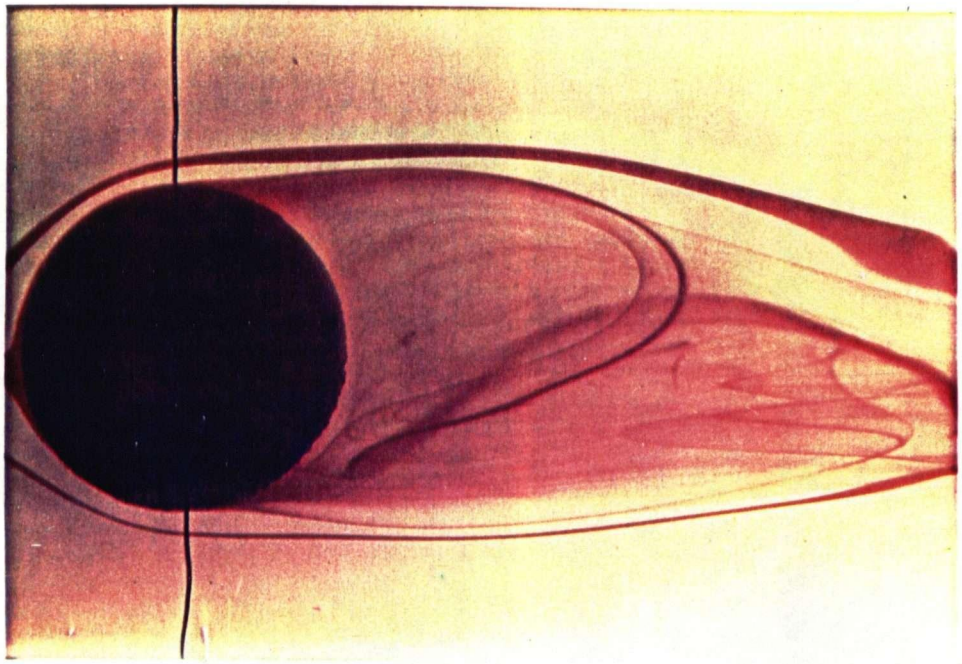

c

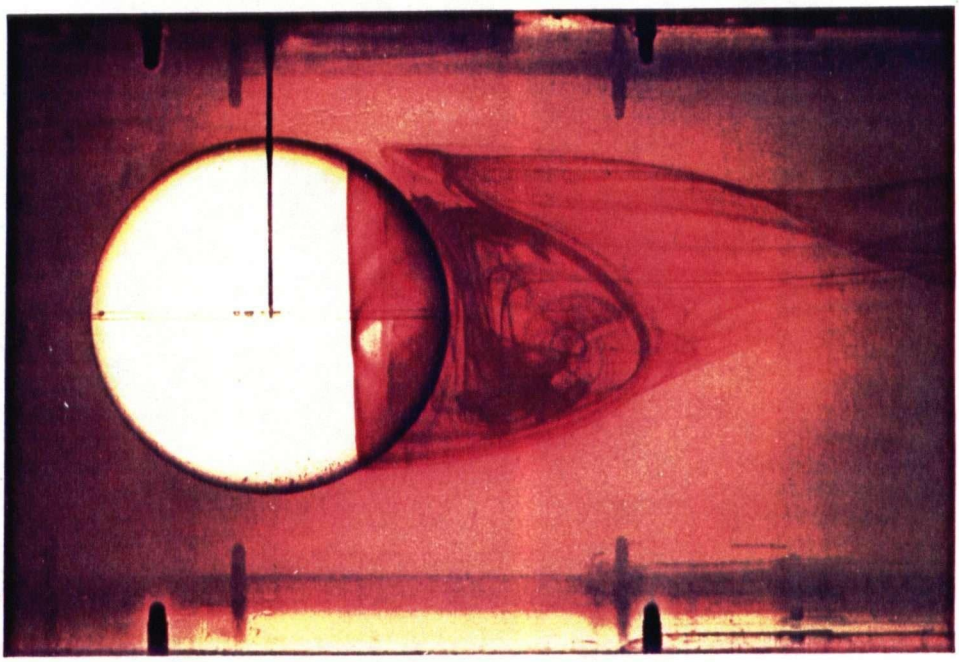

d

Figure 3-24 Typical photographs showing downstream movement of the separation position due to blockage: (c) R_n = 290, S/C = 2.7%; (d) R_n = 290, S/C ≅ 30.6%

at best, approximate. Considering this and the unstable character of the process, scatter in the experimental results is surprisingly small.

3.7 Closing Comments

It can be said with a measure of confidence that the experimental programme achieved considerably more than its initial objectives. To date the results have been analyzed only with reference to the immediate goal of assessing the blockage effects. However, there is a considerable scope for further analysis and interpretation of the data which would yield better appreciation of a variety of aspects associated with the fundamental fluid mechanics at low Reynolds number. The total experience was indeed exciting and satisfying because the project provided an exposure to the sophisticated experimental instrumentation and procedures and, more importantly, throughout there was a feeling of participation in a search for knowledge. The awareness of broader perspectives has left me humble for I realize that a scientific inquiry is unending. This is merely a beginning.

Before closing it would be appropriate to review some of the more significant results and express a few thoughts on possible avenues for future exploration which are likely to be profitable.

3.7.1 Concluding remarks

Important conclusions based on the experimental results may be summarized as follows:

(i) The use of average velocity in the test-section (based on the mean flow rate) as a reference velocity together with the pressure coefficient defined as

$$C_p = \frac{P_\theta - P_r}{P_0 - P_r}$$

promises to promote repeatability and comparison of data by other investigators regardless of the test facilities used. This approach tends to compensate for blockage effects, irregularity of the velocity profile and possible errors in pressure measurements caused by electrical drift of the pressure measuring system.

(ii) A vertical stem supporting the spherical model has negligible influence on the pressure distribution if the sphere to stem diameter ratio is greater than 10.

(iii) For pressure distribution on the surface of a sphere, the effect of Reynolds number is essentially confined to the region downstream of zero pressure point and even here it is limited to $R_n < 1000$, except for the very high blockage ratio of 30.6%. In general, the effect of Reynolds number is to increase the minimum as well as the wake pressure. Furthermore, locations of the minimum pressure and separation tend to shift little upstream.

(iv) For pressure distribution on the surface of a sphere, the confinement effects are essentially negligible up to around 11% blockage. But beyond that it has a definite tendency to reduce the minimum and base pressures. The minimum pressure point shows a distinct rearward shift with an increase in the blockage.

(v) Drag coefficient obtained by integrating pressure distribution data agrees rather well with Aminzadeh's results[47] and thus tends to substantiate reliability of the measuring instrumentation. Furthermore, the total drag compares favourably with the results, at small blockage by other investigators[3-5] thus reinforcing confidence in the strain gage balance. In general, the drag coefficient increases with blockage because of the local rise in the free stream velocity. Results also show the classical dependence of skin friction on the Reynolds number, $C_{d,f} \propto R_n^{-1/2}$.

(vi) Maskell's correction procedure for drag data is inadequate to compensate for higher confinement effects.

(vii) Flow visualization provided better appreciation as to the physical character of the flow in terms of formation, elongation and instability of the vortex ring. It showed the separation location to move downstream with an increase in blockage.

3.7.2 Recommendation for future study

As pointed out before, the present efforts at obtaining some appreciation as to the physics of the wall confinement effects at low Reynolds number represent only a modest beginning. There are numerous avenues along which the research program may progress in future. Some of the more important aspects, recommended for future studies, are summarized below:

(i) In the present set of experiments, blockage effects on the surface pressure distribution could not be studied for the Reynolds number < 280, limitation being imposed by the pressure measuring instrumentation. The surface pressure at lower Reynolds number was found to be so small $[O(10^{-5})psi]$ that it presented a problem of measurement with an acceptable degree of accuracy and repeatability. Therefore, it is suggested that pressure measurements at lower Reynolds number (and higher blockage) should be undertaken to provide a comprehensive picture of wall confinement effects. This can be accomplished using:

(a) more sensitive and stable pressure transducer (e.g., Digiquartz pressure transducers);

(b) a modified drive and the pump system so that higher concentration of glycerol-water solution can be handled.

(ii) No effort has been made here to evaluate pressure distribution, turbulence character and shear stress in the wake. In fact shear stress on the surface of the sphere, even in absence of blockage, in this range of Reynolds number remains unrecorded. The information is quite important in comparing relative performance of different prosthetic heart valves, as the parameter directly affects deformation, destruction and coagulation of the red blood cells.

(iii) The present study, due to limitation of time, was unable to focus attention on the frequency of the helical vortex shedding. It would be useful to explore this periodic phenomenon in depth, particularly, when there seems to be some question about its variation with the Reynolds number. Of course, the effect of blockage on the Strouhal number has received no attention.

(iv) Tests should be carried out with spherical model under diverse conditions of velocity profile, blockage, turbulence and pressure gradient to firmly establish universal character of the pressure distribution using proposed definition of the pressure coefficient.

(v) Blockage corrections for bluff bodies such as circular cylinder, flat plate, sphere, etc. in shear flow should provide useful information.

(vi) An important area of interest, which is particularly significant in biological fluid mechanics, would be the study of pulsatile flow past bluff bodies under wall confinement simulating a typical cardiac cycle. This may also involve modeling of turbulence character of the biological fluid flow and elasticity of the aorta. The field is relatively new and remains virtually unexplored to date.

BIBLIOGRAPHY

1. Torobin, L.B., and Gauvin, W.H., "Fundamental Aspects of Solids-Gas Flow, Part I: Introductory Concepts and Idealized Sphere Motion in Viscous Regime," The Canadian Journal of Chemical Engineering, Vol. 37, No. 4, August 1959, pp. 129-141; also "Part II: The Sphere Wake in Steady Laminar Fluids," Vol. 37, No. 5, October 1959, pp. 167-176; "Part III: Accelerated Motion of a Particle in a Fluid," Vol. 37, No. 6, December 1959, pp. 224-236; "Part IV: The Effects of Particle Rotation, Roughness and Shape," Vol. 38, No. 5, October 1960, pp. 142-153; "Part V: The Effects of Fluid Turbulence on the Particle Drag Coefficient," Vol. 38, No. 6, December 1960, pp. 189-200.

2. Heinrich, H.G., Niccum, R.J., and Haak, E.L., "The Drag Coefficient of a Sphere Corresponding to a 'One Meter Robin Sphere' Descending from 260,000 ft Altitude (Reynolds Nos. 789 to 23,448; Mach Nos. 0.056 to 0.90)," Research and Development of Robin Meteorological Rocket Balloon, Vol. II, Contract AF 19(604)-8034 AD480309, University of Minnesota, Minneapolis, Minn., May 1963.

3. Sivier, K.R., "Subsonic Sphere Drag Measurements at Intermediate Reynolds Numbers," Ph.D. Thesis, 1967, The University of Michigan, Ann Arbor, Mich.

4. Zarin, N.A., "Measurement of Non-Continuum and Turbulence Effects on Subsonic Sphere Drag," Ph.D. Thesis, 1969, The University of Michigan, Ann Arbor, Mich.

5. Ross, F.W., and Willmarth, W.W., "Experimental Results on Sphere and Disk Drag," AIAA Journal, Vol. 9, No. 2, February 1971, pp. 285-291.

6. Bailey, A.B., and Hiatt, J., "Sphere Drag Coefficients for a Broad Range of Mach and Reynolds Numbers," AIAA Journal, Vol. 10, No. 11, November 1972, pp. 1436-1440.

7. Goin, K.L., and Lawrence, W.R., "Subsonic Drag of Spheres at Reynolds Numbers from 200 to 10,000," AIAA Journal, Vol. 6, No. 5, May 1968, pp. 961-962.

8. Vlnajinac, M., and Covert, E.E., "Sting-free Measurements of Sphere Drag in Laminar Flow," J. Fluid Mechanics, Vol. 54, Part 3, 1972, pp. 385-392.

9. Achenbach, E., "Experiments on the Flow Past Spheres at Very High Reynolds Numbers," J. Fluid Mechanics, Vol. 54, Part 3, 1972, pp. 565-575.

10. Achenbach, E., "The Effects of Surface Roughness and Tunnel Blockage on the Flow Past Spheres," J. Fluid Mechanics, Vol. 65, Part 1, 1974, pp. 113-125.

11. Maxworthy, T., "Experiments on the Flow Around a Sphere at High Reynolds Numbers," Transactions of the ASME J. of Applied Mechanics, Vol. 36, No. 3, September 1969, pp. 598-607.

12. Möller, W., "Experimentelle Untersuchung zur Hydromechanik der Kugel," Phys. Z., Vol. 39, 1938, pp. 57-80.

13. Cometta, C., "An Investigation of the Unsteady Flow Pattern in the Wake of Cylinders and Spheres Using a Hot Wire Probe," Div. Engng, Brown University Tech. Report, WT-21, 1957.

14. Mujumdar, A.S., and Douglas, W.J.M., "Eddy Shedding from a Sphere in Turbulent Free Stream," Int. J. Heat and Mass Transfer, Vol. 13, 1970, pp. 1627-1629.

15. Calvert, J.R., "Some Experiments on the Flow Past a Sphere," Aero. J. Roy. Aero. Soc., Vol. 76, No. 4, 1972, pp. 248-250.

16. Achenbach,E., "Frequency and Configuration of Vortices Discharged from Sphere at High Reynolds Numbers," Proceedings of the International Symposium on Vibration Problems in Industry, Keswick, U.K., April 1973, Paper No. 111.

17. Achenbach, E., "Vortex Shedding from Spheres," J. Fluid Mechanics, Vol. 62, Part 2, 1974, pp. 209-221.

18. Taneda, S., "Experimental Investigation of the Wake Behind a Sphere at Low Reynolds Numbers," Journal of the Physical Society of Japan, Vol. 11, No. 10, October 1956, pp. 1104-1108.

19. Magarvey, R.H., and Bishop, R.L., "Transition Ranges for Three-Dimensional Wakes," Canadian J. Physics, Vol. 39, No. 10, October 1961, pp. 1418-1422.

20. Lee,K., and Barrow, H., "Some Observations on Transport Processes in the Wake of Sphere in Low Speed Flow," International J. Heat and Mass Transfer, Vol. 8, March 1965, pp. 403-409.

21. Goldburg, A., and Florsheim, B.H., "Transition and Strouhal Number for the Incompressible Wake of Various Bodies," Physics of Fluids, Vol. 9, No. 1, January 1966, pp. 45-50.

22. Modi, V.J., and Aminzadeh, M., "Separated Flow Past Spheres at Low Reynolds Number," AIAA 15th Aerospace Sciences Meeting, Los Angeles, Calif., January 1977, Paper No. 77-134.

23. Stokes, G.G., "On the Theories of the Internal Friction of Fluids in Motion, and of Equilibrium and Motion of Elastic Solids," Trans. Camb. Phil. Soc., Vol. 9, Pt. II, 1851, pp. 8-106.

24. Whitehead, A.N., "Second Approximations to Viscous Fluid Motion," Quart. J. Math., Vol. 23, 1889, pp. 143-152.

25. Proudman, I., and Pearson, J.R.A., "Expansion at Small Reynolds Number for the Flow Past a Sphere and Circular Cylinder," J. Fluid Mechanics, Vol. 2, Pt. 3, May 1957, pp. 237-262.

26. Oseen, C.W., "Über Die Stokes'sche Formal und Über eine Verwandte Aufgube in der Hydrodynamik," Ark. för Mat. Astr. O Frsik., Vol. 6, No. 29, September 1910.

27. Goldstein, S., "The Steady Flow of Viscous Fluid Past a Fixed Spherical Obstacle at Small Reynolds Numbers," Proc. Roy. Soc., Series A, Vol. 123, No. 791, March 1929, pp. 225-235.

28. Toniotika, S., and Aoi, T., "The Steady Flow of Viscous Fluid Past a Sphere and Circular Cylinder at Small Reynolds Numbers," Quart. J. Mech. Appl. Math., Vol. 3, Pt. 2, 1950, pp. 140-161.

29. Pearcey, T., and McHugh, B., "Calculation of Viscous Flow Around Spheres at Low Reynolds Numbers," Philosophical Magazine, Ser. 7, Vol. 46, No. 378, July 1955, pp. 783-794.

30. Kawaguti, M., "An Approximate Solution for Viscous Flow at Low Speeds," Tokyo Institute of Science and Technology Report, Vol. 2, May-June 1948, pp. 66-71.

31. Kawaguti, M., "Numerical Solution for the Viscous Flow Past a Sphere," Tokyo Institute of Science and Technology Report, Vol. 4, May-June 1950, pp. 154-158.

32. Fox, L., "A Short Account of Relaxation Methods," Quart. J. Mech. Appl. Math., Vol. 1, 1948, pp. 253-280.

33. Fox, L., and Southwell, R.V., "Relaxation Methods Applied to Engineering Problems," Phil. Trans., Series A, Vol. 239, No. 810, October 1945, pp. 419-460.

34. Allen, D.N., de G., and Dennis, S.C.R., "The Application of Relaxation Methods to the Solution of Differential Equations in Three Dimensions," Quart. J. Mech., Vol. 4, Part 2, 1951, pp. 199-208.

35. Jenson, V.G., "Viscous Flow Round a Sphere at Low Reynolds Numbers (<40)," Proc. Roy. Soc., Series A, Vol. 249, No. 1257, January 1959, pp. 346-366.

36. Hamielec, A.E., Hoffman, T.W., and Ross, L.L., "Numerical Solution of the Navier-Stokes Equation for Flow Past Spheres, Part I - Viscous Flow Around Spheres with and without Radial Mass Efflux," J. of The American Institute of Chemical Engineers, Vol. 13, No. 2, March 1967, pp. 212-219.

37. LeClair, B.P., Hamielec, A.E., and Pruppacher, H.R., "A Numerical Study of the Drag on a Sphere at Low and Intermediate Reynolds Numbers," J. Atmospheric Sciences, Vol. 27, No. 2, March 1970, pp. 308-315.

38. Pruppacher, H.R., LeClair, B.P., and Hamielec, A.E., "Some Relations Between Drag and Flow Pattern of Viscous Flow Past a Sphere and a Cylinder at Low and Intermediate Reynolds Numbers," J. Fluid Mechanics, Vol. 44, Pt. 4, 1970, pp. 781-790.

39. Dennis, S.C.R., and Walker, M.S., "The Steady Motion of a Viscous Fluid Past a Sphere," Aero. Res. Council Report, No. 26105, August 1964.

40. Rimon, Y., and Cheng, S.I., "Numerical Solution of a Uniform Flow Over a Sphere at Intermediate Reynolds Numbers," Physics of Fluids, Vol. 12, No. 5, May 1969, pp. 949-959.

41. Dennis, S.C.R., and Walker, J.D.A., "Calculation of the Steady Flow Past a Sphere at Low and Moderate Reynolds Numbers," J. Fluid Mechanics, Vol. 48, Part 4, 1971, pp. 771-789.

42. Van Dyke, M., Perturbation Methods in Fluid Mechanics, Academic Press, New York and London, 1964.

43. Modi, V.J., and Aminzadeh, M., "Hydrodynamic Performance of an Artificial Aortic Valve Implant," Proceedings of Fifth Canadian Congress of Applied Mechanics, Fredericton, May 1975.

44. Aminzadeh, M., and Modi, V.J., "A Theoretical Approach to the Wedge Shaped Hot Film Probe Performance," Aero. J. Roy. Aero. Soc., Vol.80, No. 791, November 1976, pp. 489-491.

45. Modi, V.J., and Aminzadeh, M., "Fluid Mechanics of an Aortic Heart Valve Implant," Proceedings of the 1977 Symposium on Biomechanics, ASME, New Haven, Conn., June 1977, Editor: Richard Skalak, pp. 137-140.

46. Modi, V.J., and Aminzadeh, M., "Fluid Mechanics of Oscillating Spherical Poppet Used in Starr-Edwards Heart Valve Prosthesis," Trans. ASME, Journal of Biomechanics, in press.

47. Aminzadeh, M., "Hydrodynamic Performance of an Artificial Aortic Valve Implant," Ph.D. Thesis, 1975, The University of British Columbia, Vancouver, British Columbia.

48. Rasmussen, C.G., "The Air Bubble Problem in Water Flow Hot-Film Anemometry," Disa Information, No. 5, June 1967, pp. 21-26.

49. Morrow, T.G., "Effects of Dirt Accumulation on Hot-Wire and Hot-Film Sensors," Fluid Dynamic Measurements in the Industrial and Medical Environments, Proceeding of the Disa Conference held at the University of Leicester, Vol. 1, April 1972, pp. 122-124.

50. Pinchon, J., "Comparison of Some Methods of Calibrating Hot-Film Probes in Water," Disa Information, No. 10, October 1970, pp. 15-21.

51. Kalashnikov, V.N., and Kudin, A.M., "Calibration of Hot-Film Probes in Water and in Polymer Solutions," Disa Information, No. 14, March 1973, pp. 15-18.

52. Batchelor, G.K., An Introduction to Fluid Dynamics, Cambridge University Press, 1967, pp. 201-204.

53. Batchelor, G.K., and Townsend, A.A., "Decay of Turbulence in the Final Period," Proc. Roy. Soc., Series A, Vol. 194, No. 1039, November 1948, pp. 527-543.

54. Taback, I., "The Response of Pressure Measuring Systems to Oscillating Pressures," NACA TN 1819, 1949.

55. Iberall, A.S., "Attenuation of Oscillatory Pressure in Instrument Lines," Journal of Research, National Bureau of Standards, Vol. 45, July 1950, pp. 85-108.

56. D'Souza, A.F., and Oldenburger, R., "Dynamic Response of Fluid Lines," Trans. ASME, Series D, Journal of Basic Engineering, Vol. 86, No. 3, September 1964, pp. 589-598.

57. Grove, A.S., Shair, F.H., Petersen, F.E., and Acrivos, A., "An Experimental Investigation of the Steady Separated Flow Past a Circular Cylinder," J. Fluid Mechanics, Vol. 19, Pt. 1, May 1964, pp. 60-80.

58. Acrivos, A., Leal, L.G., Snowden, D.D., and Pan, F., "Further Experiments on Steady Separated Flows Past Bluff Objects," J. Fluid Mechanics, Vol. 34, Pt. 1, 1968, pp. 25-48.

59. Modi, V.J., and El-Sherbiny, S.E., "A Free-Streamline Model for Bluff Bodies in Confined Flow," Trans. ASME, Journal of Fluid Engineering, in press.

60. White, F.M., Viscous Fluid Flow, McGraw-Hill, New York, 1974, pp. 208-210.

61. Rosenhead, L., Laminar Boundary Layers, Oxford University Press, 1963, pp. 102-109.

APPENDIX I

CONVENTIONAL PRESSURE COEFFICIENT $\overline{C}_p$ IN TERMS OF MEASURED INFORMATION

In a low Reynolds number experiment using a liquid tunnel, difficulties in establishing characteristic reference velocity and pressure, P_∞ and U_∞, were discussed before. However, for comparison and to establish relative effectiveness of the new definition of pressure coefficient, one can calculate the conventional pressure coefficient $\overline{C}_p = (P_\theta - P_\infty)(1/2)\rho U_\infty^2$ quite readily using differential pressure data measured during the experiment.

The x component of Navier-Stokes equation along the stagnation streamline $y = 0$ can be written as

$$u \frac{\partial u}{\partial x} = - \frac{1}{\rho} \frac{\partial P}{\partial x} + \nu \left[\frac{\partial^2 u}{\partial x^2} + \frac{\partial^2 u}{\partial y^2}\right] .$$

Integrating from front stagnation point to minus infinity upstream of the sphere yields,

$$\int_{-\infty}^{0} u \frac{\partial u}{\partial x} dx = - \frac{1}{\rho} \int_{-\infty}^{0} \frac{\partial P}{\partial x} dx + \nu \int_{-\infty}^{0} \left[\frac{\partial^2 u}{\partial x^2} + \frac{\partial^2 u}{\partial y^2}\right] dx$$

$$- \frac{u_\infty^2}{2} = - \frac{P_0}{\rho} + \frac{P_\infty}{\rho} + \nu \int_{-\infty}^{0} \left[\frac{\partial^2 u}{\partial x^2} + \frac{\partial^2 u}{\partial y^2}\right] dx$$

$$\frac{P_0}{\rho} = \frac{P_\infty}{\rho} + \frac{u_\infty^2}{2} + \nu \int_{-\infty}^{0} \left[\frac{\partial^2 u}{\partial x^2} + \frac{\partial^2 u}{\partial y^2}\right] dx$$

$$\frac{P_0 - P_\infty}{1/2\ \rho\ U_\infty^2} = 1 + \frac{\nu}{1/2\ U_\infty^2} \left\{ \int_{-\delta}^{0} \left[\frac{\partial^2 u}{\partial x^2} + \frac{\partial^2 u}{\partial y^2}\right] dx \right.$$

$$\left. + \int_{-\infty}^{-\delta} \left[\frac{\partial^2 u}{\partial x^2} + \frac{\partial^2 u}{\partial y^2}\right] dx \right.$$

where δ is the boundary-layer thickness. The second integral vanishes because of irrotationality of the outer flow while in the first integral usual boundary layer approximation

$$\frac{\partial^2 u}{\partial x^2} >> \frac{\partial^2 u}{\partial y^2}$$

can be introduced. Since

$$\frac{\partial u}{\partial x} = -\frac{\partial v}{\partial y} = 0 \qquad \text{at} \qquad x = 0 \ ,$$

$$\frac{P_0 - P_\infty}{1/2\ \rho\ U_\infty^2} = 1 - \frac{\nu}{1/2\ U_\infty^2} \left.\frac{\partial u}{\partial x}\right|_{\substack{x = \delta \\ y = 0}} = 1 + \frac{A}{R} + \cdots$$

where A is a constant and R is the Reynolds number.

Here the numerical value of A follows directly from the outer flow solution.

Using the potential flow analysis, Homann as well as Grove et al.[57] have shown, independently, the value of A to be 8. Thus,

$$\frac{P_0 - P_\infty}{1/2\ \rho\ U_\infty^2} = 1 + \frac{8}{R} + \cdots\cdots ,$$

i.e.,

$$P_\infty - P_{60^\circ} = (P_0 - P_{60^\circ}) - (1 + \frac{8}{R} + \cdots\cdots) 1/2\ \rho\ U_\infty^2 \quad .$$

Now

$$P_\theta - (P_\infty - P_{60^\circ}) = P_\theta - \{(P_0 - P_{60^\circ}) - (1 + \frac{8}{R} + \cdots\cdots) 1/2\ \rho\ U_\infty^2\} ,$$

$$\therefore \quad \frac{P_\theta - P_\infty}{1/2\ \rho\ U_\infty^2} = \frac{P_\theta - P_{60^\circ}}{1/2\ \rho\ U_\infty^2} - \frac{P_0 - P_{60^\circ}}{1/2\ \rho\ U_\infty^2} + (1 + \frac{8}{R} + \cdots\cdots) \quad .$$

Recognizing that for a Reynolds number as low as 300 contribution of 8/R term is less than 3%, the above expression reduces to

$$\frac{P_\theta - P_\infty}{1/2\ \rho\ U_\infty^2} = \frac{(P_\theta - P_{60^\circ}) - (P_0 - P_{60^\circ})}{1/2\ \rho\ U_\infty^2} + 1 \quad .$$

APPENDIX II

A PROCEDURE FOR DRIFT CORRECTION USING DIRECT MEASUREMENT OF THE DIFFERENTIAL PRESSURE

Let the objective be to measure a differential pressure, $\Delta P_\theta = P_\theta - P_r$ between the location of interest and the pressure at a reference point. Let the arbitrary zero drift of the electronic system be as indicated in Figure II-1. The diagram also shows the corresponding drift of the differential pressure ΔP_θ. From the figure it follows that:

$$\Delta P_{\theta_1} = \Delta P_\theta + \delta_1 \quad ;$$

$$\Delta P_{\theta_2} = \Delta P_\theta + \delta_1 + \delta_2 \quad ;$$

$$\Delta P_{\theta_3} = \Delta P_\theta + \delta_1 + \delta_2 + \delta_3 \, .$$

Therefore,

$$\Delta P_{\theta_1} + \Delta P_{\theta_3} - \Delta P_{\theta_2} = (\Delta P_\theta + \delta_1) + (\Delta P_\theta + \delta_1 + \delta_2 + \delta_3) - (\Delta P_\theta + \delta_1 + \delta_2)$$

$$= \Delta P_\theta + \delta_1 + \delta_3 \quad ;$$

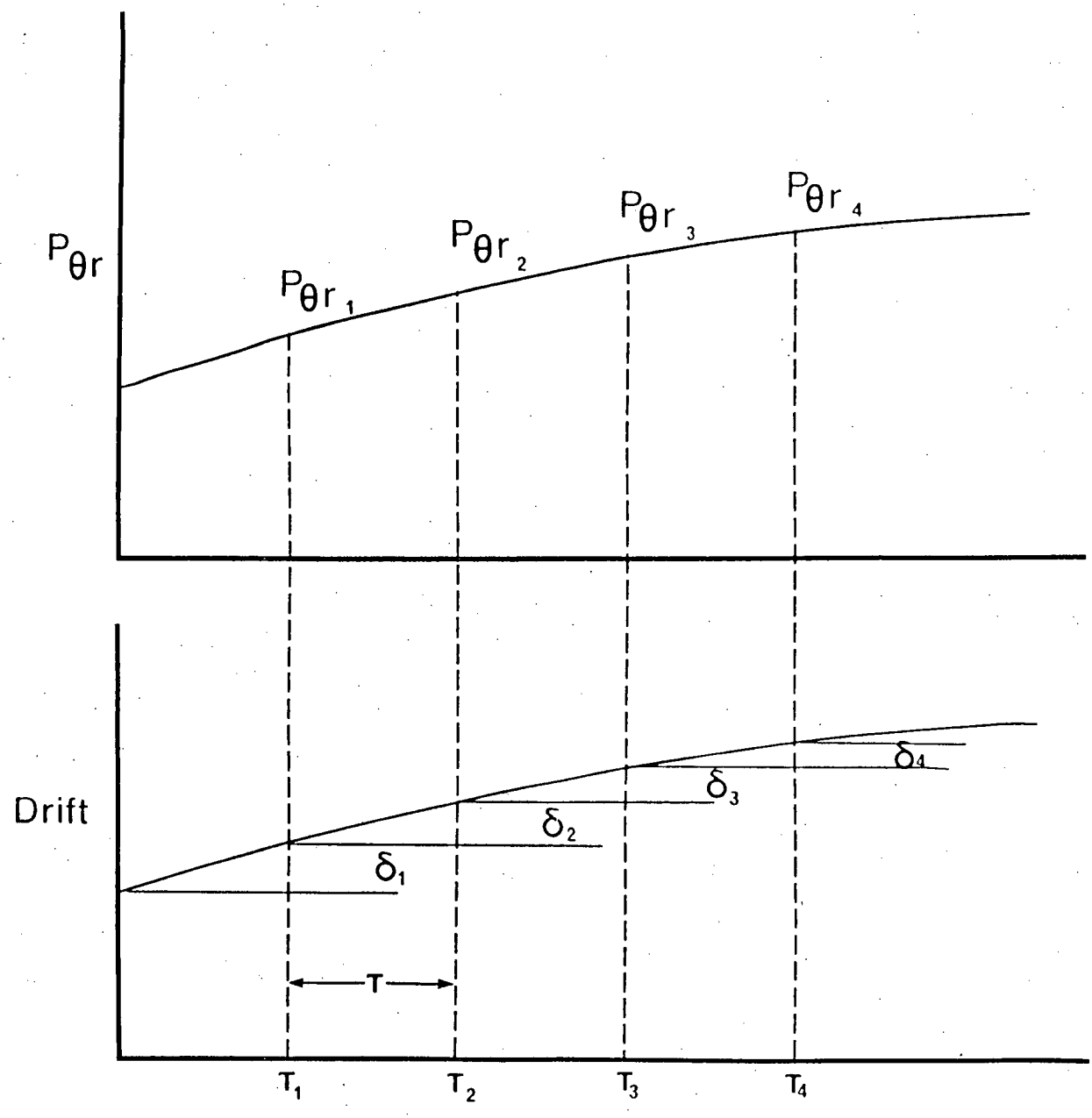

Figure II-1 A drift correction procedure using direct measurement of the differential pressure

$$\text{i.e.,}\quad \Delta P_\theta = \Delta P_{\theta_1} + \Delta P_{\theta_3} - \Delta P_{\theta_2} - \delta_1 - \delta_3 \,. \qquad \text{(II.1)}$$

Now

$$\delta_2 = \Delta P_{\theta_2} - \Delta P_{\theta_1} \,,$$

$$\delta_3 = \Delta P_{\theta_3} - \Delta P_{\theta_2} \,;$$

$$\therefore \quad \delta_2 + \delta_3 = \Delta P_{\theta_2} - \Delta P_{\theta_1} + \Delta P_{\theta_3} - \Delta P_{\theta_2}$$

$$= \Delta P_{\theta_3} - \Delta P_{\theta_1} \,.$$

Assuming the drift to be linear over a small time interval,

$$\delta_1 = \frac{\delta_2 + \delta_3}{2} = \frac{\Delta P_{\theta_3} - \Delta P_{\theta_1}}{2} \,.$$

Hence the desired differential pressure ΔP_θ

$$\Delta P_{\theta_1} + \Delta P_{\theta_3} - \Delta P_{\theta_2} - \left(\frac{\Delta P_{\theta_3} - \Delta P_{\theta_1}}{2}\right) - \left(\Delta P_{\theta_3} - \Delta P_{\theta_2}\right)$$

$$= \frac{3}{2}\,\Delta P_{\theta_1} - \frac{1}{2}\,\Delta P_{\theta_3} \,.$$

Thus determination of the differential pressure ΔP_{θ} involves the measurement of ΔP_{θ_1} and ΔP_{θ_3}. In practice it was found to be extremely difficult to accomplish these measurements with an acceptable accuracy.